"The Amyloidogenic Propensity of Human Proislet Amyloid Polypeptide in the Presence of Lipids"

DISSERTATION

**Zur Erlangung des akademischen Grades
Doktor der Naturwissenschaften
(Dr. rer. nat.)**

Vorgelegt von

Suman Jha

M.Sc.

aus Madhubani, India

**eingereicht bei der
Fakultät Chemie
der Technische Universität Dortmund**

Dortmund 2009

Erstgutacheter: **Prof. Dr. Roland Winter**

Zweitgutachter: **Prof. Dr. Martin Engelhard**

Dritter Prüfer: **PD. Dr. Claus Czeslik**

"Dedicated to my dear parents and friends"

List of Abbreviations

Aβ	Amyloid beta peptide
AFM	Atomic force microscopy
ANF	Atrial natriuretic factor (atrial amyloidosis)
APP	Amyloid precursor protein
ATR-FTIR	Attenuated total reflection Fourier transform infrared
CD	Circular dichroism
CDNN	Circular dichroism neural network
Chol	Cholesterol
CMC	Critical micelle concentration
CPE	Carboxypeptidase E
DOPC	1,2-dioleyl-sn-glycero-3- phosphatidylcholine
DOPG	1,2-dioleyl-sn-glycero-3-[phospho-*rac*-(1-glycerol)]
DPPC	1,2-dipalmitoyl-sn-gylcero-3-phosphatidylcholine
Far-UV / near-UV	Far ultraviolet / near ultraviolet
FTIR	Fourier transform infrared
hIAPP	Human islet amyloid polypeptide
Htt	Huntingtin
IAPP	Islet amyloid polypeptide
IRRAS	Infrared reflection absorption spectroscopy
LUVs	Large unilamellar vesicles
mM / µM / nM	Millimolar (10^{-3} M) / micromolar (10^{-6} M) / nanomolar (10^{-9} M)
nm / µm	Nanometer (10^{-9} m) / micrometer (10^{-6})
PAM	Peptidyl amidating mono-oxygenase
PC	Prohormone convertase
ProIAPP	Proislet amyloid polypeptide
PrP	Prion protein
rIAPP	Rat islet amyloid polypeptide
rpm	Revolutions per minute
s / min / h / d	Second / minute / hour / day

SDS	Sodium dodecyl sulfate
T2DM	Type 2 diabetes mellitus
ThT	Thioflavin T
TIA1	T-cell intracellular antigen-1
TTR	Transthyretin
UV-Vis	Ultraviolet-visible
w/w	Weight by weight ratio

Acknowledgements

Contents

Chapter 1.   Introduction

1.1.   Type 2 diabetes mellitus

The cellular proteome changes constantly according to the requirements arising due to the potentially changing chemical environment. For example, changes in the blood glucose or the free fatty acid levels affect the proteomics of pancreatic β-cells. This cellular proteome regulation is controlled by cellular protein homeostasis, which is also known as "proteostasis" (*1*). It is regulated by the proteostasis network, which includes protein translation, folding, trafficking, etc. When there are major changes in the composition of cellular moieties compared to the normal composition, this proteostasis network goes awry and leads to the onset of diseases, like cystic fibrosis, type-2 diabetes mellitus (T2DM), etc. (*2*). T2DM is one of the diseases in which the proteostasis network of pancreatic β-cells goes awry, leading to alteration in the regulation of islet amyloid polypeptide (IAPP) and the insulin proteostasis network. In turn, this leads to amyloid deposits of these polypeptides in the pancreas and causes T2DM, which is known to affect over 100 million people worldwide (*3*). This disease is marked by high blood glucose levels due to insulin resistance, or relative insulin deficiency, which arises due to the death of the pancreatic β-cells. Pancreatic amyloid deposits have been found in over 90% of T2DM cases, mainly as extracellular deposits in the proximity of β-cells of pancreas (*4, 5*). However, the mechanism of cell death by amyloid fibrils or by protofibrils / oligomers is not well known.

Among the peptides secreted by pancreatic β-cells, the relatively higher amyloidogenic propensity of IAPP, as suggested by its sequence analysis as well as its ability to fibrillate *in vitro*, makes this peptide a major culprit of T2DM. However, IAPP gene polymorphisms are not universally associated with type 2 diabetes mellitus. It has been found that transgenic mice expressing the human IAPP gene have an increased IAPP concentration, but develop islet amyloid deposits only on a high fat diet (*6*). All these *in vivo* experiments pointed out a number of possibilities that could be the possible trigger factors for the onset and progression of T2DM in human (Figure 1). Additionally, they also pointed out that not only IAPP, but also its precursor processing intermediates could be the primary culprit in T2DM under certain conditions. Figure 1 represents the possible factors that may involve the onset and progression of T2DM in human.
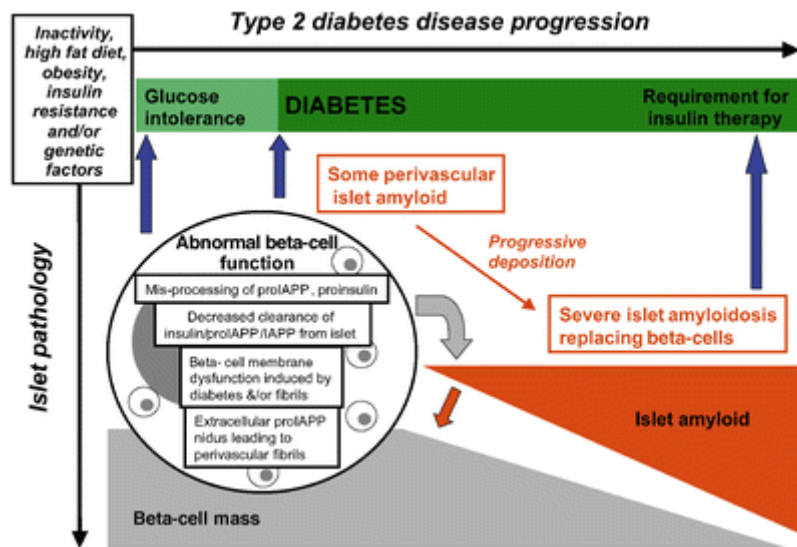
Figure 1: Schematic representation of the potential relationship of islet dysfunction, islet amyloid, and β-cell destruction in the pathophysiology of T2DM (adopted from Clark, et al. 2004 (*7*)).

1.2.   Proislet amyloid polypeptide (proIAPP)

Proislet amyloid polypeptide (proIAPP) is a 67 amino acid long polypeptide, and represents the precursor of the physiologically active human IAPP or say amylin (*8*). ProIAPP is translated on the rough endoplasmic reticulum as a secretory protein, inside the pancreatic β-cells. Subsequently, it is transferred into the lumen of the endoplasmic reticulum, where the disulfide bond between Cys13 and Cys18 of proIAPP is formed (*9-11*). The processing of proIAPP to IAPP occurs within the secretory granules of pancreatic β-cells. It starts with the removal of 11 residues from the N-terminus and 16 residues from the C-terminus of proIAPP, by the actions of the enzymes known as prohormone convertase, PC2 and PC1/3 or furin. Thereafter, the basic prohormone convertase recognition motif (i.e. Lys52-Arg53) is removed by the action of carboxypeptidase E, followed by the peptidylglycine α-amidating mono-oxygenase complex (PAM) that removes the Gly38 residue and amidates the exposed carboxy-terminus of Tyr37 (*9-12*). Thus, the normal processing of a 67-residue proIAPP to yield a 37-residue IAPP requires, apart from disulfide bond formation between Cys13 and Cys18 of proIAPP, the removal of 11 residues and 16 residues from the N- and C- termini, respectively. In addition, the basic recognition motif and Gly37 are removed, followed by amidation of the carboxy end of Tyr37 (Figure 2) (*12*). ProIAPP is co-processed, co-stored, and co-secreted with insulin as IAPP (*8, 13*). Thus, the physiologically active form of proIAPP, i.e., IAPP is secreted into

the extracellular matrix in response to various stimuli to maintain the blood glucose level (*8, 14, 15*). IAPP is known to be involved in glucose metabolism, and to act as an insulin antagonist (*8*). However, the exact physiological role of IAPP is still not clear (*16*). ProIAPP does not show any amyloidogenic propensity in bulk solution, despite its primary sequence that shares partly the primary sequence of amyloidogenic IAPP and its precursor processing intermediates (*17*). This non-amyloidogenic property of proIAPP in bulk solution has been attributed to the presence of relatively more positively charged residues at the N-terminus of its sequence (*17, 18*). Moreover, the overproduction of proIAPP or IAPP does not trigger amyloid deposition inside the pancreas, until there are some mutations that favor the fibrillation of these peptides (*4*). Nevertheless, studies on the nude mice with transplanted human islet (*19*), and on the transgenic mice expressing human IAPP (*6*) have indicated that the early stages of islet amyloid formation may take place intracellularly. These intracellular aggregates are found to be immunoreactive for partially processed and unprocessed proIAPP (*20*), underlining the possibility that proIAPP and its precursor processing intermediates may be important in the early intracellular amyloid formation.

The full length proIAPP has made it to the list of potential primary culprits in the onset of T2DM, since it has been found that *in vitro* positively charged N-terminal extended proIAPP interacts with negatively charged heparin sulfate proteoglycans (HSPG) (*21*). Thus, this electrostatic interaction with negatively charged cellular moieties may modulate its amyloidogenic propensity, which in turn may act as a seed for the amyloid deposition *in vivo (21)*. Because of these reasons, the amyloidogenic propensity of proIAPP in the presence of charged surface or cellular moieties has been under intense scrutiny, recently. Various research groups are working to explore the possible factors, which may affect the amyloidogenic propensity of proIAPP and its precursor processing intermediates inside the cell, especially in the presence of negatively charged surfaces or moieties that are either absent or present in very low quantity at non-pathological conditions. Because of these reasons, lipid membranes (largest charged surface present inside the cell) have been studied extensively (*18, 22-24*).

PC 1/3

| | 1 | 10 | 20 | 30 | 37 |
ProIAPP (67) TPIESHQVEKRKCNTATCATQRLANFLVHSSNNFGAILSSTNVGSNTYGKRNAVEVLKREPLNYLPL
                        + ++   +   ++   ++

NH$_2$-terminal   IAPP 1-37   COOH-terminal

PC2   CPE

NH$_2$-terminally extended proIAPP

TPIESHQVEKRKCNTATCATQRLANFLVHSSNNFGAILSSTNVGSNTYG
                +++   +

PAM

Mature IAPP   KCNTATCATQRLANFLVHSSNNFGAILSSTNVGSNTY-NH$_2$
                              +   +
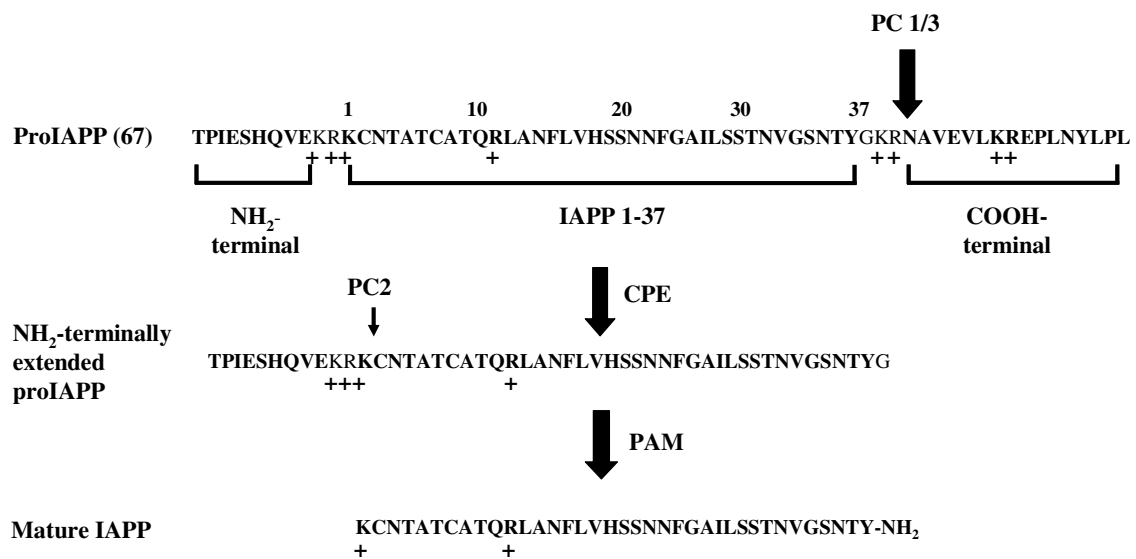
Figure 2: Proposed pathway for the normal processing of human proIAPP in pancreatic β-cells. Abbreviations: PC Prohormone Convertase, CPE Carboxypeptidase E, PAM Peptidyl Amidating Mono-oxygenase complex (adopted from Jha, et al. 2009 (*18*)).

1.3. Amyloid fibrils and their conformations

Amyloid is a term given to the abnormally insoluble fibrous structure formed by otherwise soluble monomeric protein molecules. The process of their formation is defined as "amyloidogenesis". This heterogeneous mechanism of amyloidogenesis is accompanied by the various intermediate species, termed as "oligomers", "protofibrils", and "fibrils". Since either the intermediate species or the fibrils have cytotoxic property (*25*), their formation leads to the onset of diseases, collectively called "amyloidoses". The amino acid composition and the sequence analysis of the amyloid deposits revealed that each amyloidosis is associated with a particular protein/peptide (*26*). However, the amyloidogenic propensity of each peptide depends on several factors like polypeptide charge, sequence, hydrophobicity, secondary structure, etc. To date, more than 20 amyloidoses causing proteins/peptides have been identified (see Table 1) (*27*). However, some non-disease related peptides and proteins have been shown to self-assemble into amyloid fibrils under denaturing conditions as well (*28, 29*); it is now considered that fibril formation is an inherent property of all proteins/peptides under certain environmental conditions (*30*).

Table 1: Some amyloidoses and their respective precursors and amyloidogenic proteins (adopted from Rambaran, et al. 2008 (*27*)).

Disease	Precursor protein	Amyloid protein
Alzheimer's disease	Amyloid precursor protein	Aβ peptides
Atrial amyloidosis	Atrial natriuretic factor (ANF)	Amyloid ANF
Spongiform encephalopathies	Prion protein (PrPc)	PrPsc
Primary systemic amyloidosis	Immunoglobulin light and heavy chains	AL and AH
Senile systemic amyloidosis	Wild-type transthyretin	ATTR
Haemodialysis-related amyloidosis	β2-microglobulin	Aβ2M
Hereditary nonneuropathic systemic amyloidosis	Lysozyme	ALys
Type 2 diabetes mellitus (T2DM)	**Pro-IAPP**	**IAPP or "amylin"**
Injection-localized amyloidosis	Insulin	AIns
Secondary systemic amyloidosis	(Apo) serum amyloid A	Serum amyloid A
Hereditary cerebral amyloid angiopathy	Cystatin C	ACys
Finnish hereditary systemic amyloidosis	Gelsolin	AGel
Familial amyloid polyneuropathy I	Transthyretin variants	ATTR
Familial amyloid polyneuropathy II	Apolipoprotein A1	AApoA1
Ageing pituitary, prolactinomas	Prolactin	APro
Familial amyloidosis	Fibrinogen αA-chain	AFib
British familial dementia	Amyloid Bri Precursor Protein	ABri

Over the last decades, the abnormally stable conformations of amyloid fibrils have drawn the attention of chemists from all over the world. Despite the differences in the amino acid sequences of these amyloidogenic peptides, all share a common β-sheet conformation of their polypeptide backbone (*31, 32*). On the basis of experimental studies, several molecular mechanisms have been proposed till date, in order to explain the formation and the stability of amyloid fibrils *in vitro*, including polar zipper (*33, 34*) and domain swapping models (*35, 36*). In the polar zipper mechanism, the complementary repeating amino acid sequence of hydrogen donors and acceptors along the side chains come together into a β-sheet conformation, as shown in Figure 3. In the domain swapping mechanism, a domain of a protein breaks its non-covalent bonds with the remainder of the molecule and its place is taken by the same domain of a second molecule, and this

propagates into a polymeric conformation with cross-β conformation, as shown in Figure 4. An assembly, following a domain swapping mechanism is both energetically and kinetically favorable in comparison with the equivalent association of monomers due to the increased effective concentration of monomers in the dimer.
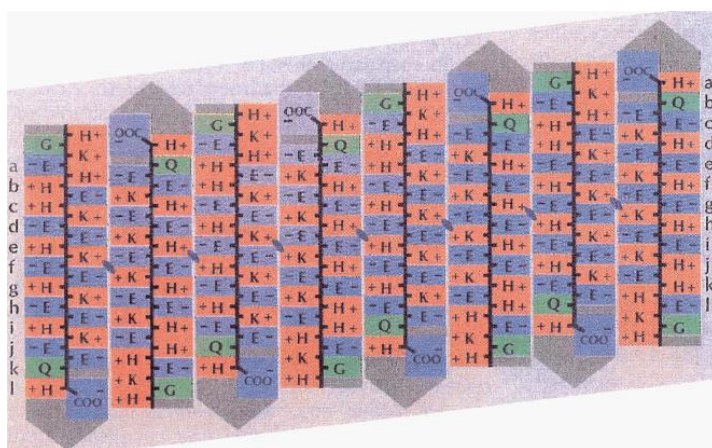
Figure 3: Polar zipper model found in carboxy-terminal peptides of *Ascaris* hemoglobin arranged in an antiparallel pleated sheet with compensating charges (adopted from Perutz, et al. 1994 (*34*)).

Figure 4: Schematic representation of a possible assembly of cystatin dimers into a continuous β-sheet structure, where dimers are connected via an interface between strands 1 and 5 (adopted from Staniforth, et al. 2001 (*35*)).

The amyloid fibrils formed from any amyloidogenic peptides via any of these mechanisms share the same core conformation that is a β-sheet placed perpendicular to the elongation axis and the direction of hydrogen bonds between the sheets run parallel to the elongation axis of fibrils. This arrangement has been studied elaborately by X-ray scattering, where the lowest-order reflection, i.e., 4.8 Å, suggests that the amyloid core contains 24 β-strands in 115.5 Å-long repeating units each along the fibril axis (Figure 5) (*31*). Most of the native β-sheets have a right handed twist, because right-handed twisted conformations represent the lowest energy conformation for a β-sheet. It is assumed that the amyloid protofilaments also incorporate the lower energy β-sheets conformation, i.e., right-handed β-sheet; this twist of the β-sheets has a common axis, which runs parallel to the axis

of the protofibrils and accounts for the repeating unit of approximately 115 Å (*37, 38*). This helical nature of protofilaments enables the hydrogen bonding between β-strands to be extended over the total length of the amyloid fibrils, thereby accounting for their rigidity and stability (*31, 39*). However, mature amyloid fibrils vary in morphology, depending upon the assembly or fibrillation conditions (*39*).

115 Å
24 β-strands
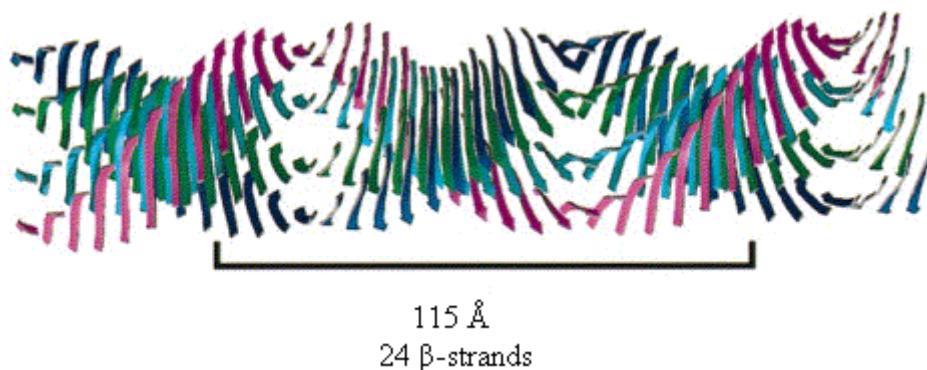
Figure 5: Model of the generic amyloid core structure. A number of β-sheets (four illustrated here) make up the protofilament structure. These sheets run parallel to the axis of the protofilament, with their component β-strands perpendicular to the fibril axis (adopted from Sunde, et al. 1997 (*31*)).

Thus, amyloid fibrils are cross-β in nature, and the β-sheet conformation forms the core of the fibril structure. The stability of these β-strands appears to be derived from a combination of forces like for native proteins, which includes not only hydrogen bonding but also the stacking of side chains between the strands that play a very important role in their stabilization (*40*).

1.4.   Mechanism of amyloid formation at membrane interfaces

It has been shown that some natively unfolded polypeptides, e.g. IAPP (*22*), α-synuclein (*41*), and medin (*42*), undergo amyloid fibril formation through helical intermediate conformations. Since these α-helical intermediate conformations play an important role in aggregation processes, all the reagents that induce α-helical conformations in these unfolded polypeptides, e.g. surfactants (SDS), TFE (2,2,2-trifluoroethanol), HFIP (1,1,1,3,3,3-hexafluoroisopropanol), become very important for studying fibrillation phenomena. Amongst all these reagents, studies with surfactants might have a direct significance in understanding the possible mechanism of membrane induced fibrillation for

unfolded polypeptides *in vivo*. However, most studies described in literature so far were carried out *in vitro* using isolated target molecules in dilute aqueous environments, thereby neglecting a key feature of cellular environments, the confined space and presence of lipid interfaces. Normally, nascent amyloidogenic proteins are released *in vivo* into an intracellular environment, which is congested by other large biomolecules. This congestion process is called "molecular crowding" (*43, 44*). Molecular crowding can stimulate self-association of amyloidogenic proteins (*45*). However, cell interiors do not only have an aqueous three dimensional congested environment, but also display dynamic biological membranes with two dimensional surfaces of varying charge and physical properties as a response to intracellular conditions (*46, 47*); these membrane surfaces have been shown to affect the protein folding and aggregation (*46*). Moreover, amyloid deposits analyzed from different amyloidoses show the presence of the lipids (*48, 49*). The exact mechanism of spatial and temporal incorporation of lipids into amyloid deposits still remains unclear. The amyloidogenic monomeric peptides, as well as intermediate species of amyloidogenesis, have been shown to manifest an affinity towards the lipid membrane. It is not clear whether this incorporation of lipids happens at the beginning of the amyloidogenesis, whereby the lipid acts as a catalyzing surface, or at later stages when these intermediate species interact with lipids and cause lipid membrane disruption. In order to understand the role of membranes in amyloidosis, and of amyloidosis on membrane disruption, a number of studies on amyloidogenic peptides have been undertaken in the presence of simple membrane-mimicking surfaces (*50*), monolayer membrane interfaces (*22*), and bilayer membrane interfaces (*18, 51*). From all these studies, a general mechanistic model has been proposed, suggesting that the interactions of many amyloidogenic peptides with the membranes is mainly initiated by electrostatic interactions between charged residues present at the peptide and oppositely charged membrane moieties. Thus, an increased peptide concentration on the membrane surface, because of the electrostatic interaction, facilitates the self-assembly of amyloidogenic structures through hydrophobic interaction between monomeric peptide conformations, as shown in Figures 6 (bilayer model) and 7 (monolayer model) (*52-54*).
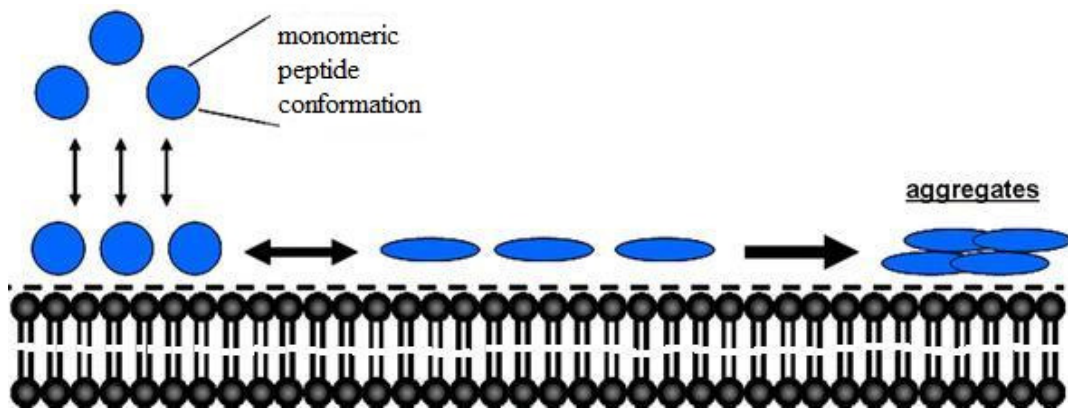
Figure 6: Schematic model of association and aggregation of amyloidogenic proteins on a bilayer membrane surface: peptide monomers bind electrostatically to a negatively charged membrane surface (left). Membrane-induced conformational changes (middle) in combination with an increased concentration of surface-bound protein initiate and accelerate conversion into β-sheet like amyloidogenic structures (right) (adopted from Bystrom, et al. 2008 (*55*)).
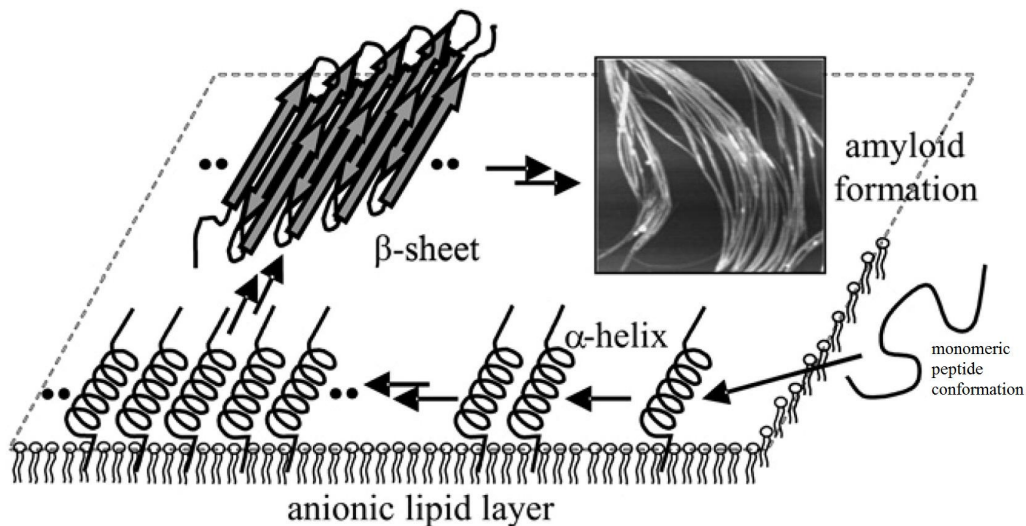
Figure 7: Schematic model of peptide-lipid monolayer interaction, lipid-induced peptide conformational transitions, and fibril formation – upon adsorption of the peptide, a subsequent conformational transition, which is then followed by the self-assembly of peptide monomers into amyloid fibrils (adopted from Lopes, et al. 2007 (*22*)).

Thus, the protein aggregation in the sub-three-dimensional environment of membrane interfaces may be differentiated into three main steps:

1) Adsorption of monomeric peptide onto the membrane interface, and the subsequent transition into a partially folded conformation.
2) Formation of the nucleus, or of oligomers.
3) Formation and growth of the fibrillar structure.

The last two steps of protein aggregation in sub-three-dimensional environments are association-driven and the first involves conformational changes. Each of these steps is influenced by the molecular crowding or by the membrane-solution interface, arising from adsorption at the membrane. Thus, the presence of membrane interfaces, or sub-three-dimensional environments, modulate the fibrillation kinetics of amyloidogenic peptides.

1.5.   Tuned amyloidogenesis

Amyloidogenesis is a nucleation dependent process similar to crystallization. Thus, it is also called "one dimensional crystallization" (*56*). The kinetics of amyloidogenesis often comprises of two stages: a lag phase corresponding to the thermodynamically-disfavored nucleation stage and an exponential, thermodynamically-favored stage corresponding to the elongation of the nucleus into mature fibrils (*57*) (Figure 8). Some amyloidogenic peptides have been found to show a shortened or fully vanished lag phase of amyloidogenesis in the presence of an external nucleus (*58*). For any amyloidogenic peptide, the nucleus formation is the rate limiting step of the fibrillation process.
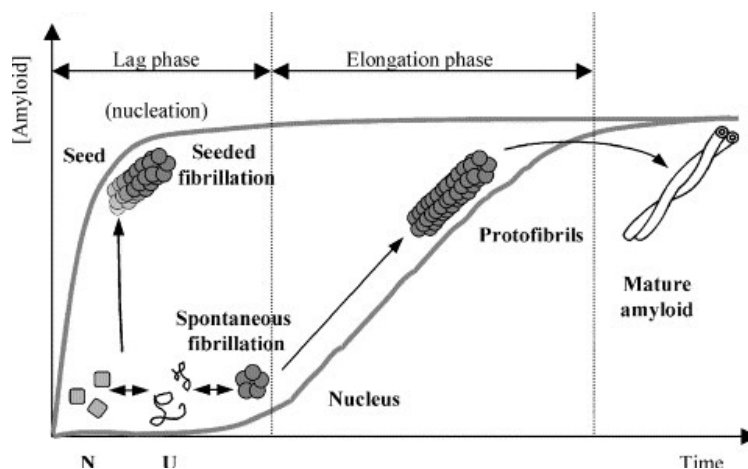
Figure 8: Kinetics of spontaneous and tuned (seeded) amyloidogenic self-assembly (adopted from Dzwolak, et al. 2006 (*57*)).

As mentioned in the previous sub-chapter (1.3), the side chain packing of the adjacent β-strands of amyloid fibrils plays an important role in the stability of the fibrils. An interesting question that arises is how do many polypeptides, whose sequences are evolved to fold into stable, globular structures, could be equally well accommodated into the same generic conformation of amyloid, i.e., a β-sheet-rich motif? This quest can be answered by

finding how efficient the nucleus of one amyloidogenic peptide can be for the fibrillation of another amyloidogenic peptide sequence. Additionally, this approach, the so-called "cross-seeding" approach, gives vital information about the possible involvement of one amyloidogenic disease in the onset of another amyloidogenic disease, like the possibility of the onset of Alzheimer disease to a T2DM patient, or *vice versa*. Figure 9 represents the very recent model of the cross-seeding approach, whereby Htt (huntingtin) fibrils seeded the fibrillation of TIA-1 (T-cell intra-cellular antigen-1, TIA-1 contains no poly(Q) tract), leading to pathological diversity (*59*).
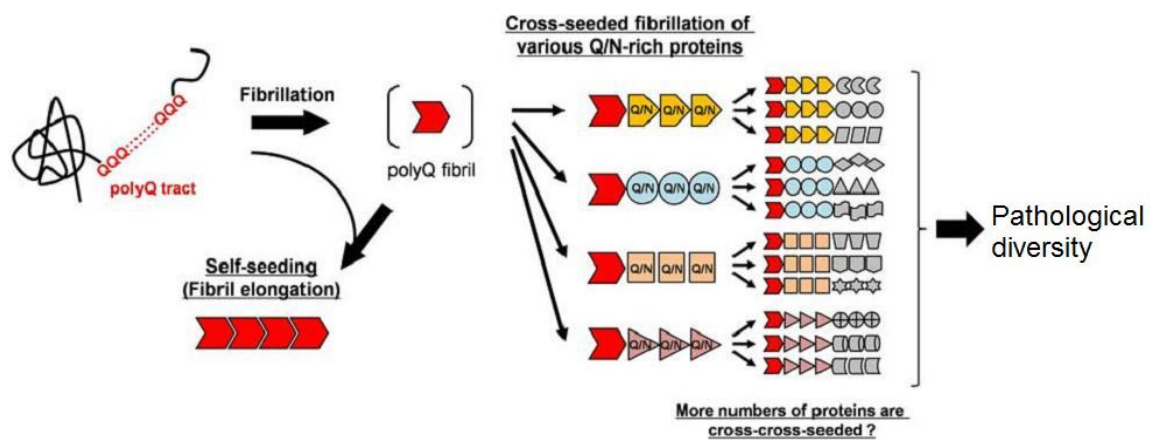
Figure 9: Model of pathological diversity based on a cross-seeding mechanism. An abnormally expanded poly(Q) tract forms fibrillar aggregates, which can induce fibrillation of Q/N-rich proteins by acting as a seed (cross-seeding). Various kinds of Q/N-rich proteins (designated as different shapes and/or colors) can be potentially recruited into the fibrillar aggregates through a cross-seeding reaction. Likewise, cross-seeded fibrils of Q/N-rich proteins may further facilitate fibrillation of the other proteins that can not be directly seeded by poly(Q) aggregates (cross-cross-seeding). Given that physiological functions of recruited proteins are repressed, cross-seeding reactions will describe diverse pathologies observed in the poly(Q) diseases (adopted from Furukawa, et al. 2009 (*59*)).

1.6. Aim of the research

Cellular membranes constitute the largest charged surface inside the cell. These cell membranes generally display a lateral heterogeneity in their lipid composition, in their inner and outer leaflet. The recent outburst of information in lipidomics shows a high level of spatial and temporal variability of membrane composition (*60, 61*). In addition, there have been more and more examples of biological processes in which the protein function depends on the intricate details of the membrane properties, e.g., the distribution of charged phospholipids in the membrane. On one hand, lipids may influence protein function by altering the physical properties of the lipid matrix. On the other hand, lipids may also affect

protein function by directly binding to certain sites on the proteins; thus, the composition of lipids is extremely important in studying any membrane associated biological processes. One such classical example, where changes in lipid composition of membranes have adverse implications, is Diabetes. In the prediabetic stage, an increased level of free fatty acids has been observed. This increased level of free fatty acid leads to the remodulation of membrane composition by significantly increasing the negatively charged lipid content. The anionic lipid content of the membrane has been found to increase beyond the physiological limit of 10-30%. Moreover, it has been hypothesized that proIAPP is involved in the intracellular amyloid deposits in the presence of negatively charged cellular moieties like heparin sulfate proteoglycans (21) (HSPG), non-esterified fatty acids (NEFA) (20), etc.

The aim of this research is to explore the amyloidogenic propensity of proIAPP and its conformational properties, in the presence of lipid membranes. Since no studies regarding proIAPP-membrane interaction have been reported so far, in the first step simple membrane-mimicking systems were studied, followed by model phospholipid membranes. The first part of this work is dedicated to establish the effect of a well-studied negatively charged membrane-mimicking agent, SDS (sodium dodecyl sulfate), on the amyloidogenic propensity and the conformational properties of proIAPP. The methodology used to accomplish this goal mainly involved circular dichroism spectrometry (CD), fluorescence spectrometry, and atomic force microscopy (AFM).

The second part of this project is an extension of the surfactant studies, in which the interaction between proIAPP and negatively charged phospholipids (POPG) has been explored. Here, the effects of negatively charged lipid monolayers on the amyloidogenic propensity and conformational properties of proIAPP at a surface pressure of 10 mN/m and 30 mN/m were studied, respectively. For this study, infrared reflection absorption spectroscopy (IRRAS) and AFM were used as main methods of investigation.

The third part of the project is built upon the information collected from the results of simple negatively charged membrane mimicking lipid and lipid monolayer systems on the amyloidogenic propensity of proIAPP. It aimed to study the effect of different compositions of negatively charged and zwitterionic lipid bilayer membranes on the amyloidogenic propensity and the conformational properties of proIAPP by means of ATR-FTIR

spectrometry, fluorescence spectrometry, and AFM. This is essential in order to reveal the possible mechanisms of prediabetic membrane involvement in intracellular proIAPP fibril formation.

The last part of this work includes the cross-seeding approach to explore the efficiency of other amyloidogenic peptides secreted by pancreatic β-cells, like IAPP and insulin, in seeding the fibrillation of proIAPP, and vice versa. To accomplish the goal of this part, fluorescence and ATR-FTIR spectroscopy, as well as AFM have been used. This "cross-seeding" approach would provide an *in vitro* proof of proIAPP involvement in the onset and progression of T2DM in human.

Chapter 2. Materials and Methods

2.1. Materials

2.1.1. Chemicals

1,1,1-trifluoroacetic acid	TFA	Merck
1,2-dioleoyl-2-oleoyl-*sn*-glycero-3-phosphatidylcholine	DOPC	Avanti Polar Lipids
1,2-dioleoyl-2-oleoyl-*sn*-glycero-3-[phosphor-rac-(1-glycerol)]	DOPG	Avanti Polar Lipids
1,2-dipalmitoyl-*sn*-glycerol-3-phosphatidylcholine	DPPC	Avanti Polar Lipids
1-palmitoyl-2-oleoyl-*sn*-glycerol-3-[phosphor-*rac*-(1-glycerol)]	POPG	Avanti Polar Lipids
Acetone		JT Baker
Acetonitrile		JT Baker
Acrylamid/Bisacrylamide (37.5:1, 30 % w/v)		Applichem
Ammonium persulfate	APS	Merck
Bromphenol blue		Serva
Chloroform	$CHCl_3$	Merck
Cholesterol	Chol	Sigma-Aldrich
Coomassie Brilliant Blue G250+R250		Serva
Deuterium oxide, 99.9 atom% D	D_2O	Sigma-Aldrich
Deuterium chloride	DCl	Sigma-Aldrich
Enterokinase enzyme	EK	Novagen
Ethanol		JT Baker
Ethidium bromide	EtBr	Sigma
Guanidine hydrochloride	GdnHCl	Calbiochem
Hexafluoro-2-propanol	HFIP	Fluka
Hydrochloric acid		JT Baker
Insulin from bovine pancreas	Insulin	Sigma-Aldrich
Imidazol		Gerbu
Islet amyloid polypeptide	IAPP	Calbiochem
Isopropyl-b-D-thiogalactopyranoside	IPTG	Applichem
Muscovite mica	Mica	Plano GmbH
Nickel-nitrilotriacetate resin	Ni-NTA	Sigma
N,*N*,*N'*,*N'*-tetramethylethylendiamin (TEMED)		Roth
Sodium chloride	NaCl	Sigma-Aldrich
Sodium phosphate dibasic	NaH_2PO_4	Sigma-Aldrich
Sodium phosphate monobasic	Na_2HPO_4	Sigma-Aldrich
Sodium dodecyl sulfate	SDS	Sigma-Aldrich
Thioflavin T	ThT	Merck
Yeast extract, Tryptone	YT	Gibco

All chemicals used for proIAPP purification were of HPLC grade. The plasmid (pET32_EK/LIC_ProIAPP) for the expression of proIAPP was a generous gift from Prof. Dr. Aphrodite Kapurniotu, Technical University of Munich, Germany. All other chemicals were used without further purification. For all experiments deionized water (Except IRRAS and FTIR measurements) with conductance > 18 MΩ cm was obtained from ELGA PURELAB Classica polisher system, ELGA Lab Water, Celle, Germany.

2.1.2. Proislet amyloid polypeptide (proIAPP)

Proislet amyloid polypeptide (proIAPP), also known as proamylin, is a 67 amino acid polypeptide, and is expressed in the β-cells of pancreas. The physiologically active part of this protein is very well known as amylin/islet amyloid polypeptide (IAPP), which is going to be discussed in the following sub-chapter. ProIAPP has been found to be a part of the intracellular amyloid deposits in transgenic mice expressing the gene for human IAPP (20). There are plenty of references, where the factors affecting the amyloidogenic propensities of hIAPP have been studied. It has been demonstrated that the N-terminal extended proIAPP sequence interacts with the negatively charged surface present inside the cell, like HSPG. However, there has not been much of exploratory work of the possible factors that can induce these intracellular amyloid deposits of proIAPP, and initiate the extracellular amyloid deposits by using these intracellular fibrils as nucleus for IAPP/insulin fibril formation. Figure 10 depicts the amino acid sequence of proIAPP.

TPIESHQVEKRKCNTATCATQRLANFLVHSSNNFGAILSSTNVGSNTYGKRNAVEVLKREPLNYLPL
              + ++   +   - ++ -   ++   -

Figure 10: The primary sequence of proIAPP (adopted from Abedini et al. (*62*)).

2.1.3. Islet amyloid polypeptide (IAPP), insulin

Islet amyloid polypeptide (IAPP) is a 37 amino acid long polypeptide, which is also known as amylin. It is a hormone secreted by the β-cells of the pancreas in response to the various stimuli due to increased blood glucose level. It acts as an antagonist to insulin, another hormone secreted by the same pancreatic β-cells to decrease the blood glucose level. Both, IAPP and insulin are co-stored and co-secreted into the extracellular matrix.

They are also expressed as prohormone, and processed by the same enzymes. Figure 11 depicts the amino acid sequence of IAPP and insulin with disulfide bonds.

A)   IAPP

KCNTATCATQRLANFLVHSSNNFGAILSSTNVGSNTY-NH$_2$
  +   +

B)   Insulin

Figure 11: Amino acid sequence of (A) IAPP (adopted from Abedini, et al. (*62*)), and (B) insulin (adopted from Nielsen, et al. (*63*)).

2.2.   Methods

2.2.1. Transformation by electroporation

An amount of 50 µL of the electro-competent cells, *E. coli* BL21(DE3), was incubated with approximately 1 ng of the plasmid DNA, pET32_EK/LIC_ProIAPP (a gift from Prof. Dr. Aphrodite Kapurniotu, Technical University of Munich, Germany), in a chilled electroporation cuvette (0.2 µm path length). Thereafter, a high voltage pulse was applied (25 µF, 200 Ω, 2.5 kV) using an *E. coli* Pulser from Biorad. The cells were immediately transferred into 1 mL of LB (Luria-Bertani broth) medium and incubated for 1 h at 37 °C. After one hour, the incubated cells were centrifuged and the supernatant was discarded, the remaining pellet was resuspended in 100 µL of LB medium and plated on an agar plate containing ampicillin as selection marker.

2.2.2. Protein expression

A single colony of transformed *E. coli* BL21(DE3) cells was picked from an agar plate using a sterile inoculating loop, and inoculated into 100 mL of LB-medium containing 100 mg/L of ampicillin. This inoculated sample was kept at 200 rpm in a rotatory shaker at

37 °C overnight. The pre-culture was then used to inoculate 6 L of 2x YT medium containing 100 mg/L of ampicillin. Cells were left to grow until the $OD_{600 \, nm}$ of the medium reached 0.6 at 37 °C, 200 rpm. At this point, the proteomics of growing cells was induced by adding IPTG (isopropyl β-D-1-thiogalactopyranoside) to a final concentration of 1 mM, and the cells were left to grow for additional 3 h prior to harvest the cells. Before harvesting the cells, 30 µL of sample was mixed with 2x SDS sample buffer and boiled at 95 °C for 10 min, and run on a denaturing sodium dodecyl sulfate poly-acrylamide gel electrophoresis (SDS-PAGE) to estimate the protein expression level (Appendix Figure A). Further, the medium was distributed into 600 mL aliquots, and the cells were centrifuged at 4000 g for 15 min at 4 °C by using an Allegra^{TM} X-22R centrifuge (Beckmann coulter, Germany). The cells were washed with 25 mM Tris-HCl buffer, pH 8.0, containing 50 mM of NaCl and centrifuged at 3000 g for 30 min. Thereafter, the supernatants were discarded, and pellets were stored at -80 °C for further purification of the fusion protein containing the primary sequence of proIAPP.

2.2.3. Protein purification

The pellet stored at -80 °C was thawed and dissolved in 25 mM Tris-HCl buffer (pH 8.0) containing 50 mM NaCl up to a final volume of 15 mL. Cells were broken by three cycles in a microfluidizer (Microfluidics Corporation, Newton, MA). The degree of cell lysis was checked by a microscope. The cell lysate was immediately diluted with 8 M GdnHCl in 10 mM Tris-HCl (pH 8.0), 100 mM NaCl, to a final concentration of 6 M GdnHCl. Here, the role of GdnHCl was to avoid the aggregation of the fusion protein containing the primary sequence for proIAPP. The resultant clear solution was centrifuged at 48000 g for 30 min at 7 °C using an ultracentrifuge Optima L-70K (Beckman Coulter), and the supernatant was stored for further purification steps. The supernatant was loaded on a 15 mL Ni-NTA (Nickel-nitrilotriacetate) resin, which was equilibrated with a gradual increasing concentration of GdnHCl from 0 to 6 M in 10 mM Tris-HCl buffer (pH 8.0), 100 mM NaCl. The His-tag of the fusion protein containing the primary sequence of proIAPP forms the co-ordinate bond with the Ni^{2+} present in the resin, and the rest of the unbound proteins was washed away with a decreasing gradient of GdnHCl from 6 to 0 M in 10 mM Tris-HCl buffer (pH 8.0), 100 mM NaCl. After washing with 10 mM Tris-HCl buffer (pH

8.0), 100 mM NaCl (without GdnHCl), the bound fusion protein was eluted with 100 mM imidazole in 10 mM Tris-HCl (pH 8.0) containing 100 mM NaCl. The eluate was dialysed against 50 mM Tris-HCl, pH 8.0, 50 mM NaCl, and the resulting precipitate was immediately dissolved to a final concentration of 4 M GdnHCl, 10 mM Tris-HCl, pH 8.0, and 100 mM NaCl. The resulting protein solution was loaded on a C18 column (ProntoSIL HPLC, Germany) for further purification by reverse-phase high performance liquid chromatography (RP-HPLC) on a Waters 600 chromatography instrument equipped with a Waters 2487, dual λ absorbance detector (Waters, Milford, MA, USA). The eluate during sample loading, washing, and elution was checked for the fusion protein, having a weight of 24.4 kDa, by SDS-PAGE, as well as by liquid chromatography-electron spray ionization-mass spectrometry (LC-ESI-MS). The elution gradient used was: 10 min at 10% buffer B (90% acetonitrile, 0.05% TFA in H_2O) in 90% buffer A (0.06% TFA in H_2O; 60 min from 10% to 90% buffer B in buffer A). The flow rate was 2 mL/min, which was maintained throughout the run, and the detection of the fusion peptide was performed at 214 nm. The fusion protein fraction was confirmed by ESI-MS (Appendix Figure B), then lyophilized and dissolved in an enterokinase cleavage buffer (20 mM Tris-HCl, pH 7.5, 50 mM NaCl, 2 mM $CaCl_2$). The cleavage reaction was performed for 16 h at room temperature (20 °C) with an enterokinase (EK) enzyme. The cleavage product was lyophilized, then dissolved in 10% acetic acid and purified on RP-HPLC with the same elution profile as for the fusion protein. The purity and identity of human proIAPP, having a weight of 7514 Da, was determined with SDS-PAGE (Appendix Figure A) and ESI-MS (Appendix Figure C) (LCQ Advantage MAX, Thermo). The protein concentration was estimated from the absorbance at 280 nm in water, using an extinction coefficient of 3230 M^{-1} cm^{-1} (*64*). Following the concentration determination, the proIAPP fraction was dissolved in 100 % TFA and then distributed to aliquots and lyophilised. It was stored at -20 °C for further use.

2.2.4. Sodium dodecyl sulfate – polyacrylamide gel electrophoresis (SDS-PAGE)
Preparation of SDS-PAGE

The resolving gel was prepared by mixing the individual components as indicated in Table 2 (shown below), APS and TEMED were added to start the polymerization. Thereafter, the solution was poured into a Biorad Multi-casting apparatus, and 50%

isopropanol on the top of the resolving gel and the resolving gel solution left to polymerize at room temperature. After polymerization of the resolving gel (*ca.* 30 min), the isopropanol was removed from top, and the stacking gel solution was added on top of the resolving gel. Further the comb was inserted immediately, and again left to polymerize at room temperature (ca. 30min).

Table 2: Recipe for preparing the SDS-PAGE gels.

Adding sequence	1	2	3	4	5	6
Type of gel (%)	acrylamide/ bisacrylamide (29:1, 30%)	Mili-Q H$_2$O	Resolving gel buffer (4x)	Stacking gel buffer (4x)	10% APS*	TEMED*
Resolving gel (60 mL)						
10%	20 mL	25 mL	15 mL	-	300 µL	30 µL
15%	30 mL	15 mL	15 mL	-	300 µL	30 µL
Stacking gel (30 mL)						
5%	5 mL	17.5 mL	-	7.5 mL	240 µL	30 µL

*TEMED: N,N,N',N'-tetramethylethylendiamine. ***APS:** ammoniumpersulfate.
Resolving gel buffer: 1.5 M Tris-HCl, pH 8.8; 0.4% (w/v) SDS. **Stacking gel buffer:** 0.5 M Tris-HCl, pH 6.8; 0.4% (w/v) SDS. **Running buffer (10x):** 0.25 M Tris-HCl (pH 8.0); 2 M Glycine; 1% SDS.

Gel electrophoresis

The protein samples were prepared by adding an equal volume of SDS-PAGE sample buffer (2x) (62.3 mM Tri-HCl, pH 6.8; 2% w/v SDS; 10% v/v glycerol; 5% v/v β-mercaptoethanol; 0.001% w/v Bromophenol blue). After heat treatment (60 °C for 5 min), the mixtures were loaded on SDS-PAGE, and run at 80 V direct current (DC) until the bromophenol blue front entered the buffer solution. SDS-PAGE was stained with coomassie staining solution (10% v/v acetic acid; 40% v/v ethanol; 0.1% w/v Comassie Brilliant Blue R250) by heating for 2-3 min in a microwave, followed by 1 h on a shaker at room temperature. The stained gel was de-stained by keeping it overnight in destaining solution (10% v/v acetic acid) at room temperature.

2.2.5. LC-ESI-mass spectrometry

Liquid chromatography-electrospray ionization-mass spectropmetry (LC-ESI-MS) analysis was performed on an Agilent 1100 series chromatography system (Hewlett Packard) equipped with an LCQ ESI mass spectrometer (Finnigan, San Jose, USA) using Vydac 214TP C4 columns (5 µm, 15 x 0.46 cm, 300 Å pore-size) from Phenomeney (Aschaffenburg, Germany). For LC separation, a gradient of buffer B (0.1% formic acid (FA) in acetonitrile (ACN)) in buffer A (0.1% formic acid in water) with a constant flow rate of 1 mL/min was applied, with a gradient program as shown in Table 3. Under these conditions, the fusion protein was eluted at 14 min. Mass spectra evaluation and deconvolution was performed using the Xcalibur software package and Mag Tran software (*65*). The accuracy of the method for proteins within 25 kDa is approximately ±1-2 Da.

Table 3: The gradient program for LC-ESI-MS measurements of proteins using a C4 column.

Time (min)	buffer A (0.1% FA, H$_2$O) %	buffer B (0.1% FA, ACN) %
5	20	80
15	70	30
17	90	10
19	90	10
20	20	80
22	20	80

2.2.6 Preparative reverse-phase (RP) – HPLC

Preparative reversed-phase (RP) chromatography was performed on a Waters 600 chromatography instrument equipped with a Waters 2487 absorbance detector. ProntoSIL C18 column (5 µm, 25 x 0.8 cm, 200 Å pore-size) from ProntoSIL HPLC Germany, was used for RP-HPLC. For RP-HPLC the gradient of buffer B (0.1% TFA in Acetonitrile) in buffer A (0.1% TFA in water) at a flow rate of 2 mL/min was applied using a gradient program described in Table 4. Under these conditions, the fusion protein was eluted at *ca.* 38 min, while proIAPP was eluted at *ca.* 34 min.

Table 4: The gradient program used for RP-HPLC measurements using a C18 column, while the flow rate (2 mL/min) was kept constant throughout the gradient.

Time (min)	buffer A (0.1% TFA, H$_2$O) %	buffer B (0.1% TFA, ACN) %
10	30	70
15	90	10
10	90	10
60	10	90
70	30	70

2.2.7. UV-Vis Spectrometry

The ProIAPP concentration was measured by following the absorption at $\lambda_{280\ nm}$ on PerkinElmer lambda25 model spectrometer (PerkinElmer, USA), and then employing the Beer-Lambert's law. According to the Beer-Lambert's law, the transmission (*T*) of light through a substance is the product of the molar absorption coefficient of the substance, ε, the concentration *c*, and the distance the light travels through the substance, *l*, i.e., $T=I/I_o=10^{-\varepsilon lc}$. The absorption coefficient (*A*) of the substance is given by $A = \varepsilon lc$.

The molar absorption coefficient, ε, for proIAPP was calculated from its amino acid sequence (*64*), which was found to be 3230 M^{-1} cm^{-1} at 280 nm. The path length, *l*, of light that passed through the protein sample was 3 mm.

2.2.8. Fluorescence Spectrometry

Luminescence is the emission of light from any substance, and occurs during the transition from an electronically excited state to the ground state. Depending on the nature of the transition, it is divided into fluorescence and phosphorescence. The electrons of a fluorophore excite by absorption of energy, and attain a higher energy orbital. The electron in the excited orbital remains unpaired, and of opposite spin compared to the electron in ground state orbital. Consequently, the high energy orbital unpaired electron returns to the ground state orbital as a result of spin pairing of electron ("spin allowed"), and this transition occurs very rapidly by emission of a photon corresponding to a lower energy than the absorbed photons. This property of a fluorophore is called fluorescence. The emission rates of fluorescence are typically 10^8 s^{-1}, so that a typical fluorescence lifetime is near 10 ns; the life time (τ) of a fluorophore is the average time between its excitation and return to the ground state. On the other hand, phosphorescence is the emission of light from triplet

excited states, in which the electron in the excited orbital has the same spin orientation as the ground-state electron. The emission rates are slow, typically 10^3 - 10^0 s^{-1}, so that phosphorescence lifetimes are typically in the range of milliseconds to seconds. Sensitivity at the scale of nanoseconds has made fluorescence a powerful technique for studying bio-molecular interactions. The technique has become quite popular also because of its exquisite sensitivity to the immediate environment of the probe, and due to the generally high signal to noise ratio (*66*).
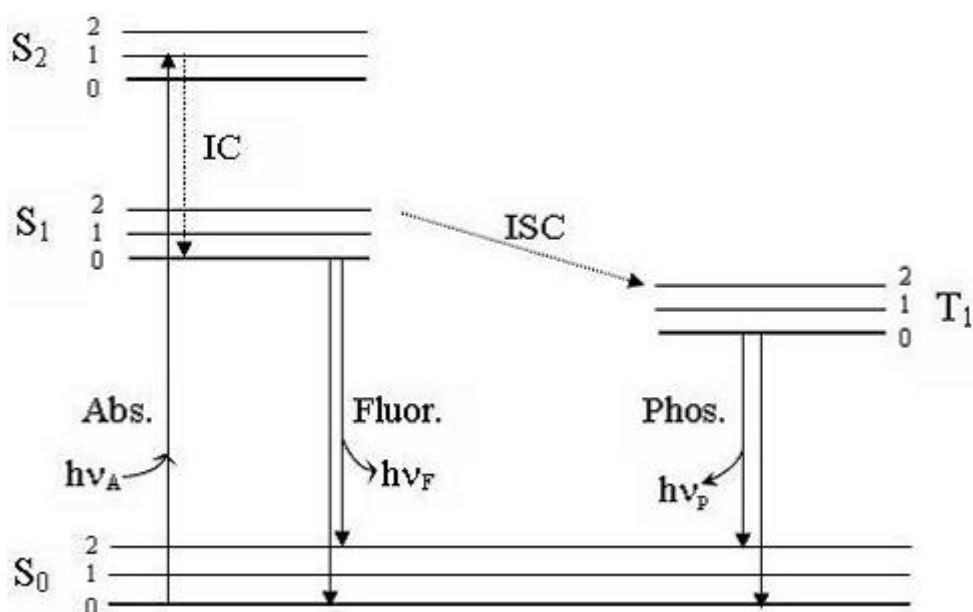

Figure 12: Jablonski diagram (*67*). Symbols from the diagram: S_1, S_2, and S_0 stand for the singlet states of the excited states 1, 2, and of the ground state, respectively. IC stands for internal conversion. ISC stands for intersystem crossing, while T_1 stands for triplet state; $h\nu_A$, $h\nu_F$, $h\nu_P$ stands for the energy of absorbance, fluorescence, and phosphorescence, respectively.

2.2.8.1. Thioflavin T: a fluorescent dye and its applications

Thioflavin T (ThT) is a cationic benzothiazole dye that has a special affinity towards amyloid fibrils (*68*). On binding to amyloid fibrils, the fluorescence characteristic of this benzothiazole dye changes. Unbound ThT has its excitation maximum at 385 nm, and the emission is at 445 nm. Upon interaction with fibrillar or prefibrillar structures, the excitation maximum shifts to 450 nm and the emission maximum to 482 nm, respectively (*69-71*). Due to the specificity of ThT binding to amyloid fibrils, it has found many

applications such as diagnosis of amyloid fibril formation *in vivo* by using fluorescence microscopy (*68, 72*), monitoring extracted amyloid fibrils and *in vitro* amyloid fibrils formation using fluorescence spectrophotometry (*69, 70*), and direct observation of amyloid fibril growth using total internal reflection fluorescence microscopy (*73, 74*). The chemical structure of ThT (Figure 13) has a hydrophobic and a relatively polar end.
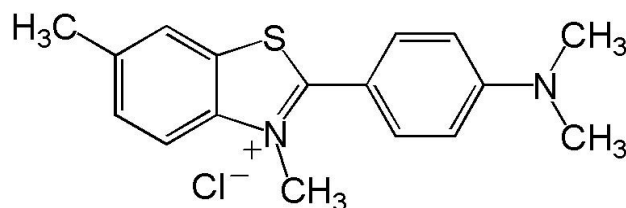

Figure 13: Chemical structure of thioflavin T (*70*).

The polar end of ThT is a polar benzothiazole group consisting of polar atoms such as N and S. It has been suggested that the polar nitrogen of thiazole dye forms hydrogen bonds with the hydroxyl groups of tissue structures and causes the above mentioned transitional shifts in fluorescence characteristics of the dye (*75*). However, there is not much known about the binding mechanism of ThT to amyloid fibrils.

For this project, ThT has been employed to follow the fibrillation kinetics of proIAPP in the absence and presence of SDS, LUVs, lipid rafts and seeds from different amyloidogenic peptides/proteins by fluorescence spectroscopy. For the SDS experiments, 10 µM ThT was used, while the fibrillation kinetics in the presence of LUVs, lipid rafts and seed reactions were followed with 50 µM of ThT in the reaction mixture.

The fluorescence emission intensity of ThT was measured using a K2 multifrequency phase and modulation fluorometer with photon counting mode equipment (ISS Inc., Champaign Ill, USA). Figure 14 represents the typical set up of a K2 fluorescence spectrophotometer.
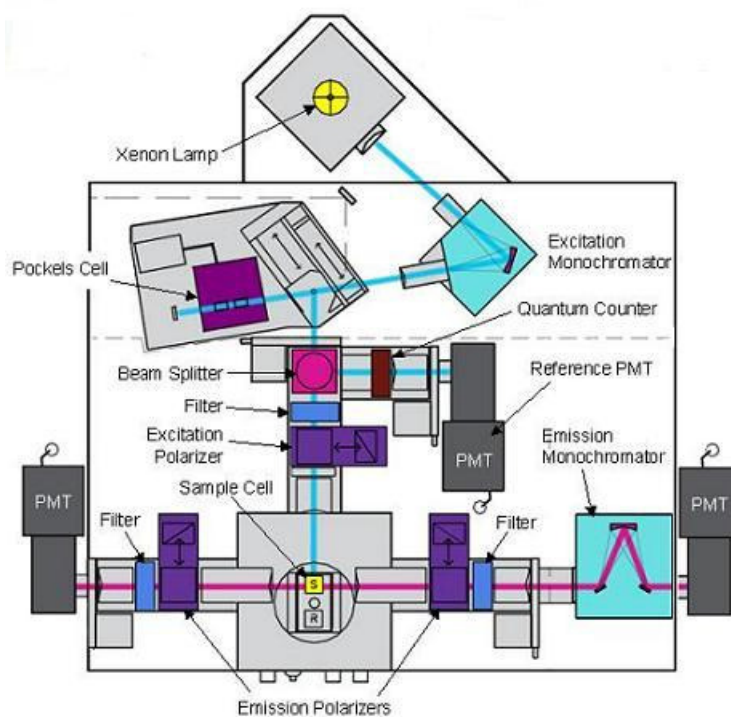
Figure 14: A schematic representation of the K2 fluorescence spectrophotometer (courtesy of ISS, Inc.).

The instrument has a xenon arc lamp as the source of excitation light, having a spectrum between 190 and 1100 nm. This xenon lamp emits a continuous light beam, as a result of recombination of electrons with ionized xenon (Xe) atoms. These charged Xe atoms are generated by the collisions of atoms with the electrons flowing across the arc. This continuously emitted light is focused with the help of lenses on the entrance slit of the excitation monochromator. A monochromator accepts the incoming light and disperses it into the various colors of the spectrum. This dispersion can be accomplished using prisms or diffraction gratings. In the K2 spectrophotometer, the spectral dispersion is achieved by means of holographic gratings with 1200 grooves per millimeter. The spectral region is in the range of $\lambda = 200 - 800$ nm with allowance of $\Delta\lambda = 0.25$ nm. Both monochromators are equipped with a set of interchangeable slits of 2, 1, 0.5 mm, respectively. Since the linear dispersion of the monochromator is 8 nm/mm, slits have a bandwidth of 16 nm, 8 nm and 4 nm. The monochromatic light is stirred afterwards over a mirror which is fastened to the corner of a two-way polarizer, directly on a beam splitter. A beam splitter is provided in the excitation light path, which reflects part of the excitation light to a reference cell, in this rhodamine-B, a stable reference fluorophore. The excitation spectra are distorted primarily

by the wavelength dependence of the intensity of the exciting light. This intensity can be converted to a signal proportional to the number of incident photons by the use of a "quantum counter". This concentrated solution absorbs virtually all incident light in the range of 200 - 600 nm. The quantum yield and emission maximum (~ 630 nm) are essentially independent of the excitation wavelength from 220 – 600 nm. Rhodamine-B remains the most reliable and convenient "quantum counter".

Polarizers are present in the both excitation and emission light paths. Generally, the polarizers are removable so that they can be inserted only for the measurement of fluorescence anisotropy or when it is necessary to select a particular polarized component of the emission and/or excitation. In the sample space, there are two possibilities for inserting cells, either the cuvette holder with thermostat or the high-pressure autoclave. In the right emission channel, light emitted by the sample is spectrally divided by the emission monochromator. Like the excitation monochromator, the emission monochromator also contains concave holographic gratings with 1200 grooves per millimeter as a dispersive element. The emission monochromator grating is maximized for fluorescence light detection in the region 350 - 800 nm. Additionally, the slits for optical filters are indicated in both, left and right, emission paths directly behind the polarizer and the monochromator, respectively. Optical filters are used to compensate for the slight fluctuation from ideal behaviour of the monochromators. The detection of the emission light is facilitated by two photomultipliers, on the left and on the right side of the sample area. The emitted fluorescence radiation is focused first by a lens. The focused emission radiation passes through a monochromator and filters to the detector. Most of the fluorometers use photomultiplier tubes (PMTs) as detectors. These PMTs are regarded as extremely sensitive detectors of light in the ultraviolet, visible, and near-infrared ranges. Since these detectors multiply the current produced by received light by million times, enabling individual photons of received light to be detected when the incident flux of light is very low. Although a PMT responds to individual photons, these individual pulses are generally detected as an average signal.

2.2.9. Circular dichroism spectrometry

An electromagnetic radiation is composed of two mutually perpendicular field vectors, an electric and magnetic field vector. These field vectors align at 90° to the axis of propagation of the electromagnetic radiation. By convention, the polarization of light is described by specifying the direction of the radiation's electric field vector, as shown in Figure 15.
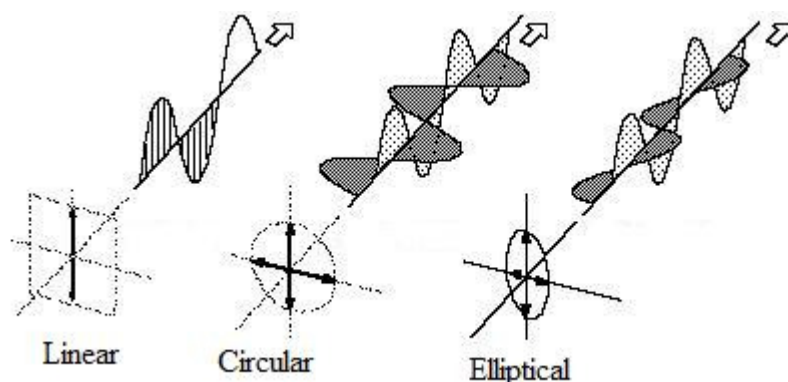

Linear   Circular   Elliptical

Figure 15: Schematic diagram of linear, circular, and elliptical polarized light propagation.

When electric field vectors are aligned in one direction, the radiation is called linearly polarized radiation or plane polarized light. While, when the electric field vector keeps rotating as the wave propagates, the radiation is called circular or elliptical polarized light. In the latter case, the amplitude of rotating electric field vector determines the nature of polarization. If the amplitude is the same, it is called circularly polarized light, if not then it depends upon the magnitude of the amplitude of the two perpendicular component vectors of the rotating electric field. It can be rightward or leftward, which in turn depends upon the molar absorption coefficient of a compound towards the circular polarized light. Only certain compounds have such characteristics, i.e. different molar absorption coefficient for left and right circular polarized light. These compounds are called "chiral" or optically active compounds. In a protein, the peptide bonds [-(O)C-N(H)-] are the chiral centers in the protein molecule.

A circular dichroism (CD) spectrometer is used to measure the interaction of polarized light with the optically active compounds (asymmetric compounds). Asymmetry can result from a chiral center (as mentioned above, a peptide bond of a protein molecule), a non-chiral molecule (aromatic amino acid side chains) covalently attached to a chiral

molecule, or a non-chiral molecule in an asymmetric environment (a chromophore bound to a protein). Proteins are optically active molecules, as the peptide bonds have a chiral center, as well as all amino acids contain at least one chiral center, except glycine. The resulting CD signals are sensitive to the arrangement and coupling of those peptide bonds in different secondary structures (far-UV CD), and packing of side chains in the tertiary structure (near-UV CD). The secondary structures of proteins interact preferentially with one circular polarization, allowing one to follow the changes in protein structure using circular dichroism spectrometry.

By definition, CD is a measure of the differential absorbance between the left and right circularly polarized light:

$\Delta A = \Delta \varepsilon l c$, where $\Delta \varepsilon = \varepsilon_l - \varepsilon_r$

Therefore, it would be logical to use $\Delta \varepsilon$ as CD data. However, for historical reasons, the CD data are often expressed not as $\Delta \varepsilon$ but in terms of the molar ellipticity, i.e. $\theta(\lambda)$, which has units of deg cm^2 dmol^{-1}. When plane polarized light passes through a solution of optically active compounds, the left and right circularly polarized components of the plane polarized light are absorbed by different magnitudes. When these components are recombined, they appear as elliptically polarized light. The ellipticity is the angle θ, the tangent of which is the ratio of the minor to major axis of the ellipse.

CD spectra of proteins and peptides are usually measured in two spectral regions. In the far-UV region (180 - 260 nm), the measured bands represent the electronic transitions of the amide bonds of the protein backbone. The sign, magnitude, and position of these bands are strongly dependent on the arrangements of the peptide bonds in different secondary structures. Thus, the CD spectra in the far-UV region provide information about the content of secondary structures or changes in the secondary structure content of a protein in solution. Moreover, the near-UV region (250 - 350 nm) accounts for the packing of side chains of aromatic amino acids and disulfide bonds. Thus, the near-UV CD signal depends upon the local environment of the aromatic amino acid side chains and their packing/orientation with respect to the backbone of the protein.

2.2.9.1. Far-UV CD spectra and protein secondary structure

The most stable and abundant elements of regular, secondary structures are α-helices, parallel and antiparallel β-sheets (*38*). All proteins can be grouped into five classes according to their secondary structures:

1) All α proteins, which show a strong double minimum in the CD spectra at 222 nm, 208 ±2 nm, and a strong maximum at 191 ±2 nm.

2) All β proteins have a single negative minimum at 216 ±3 nm and a single positive maximum between 190 nm and 200 nm. In contrast, a highly distorted β-sheet or β-sheets made up of short irregular β-strands show a strong negative band near 200 nm, similar to unordered forms (*76*).

3) Proteins with both, α and β, conformation but in separate domains.

4) Proteins with intermixed strands of α/β conformations along the polypeptide chain.

5) Unordered or denatured proteins have little ordered conformations; they show a strong negative band near 200 nm and some week bands between 220 nm and 230 nm, which can have either positive or negative signs.

For α+β and α/β proteins, the ellipticity of α-helices predominate that of β-sheets. However, in a few cases a single broad minimum CD band may appear between 210 nm and 220 nm because of the overlapping ellipticity signal of various α-helices and β-sheets. For α+β proteins, the 208 (±2) nm band ellipticity is higher than the 222 nm band, and the reverse is true for the α/β proteins (*77*).

The estimation of the secondary structure of a protein from its CD spectrum remains an empirical task, despite of many programs proposed to analyze the data. This is because of the lack of a unique solution for the deconvolution of a CD spectrum. Most of the deconvolution methods assume that the spectra are a linear combination of reference spectra for the five secondary structures (helical conformation, parallel and antiparallel β-sheet, β-turn and random coil). A relatively new program, circular dichroism neural network (CDNN) has been recently established as an alternative to the statistical methods (*78*).
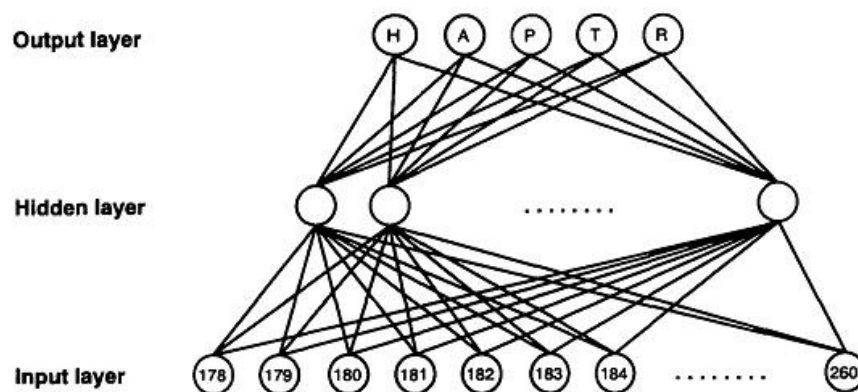
Figure 16: Schematic topology of a NN (neural network). Data are presented to the input layer; for each data point (at each wavelength) there is a separate processing element (neuron), which processes the data and send the result via weighted connections to each neuron in the next layer (hidden layer). The adaptation of weights is performed in the learning phase. The output consists of five neurons that represents the five fractional states (*78*).

This program uses a back-propagation network model (*79*) with a single hidden layer between input and output (Figure 16), to deduce the five different secondary structures with satisfactory correlations between calculated and measured secondary structure data. As shown in Figure 16, in this program neuron of a given layer is connected to all neurons in the next layer through randomly weighted (numerical weight) connections. Information is passed though these connections and processed in the neurons by adjusting the numerical weights iteratively, through back-propagation method (*79*), until all patterns presented to the input layer are correctly projected on the output layer in the training phase of program. These adjustments of numerical weights come from the difference in the actual output and the calculated output, i.e., residual error. Thus, the back-propagation algorithm of the network is repeated until the residual error in the output layer reaches a minimum. This neural network program represents the relatively most elegant method of non-algorithmic deconvolution of experimental CD spectra. Moreover, direct comparison of different methods is not possible because of the different reference spectra and algorithms that are used by different methods.

2.2.9.2.   Sample preparation and instrument set-up - CD

Aliquots of proIAPP were dissolved in the respective reaction buffer, and the CD spectra were measured with a J-715 model from JASCP (Easton, MD) under constant nitrogen flush. The parameters used for the CD measurements are given in Table 5.

Table 5: Parameter used for all CD measurements.

CD parameters	
Sensitivity	Standard (100 mdeg)
Start wavelength	260 nm
End wavelength	190 nm
Data pitch	1 nm
Scanning mode	Continuous
Scanning speed	50 nm/min
Response	2 sec
Band width	1.0 nm
Accumulation	5

Each CD spectrum is an average of 5 scans. An external water thermostat was used to control the temperature within ±0.1 °C. After each measurement, the CD spectra were normalized, baseline corrected, and translated into mean residue ellipticity (MRE) by using the spectra analysis software from Jasco. The secondary structure content of the peptide was determined using a CD spectrum deconvolution program, CDNN (*78*), using 66 input neurons for wavelengths from 190 to 260 nm, five output neurons for the secondary structure elements, and one hidden layer with 45 neurons (*78*).

2.2.10. Infrared spectrometry

One of the best ways to recognize any compound, or changes in its conformation is through the functional groups present in the compound. Currently, several methodologies have been established to understand kinetic processes by following the functional groups, like Infrared spectrometry (FTIR, IRRAS). The bonds in a molecule are dynamic in nature. The nature of this dynamicity includes symmetric, asymmetric stretches, and bending vibrations either in-plane or out-of-plane. The frequency of these motions falls in the infrared region of the electromagnetic spectrum. When these bonds are exposed to infrared radiation, energy is absorbed by the particular bonds, corresponding to their respective resonance frequency. This change is observed by infrared spectrometers (IRRAS, FTIR). For example, a C-H bond displays stretching vibrations around 3000 - 2840 cm^{-1}. Depending upon its vicinity from the neighboring group, the frequency of the bond vibration varies. Similarly, the C=O, N-H groups of the peptide bond have their unique

vibration bands in the IR spectrum. Opaque samples are difficult to analyze in the usual absorbance mode. Other techniques such as attenuated total reflection Fourier transform infrared spectroscopy (ATR-FTIR), or infrared reflection absorption spectroscopy (IRRAS) proved to be very useful in this case.

2.2.10.1. Infrared reflection absorption spectroscopy (IRRAS)

IRRAS can be used to monitor a wide range of functional groups present on the surfaces (like lipid membranes), in addition to their orientation on the surfaces. This technique is typically applied to thin films on highly reflective surfaces, therefore often applied to self assemble monolayers (SAMs) on the solid surfaces like Teflon, gold, etc. Since infrared radiation is incident at grazing angle in IRRAS, it is also known as grazing-angle infrared spectroscopy (GARIS). At this incident angle, the electric vectors of p-polarized light interacts constructively and gives a better intensity signal for IRRAS spectra. On the other hand, the electric vector of s-polarized infrared radiation is negligible at all angles, since it undergoes a 180° phase shift relative to each other (parallel and perpendicular components), therefore cancels through the destructive interface, resulting in negligible absorbance. Thus, the only active vibrations observed, consist of bonds vibrating in the direction normal to the solid surface. These properties of IRRAS make it a valuable method to study lipid-protein interactions by analysis of the amide-I and –II bands, and is the only method capable of monitoring directly the protein's secondary structure, in situ, and its orientation associated with lipid films, also in a time-dependent fashion and as a function of the lipid monolayer pressure (*22*). Although IRRAS spectra provide information in terms of frequencies and intensities, molecular structures and interactions are interpreted from the frequency, while the protein structure and interaction details are studied by following the frequency of the amide-I band, mostly due to the C=O stretching of the peptide bond. Moreover, quantitative analysis of the intensity data provides information about the molecular structure's orientation. Some of the studies with IRRAS have provided data on acyl chain orientation as a mean tilt from the surface normal in ordered phospholipid (*22*), and fatty acid monolayer films (*80*).

2.2.10.2. Instrumentation and experimental part - IRRAS

IRRAS spectra were recorded with an Equinox 55 FTIR spectrometer (Bruker, Karlsruhe, Germany) connected to an XA 511 reflection attachment (Bruker) with an external narrow band mercury-cadmium-telluride (MCT) detector using a trough system (*81*). The infrared light was focused onto the D_2O-liquid interface and different angles of incidence could be adjusted. The trough system was positioned on a movable platform to shuttle the focus beam from sample to reference trough without any interference from absorption of infrared light by water vapor (*82*). Two Teflon troughs of different sizes (300 x 60 x 3 mm^3 and 60 x 60 x 3 mm^3 for sample and reference trough, respectively) were linked by three small water-filled bores to ensure equal height of the air-water interface in both troughs. The temperature of the subphase was maintained at 20 ±0.5 °C, and a Plexiglass hood covered the trough to minimize the evaporation of water (Figure 17) (*81*).
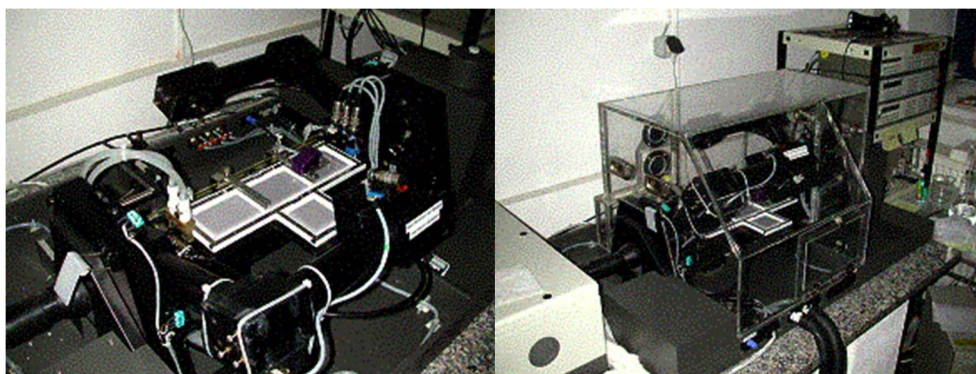

Figure 17: IRRAS apparatus: Top view (left) and with attached plexiglass box (right), employed to follow the proIAPP aggregation in the presence of lipid monolayers (*courtesy to* Dr. A. Kerth, Martin-Luther-University, Halle-Wittenberg, Halle / Saale, Germany).

All experiments were performed in the small (reference) trough, the large trough filled with buffer solution (10 mM NaH_2PO_4 and 100 mM NaCl), only. Protein adsorption experiments at the air-D_2O interface were started by filling the protein-containing buffer solution into the small trough just before running the infrared reflection absorption measurements. The lipid-protein interactions were studied at constant surface area by filling the protein-containing buffer solution into the small trough. Then the uppermost thin layer of the air-protein-buffer interface was sucked off just before the lipid monolayers were formed by directly spreading the lipid solution (POPG, ~ 1 mM) in a mixture of chloroform and methanol (3:1) onto the subphase until the required surface pressure was reached. The

lyophilized proIAPP aliquot was dissolved in 10 mM NaH_2PO_4 buffer, containing 100 mM NaCl, to obtain a final concentration of 1 µM (1.67 µM in the case of proIAPP$_{Ser13,18}$) before the start of the experiment.

2.2.10.3. Attenuated total reflection Fourier transform infrared spectroscopy (ATR-FTIR)

Attenuated total reflection Fourier transform infrared spectroscopy (ATR-FTIR) is one of the most powerful methods for recording IR spectra of biological materials in general, and for biological membranes in particular. It is fast, yields a strong signal with only a few micrograms of sample, and most importantly, it yields information about the orientation of various parts of the molecule under study to be evaluated in an oriented system. The environment of the molecules can be modulated so that their conformation can be studied as a function of temperature, pressure, as well as in the presence of membrane surfaces. A unique advantage of IR spectrometry is that it allows a simultaneous study of the structure of lipids and proteins in intact biological membranes without introduction of foreign perturbing probes. Additionally, because of the long infrared wavelength, light scattering problems are virtually nonexistent; thus, highly aggregated materials or large membrane fragments can be investigated.

In an ATR-FTIR spectrometer, there is an internal reflection crystal (for example, Ge, Si) that is covered with lipid layer(s) or sample to be studied, containing reconstituted protein or amyloid fibrils, and the infrared beam is focused into the crystal (Figure 18). The light travels inside the plate by means of a series of internal reflections from one surface of the plate to the other, creating an exponentially decaying evanescent radiation outside the plate, as shown in Figure 18. Absorption of the evanescent wave energy by the supported membrane and the reconstituted protein provides ATR-FTIR spectra. The decay length of the evanescent wave (here, ~ 0.6 µm) extends far beyond the dimensions of largest proteins. By using polarized light in ATR-FTIR measurements, the orientation of the protein with respect to membrane lipids can be obtained. The spectra of protein-lipid systems not only comprise of resolved bands of membrane lipids and proteins, they also differentiate between different functional groups of these molecules. For studying any processes regarding proteins/peptides, generally amide bond vibrations are recorded. Among those

bond vibrations, the amide-I band ($\sim$ 1700 – 1600 cm^{-1}) is most sensitive to different secondary conformations (*83, 84*).
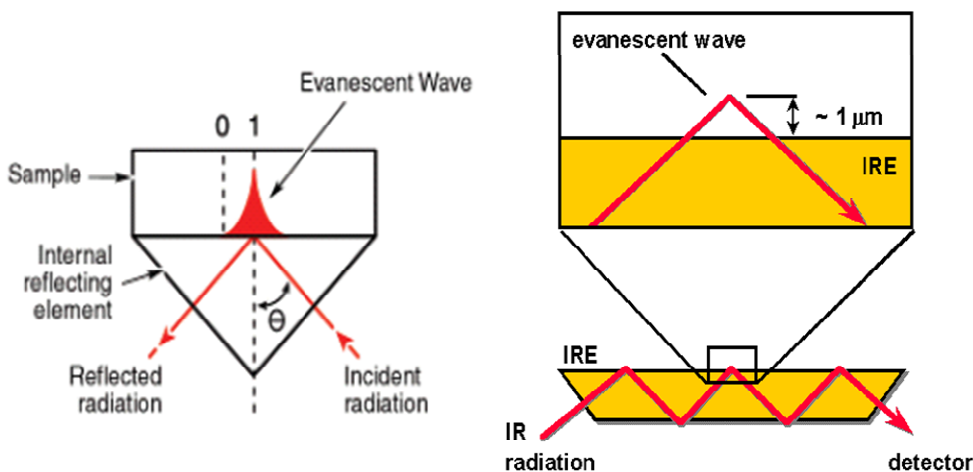

Figure 18: Left: schematic representation of a single reflection of infrared radiation and production of an evanescent wave. Right: schematic representation of total internal reflection and generation of an evanescent wave by internal reflecting elements (IRE).

2.2.10.4. Instrumentation and experimental part – ATR-FTIR

The ATR-FTIR spectroscopic measurements (*85*) were performed using a Nicolet 6700 FTIR-spectrometer equipped with a liquid nitrogen-cooled MCT-A detector. The spectrometer chamber was continuously purged with dry air to remove water vapor. The ATR out-of-compartment accessory consists of a liquid jacketed Piketech ATR flow-through cell made of steel. A trapezoidal Ge-Crystal (Piketech, Madison, WI, 80 mm x 10 mm x 4 mm, angle of incidence: 45°) was used as internal reflection unit (IRE). A background spectrum of air was collected using the same IRE before the sample measurements. Typically, spectra of 128 scans were taken with a resolution of 2 cm^{-1}. The measurements were usually performed at 25 °C. Processing of the ATR-FTIR spectra was performed using GRAMS-Ai 8.0 software (Thermo Electron). After subtraction of a spectrum of the lipid-membrane together with the buffer and subtraction of noise from water vapor, the spectra were baseline corrected between 1710 and 1585 cm^{-1} and also offset corrected. To follow the changes in secondary structure with time, the spectra were normalized by setting the area between 1710 and 1585 cm^{-1} of the amide-I' (amide-I bond

vibration in D_2O) band to 1, to compare differences in the adsorption propensities at the crystal and membrane surface, respectively.

For all infrared spectrometric experiments, a phosphate buffer (10 mM PO_4^{3-}, pD 7.4) in D_2O, containing 100 mM NaCl, was used. Stock solutions of the lipids were prepared by dissolving a mixture of 7 mg DOPC and 3 mg DOPG in chloroform up to a total lipid concentration of 10 mg/mL. 50 µL (containing 0.5 mg of lipids) of this solution were dried under a stream of nitrogen. When all chloroform was evaporated, the samples were placed in a Speed-Vac (SC110, Savant) for 3 h in order to remove residual chloroform.

Large unilamellar vesicles (LUV) and membranes

Stock solution of 0.5 mg of the lipid mixture (anionic: DOPC/DOPG 7:3, 8:2 or 9:1, lipid raft mixture: DOPC:DPPC:Chol 1:2:1, or pure DOPC) were prepared in chloroform:methanol (3:1) solution. Solvent was evaporated with the help of nitrogen gas, and then dried completely by lyophilisation overnight. The lyophilized lipid mixtures were re-dissolved in 1 mL of 10 mM phosphate buffer, pH 7.4, containing 0.1 mM NaCl, and ultrasonicated for 10 min. After 5 cycles of freezing and thawing, a homogeneous solution of multilamellar vesicles (MLVs) was obtained. To obtain a solution of large unilamellar vesicles (LUVs), the MLV solution was passed 11 times through an extruder with a membrane filter made of polycarbonate (Avanti, pore diameter: 0.1 µm). In case of the lipid raft mixture, the extrusion step was performed above its transition temperature, at 60 °C.

The freshly prepared solution of LUVs was injected carefully into the ATR-flow-cell, which was maintained at 25 °C (Figure 19). In case of the lipid raft mixture, the cell temperature was kept at 60 °C. Spreading of the vesicles took place spontaneously. After adsorption on the crystal overnight, the membrane was washed with buffer for a time period of 6 h (in case of the lipid raft mixture at 30 °C, the cell was kept at 25 °C before the peptide solution was added). For this purpose, 2 mL of buffer was pumped from a reservoir into the sample compartment (1.4 mL/min). Lipid vesicles, which did not strongly attached to the surface of ATR crystal, were washed away by the buffer solution.
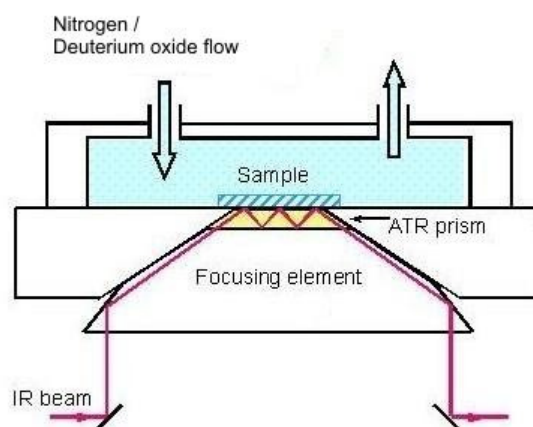
Figure 19: Schematic representation of the ATR-flow-cell along with the focusing element, IRE (ATR prism).

Adsorption and washing of the lipid membrane

The adsorption of the membrane was followed by monitoring the band intensity of the lipid-bands over time. For this purpose, a buffer spectrum was subtracted and spectra were baseline corrected in the region of the acyl-chains of the lipids between 3060 and 2820 cm^{-1}. Then, the area was determined by integration between 3030 and 2810 cm^{-1}. During the washing process, spectra were collected likewise performing the same steps. To check the membrane preparation and the reproducibility of the membrane deposition procedure, the area of the acyl-chain region was determined by integration between 3030 and 2810 cm^{-1} (average area: ~ 2.25 cm^{-1}). As shown in earlier studies, we may assume that after the washing step, one double layer of lipids is left on the IRE, only (*85*).

Adsorption of ProIAPP to the lipid membrane and aggregation

To ensure the integrity of the membrane, a proIAPP solution of 10 or 40 µM proIAPP was injected into the ATR-cell containing membrane by means of a peristaltic pump at 1.4 mL/min. Then the change of the amide-I' band was followed over time. Spectra were collected every 30 min over a time period of 7 d.

Analysis of the secondary structure changes of proIAPP

Second-derivative and Fourier self-deconvolution (FSD) were applied to the normalized spectra to identify the components in the amide-I' band region. These peaks

were then fitted to the normalized raw spectra according to the least squares condition, using a Levenberg-Marquardt curve fitting routine with bands of Voigt line shape. The starting width at half height of each peak was 8 cm^{-1}. Each peak position was restricted to move not farther than 1 - 3 cm^{-1} (as determined by the shifts in the second derivative and FSD) from their centres during the fitting routine. Such spectral shifts were allowed to take into account differences in the dielectric environment and conformational dynamics of the secondary structures. All spectra were fitted with a similar set of peaks and parameters. In ambiguous cases (such as the well-known overlap of the α-helical and unordered band regions), information from CD and NMR experiments were taken into account was well. The area under each peak represents the fraction of each component (assuming similar transition dipole moments for the different conformers) and was finally used to determine the percentage of secondary structure components (*86*).

Native structure of proIAPP

For the determination of the secondary structures of the native form of proIAPP, a 10 µM solution of peptides was injected into the ATR-flow-cell and after a few minutes, an ATR-FTIR-spectrum was collected.

Amide-I' band of fibrils grown by cross-seeding experiments

To check the secondary structure of the fibrils grown in the presence of seeds, 400 µL of the samples were taken and spread on the silicon crystal, and ATR-FTIR spectra were collected with time.

2.2.11. Atomic force microscopy (AFM)

Scanning probe microscope (SPM) is a branch of microscopy that provides information about the surface and its properties by scanning the specimen line by line using a physical probe (*87*). Atomic force microscopy (AFM) or scanning force microscopy (SFM) is a very high-resolution microscopy technique of the SPM family. A stylus, which raster-scan a surface with sufficient proximity or mechanical contact, is used in AFM to monitor the changes in the magnitude of the interaction between probe and specimen. Thereby, the resolution depends on the sharpness of the tip, the precision with which the

probe can be moved over the surface, and the sensitivity with which the interactions are detectable. AFM is not only capable of depicting surfaces with atomic resolution (*88*) or even subatomic resolution (*89*), but also of achieving a sub-molecular resolution in aqueous or gaseous medium (*90*). The working principle of the AFM is based on the deflection of an ultra sharp tip (stylus), which is mounted at the free end of a cantilever of 100 - 200 µm lengths that reflects a laser beam onto a photodiode. As the tip moves in response of the surface topography during scanning, the reflection of the laser beam changes, and the laser spot falling onto the photodiode moves in response, producing changes of intensity in each of its four segments. The photocurrent's differential signal between the top and the bottom segments contains the topographic information, whereas the orthogonal difference quantifies any lateral or twisting motion of the tip (*91*). By these means, frictional information can be distinguished from topographic information. In the simplest operating mode, the tip-sample distance is regulated by a feed-back in a way that the cantilever deflection (i.e. probed interaction) remains constant during a scan. The resulting control signal is recorded as a function of the lateral tip position, and converted into a false colour image, wherein the colour graduation reflects the extent of vertical displacement (*92*). The scheme shown in Figure 20 depicts the main part of AFM and working principle as described above.
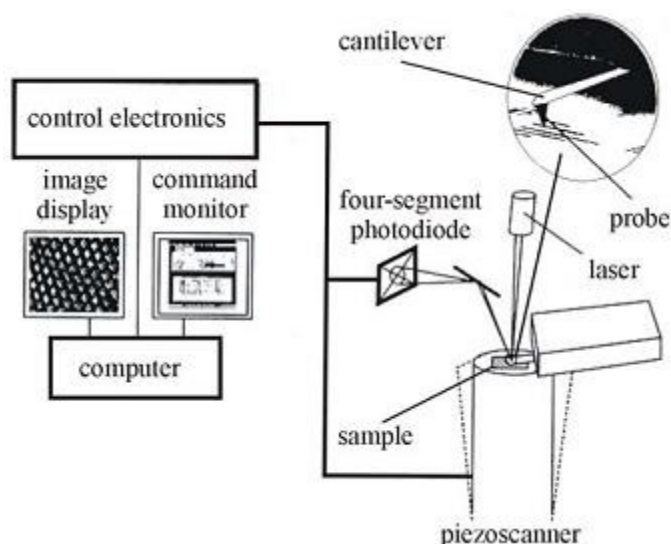

Figure 20: Scheme of the main components of an atomic force microscope. This device incorporates an electronic unit and a computer station equipped with image and command monitors. The microscope itself includes a piezoscanner, a probe and a laser beam deflection system (*93*).

Instrumentation and experimental part - AFM

The surface scans were recorded on a MultiMode scanning probe microscope equipped with a Nanoscope IIIa controller from Digital Instruments (Santa Barbara, California, USA). The microscope was coupled to an AS-12 E-scanner (~ 13 µm), and an Extender Electronics Module EX-II (Santa Barbara, California, USA), which allows the acquisition of phase images. Typically used AFM probes were aluminium coated NCMR silicon SPM sensors (force constant ~ 42 N/m; length ~ 125 µm; resonance frequency of 250 ±50 kHz; nominal top radius of curvature ≤ 5 nm) from Nanosensors, Budgetsensors. The AFM head with optical block and base was placed atop a commercially available active, piezo-actuated vibration damping desk from Halcyonics (Göttingen, Germany). All measurements were done in the air using TappingMode^{TM}.

TappingMode^{TM} AFM operates by scanning a tip attached to the end of an oscillating cantilever across the sample surface. The cantilever oscillated at or near its resonance frequency with amplitude ranging typically from 20 nm to 100 nm. The probe (stylus) lightly "taps" the sample surface during scanning, contacting the surface at the bottom of its swing. The feedback loop maintains constant oscillation amplitude by maintaining a constant root mean square of the oscillation signal acquired by the split photodiode detector. The vertical position of the scanner at each (x, y) data point, in order to maintain a constant "setpoint" amplitude, is sorted by the computer to form the topographic image of the sample surface. By maintaining the constant oscillation amplitude, a constant tip-sample interaction is also preserved during imaging. When imaging in air, the typical amplitude of the oscillation allows the tip to contact the surface through the adsorbed fluid layer without getting stuck (*91*).

For the morphology of fibrils grown at lipid bilayer interface, sample probes were taken from ATR-FTIR trough, and dissolved in chloroform to remove the lipids fraction from the probes. About 20 µL of sample were taken from the water soluble part and spin-coated on the freshly cleaved mica. Thereafter, it was freeze-dried in a lyophilizer prior to make any AFM scan of the samples. Samples from monolayer lipid samples were directly taken from the interface, coated on freshly cleaved mica and dried before doing any AFM scan. For the cross-seeding and SDS experiments, the diluted reaction mixtures were spin-coated on freshly cleaved mica and freeze-dried, prior to make any AFM scan.

Chapter 3. Results and discussion

3.1. The effect of membrane-mimicking surfactant, SDS on proIAPP fibrillation

Sodium dodecyl sulfate, SDS, is an anionic detergent, which has often been used as a membrane-mimicking agent (*94-96*). In phosphate buffer, pH 7.4, it exists either in a monomeric conformation or in a micellar conformation, depending on its concentration (*97*); at micromolar concentrations, SDS is known to interact with peptides and to induce order in the secondary conformation of the initially unordered peptides (*98, 99*). Because of its mesophasic behaviour, the different conformations adopted by SDS below, near, and above the critical micelle concentration, CMC (known to be 8 mM in water; addition of salts, in this case 10 mM phosphate, lowers the CMC (*97*)), could affect peptides differently (Figure 21).
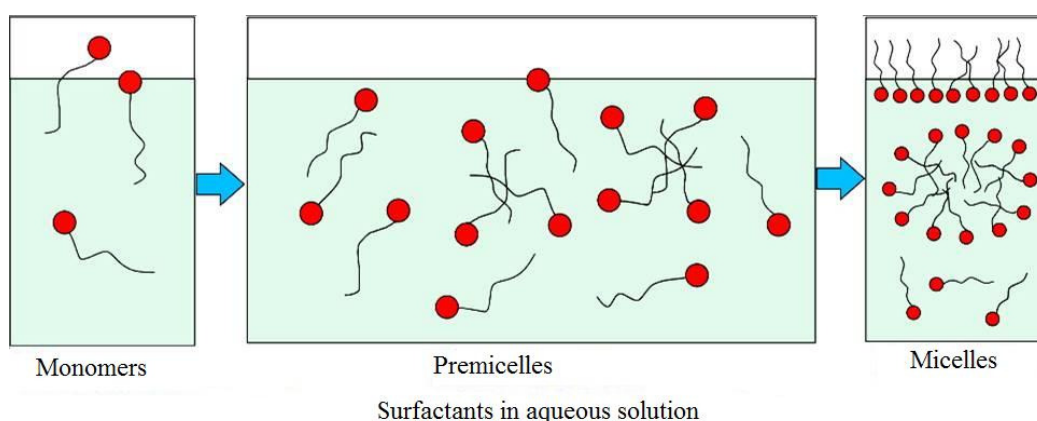

Figure 21: The diagram depicts the different conformations (mesophasic behaviour) attained at different concentrations of a surfactant in solution, i.e., monomers below the CMC, premicelles near the CMC, micelles above the CMC (adopted from Cui, et al. (*100*)).

To understand the membrane's effect on amyloidogenic peptides, with regards to their propensity to form amyloid fibrils inside the cells, they have been well-studied in the presence of SDS (*50, 101, 102*). In addition, the mesophasic nature and the simple chemistry of SDS molecules provides some vital information that can help in understanding the process in the process of more complex molecules or surfaces like non-esterified fatty acids or negatively charged phospholipid membranes, respectively (*101*). The effects of SDS on amyloid fibril formation vary, depending upon the concentration of SDS. SDS at sub-micellar concentrations has been shown to induce spherical aggregates (*50*), and is also

known to induce helical-rich conformation, which in turn may undergo conformational transitions to cross β-sheet conformations (*102*). The interactions of SDS with highly amyloidogenic peptides has been studied well above the CMC in order to provide structural insights of micelles bound to amyloidogenic peptide by NMR (*103*). However, to the best of our knowledge, there are no reports regarding the interactions of SDS or membranes except for this work or proceeding works done for this PhD thesis. The effects of various SDS concentrations, below or near the CMC, on the conformational transitions and the amyloidogenic propensity of proIAPP have been explored. To this end, combined methodological approaches, including fluorescence and circular dichroism spectroscopy, as well as tapping-mode atomic force microscopy have been used, as described in the subsequent sub-chapters.

3.1.1. Circular dichroism spectrometry study (conformational changes in proIAPP in the presence of SDS)

SDS is known to interact with proteins and peptides and to induce α-helical conformations (*98*). One of the most suitable techniques to follow changes in secondary structure is far-UV CD spectroscopy. CD spectra were recorded for 10 µM proIAPP in the presence of varying concentrations of SDS at the conditions described in the respective figure captions. To observe the effect of SDS on the conformational transition to amyloid fibrillar structures, different concentrations (0 µM, 100 µM, 0.5 mM, 1 mM) of SDS were used. The concentration of SDS at well-above the CMC is known to cease the amyloidogenic propensity of highly amyloidogenic peptides (*96*). Since the purpose was to study the effects of SDS on amyloidogenic propensity of proIAPP, SDS concentrations well-above the CMC were avoided for the study of proIAPP; proIAPP in bulk solution does not show any amyloidogenic character.

ProIAPP in the absence of SDS shows a CD peak minimum at 201 nm and a shoulder at ~ 225 nm, confirming random coil as a predominant monomeric starting structure (Figure 22). Moreover, the deconvolution results with the CDNN program reveal that proIAPP has a high population of disordered secondary structure element, approximately 40% random coil and 30% turns, as shown in the inset of Figure 22. Additionally, there has neither been any significant decrease in the ellipticity at 201 nm, nor any peak change from 201 nm to

216 nm, when recording CD spectra over 143 h under the experimental conditions used. Thus, proIAPP does not show any amyloidogenic propensity to aggregate or fibrillate in the absence of SDS, as observed by these time dependent CD spectroscopic measurements.
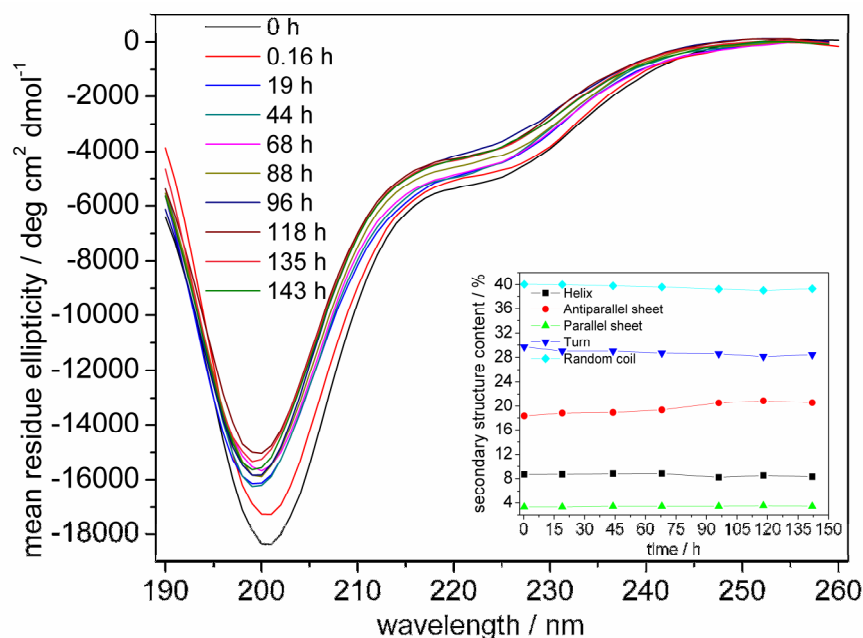

Figure 22: Ellipticity spectra as monitored by CD spectroscopy for 10 µM proIAPP in 10 mM phosphate buffer, pH 7.4, at 25 °C. The inset shows the change in secondary structure content, deconvoluted using the CDNN program for the wavelength range 195 - 260 nm.

In the presence of 100 µM SDS, there is a small but significant induction of ordered secondary structures in the initially unordered conformation as observed in the CD spectra measured over five days (Figure 23). The negative ellipticity peak that is present at ~ 201 nm in the absence of SDS shifts to ~ 205 nm in the presence of 100 µM SDS, whereas the ellipticity at ~ 222 nm is more prominent than without SDS. The CDNN deconvolution of temporal CD spectra proves that SDS at this concentration induces ordered secondary structures to some extent (~ 8%), as it is generally known for. This partially folded conformation seems to undergo precipitation, as concluded from the decrease in the ellipticity at 205 nm with time. However, proIAPP in the presence of 100 µM SDS did not show any conformational transition in the ellipticity peak to 216 nm, the signature peak transition in the case of amyloid fibril formation, but the deconvolution using the CDNN program shows a small change in conformation from random coil to antiparallel β-sheet

(inset of Figure 23), indicating the accumulation of some conformations that are rich in antiparallel β-sheet conformations.
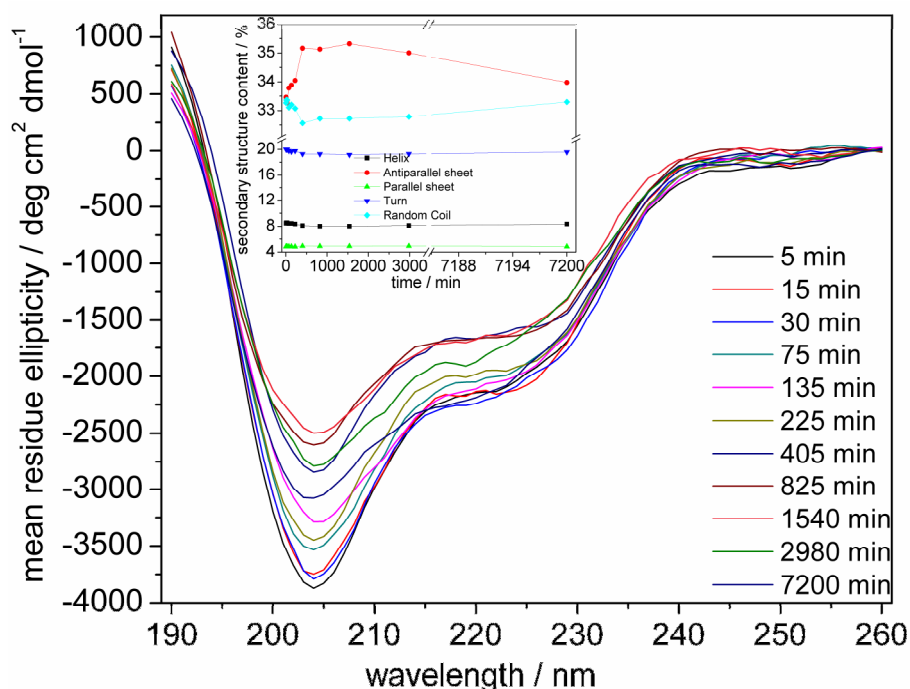

Figure 23: Ellipticity spectra as monitored by CD spectroscopy for 10 µM proIAPP in the presence of 10 mM phosphate buffer, pH 7.4, containing 100 µM SDS at 25 °C. The inset shows the change in secondary structure content, deconvoluted using CDNN for the wavelength range 195 - 260 nm.

Upon further increase in SDS concentration to 0.5 mM, an ellipticity peak at 208 nm appeared along with another peak at ~ 222 nm that are typical signatures for α-helical conformations (Figure 24). This shows that proIAPP attained a predominantly α-helical conformation at 0.5 mM SDS concentration, whereby 100 µM SDS was unable to induce α-helical structures in the initially unordered conformation. Similar to the proIAPP fibrillation reaction containing 100 µM SDS, the solubility of monomeric proIAPP molecules decreased within the first 17 h of incubation in the presence of 0.5 mM SDS, as observed by the decrease in the ellipticity of the CD spectra recorded. This decrease occurs also without a subsequent transition of the ellipticity peak. However, the deconvolution of the time dependent CD spectra shows that this decrease in the ellipticity is accompanied by a loss in α-helical conformation and subsequent gain in corresponding antiparallel β-sheet structures (inset of Figure 24).
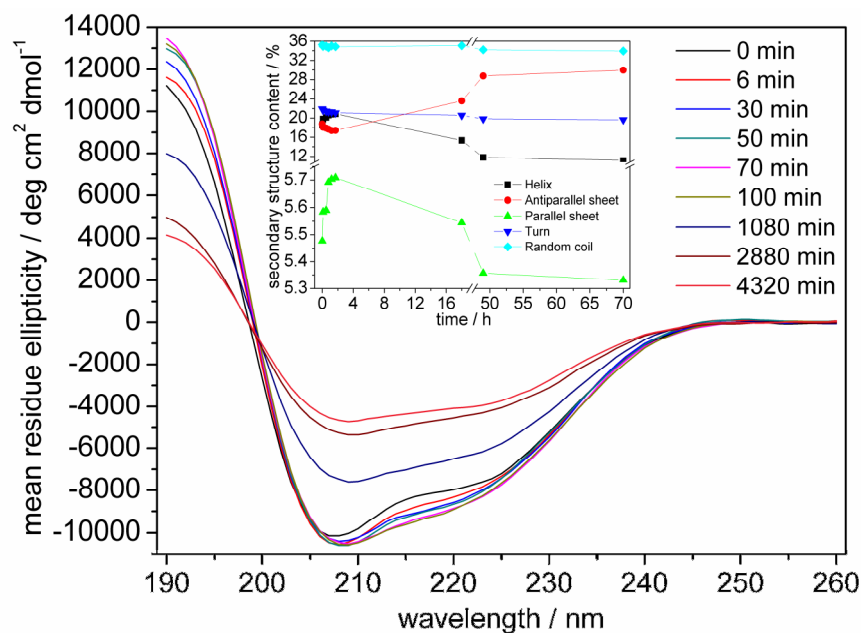
Figure 24: Ellipticity spectra as monitored by CD spectroscopy for 10 µM proIAPP in the presence of 10 mM phosphate buffer, pH 7.4, containing 0.5 mM SDS at 25 °C. The inset shows the changes in secondary structure content, deconvoluted using CDNN for the wavelength range 195 - 260 nm.

Further increase in SDS concentrations to 1 mM SDS leads to a more prominent contribution of α-helical structures that are resistant to precipitation into insoluble structures, as shown in Figure 25. The ellipticity of proIAPP in 1 mM SDS neither decreases nor undergoes a transition to 216 nm with time. Furthermore, the deconvolution using the CDNN program is also unable to reveal any inter-conversion of secondary structure elements (inset in Figure 25). Hence, at this SDS concentration, a relatively large population of proIAPP molecules attains α-helical conformations on interaction with SDS micellar conformation.
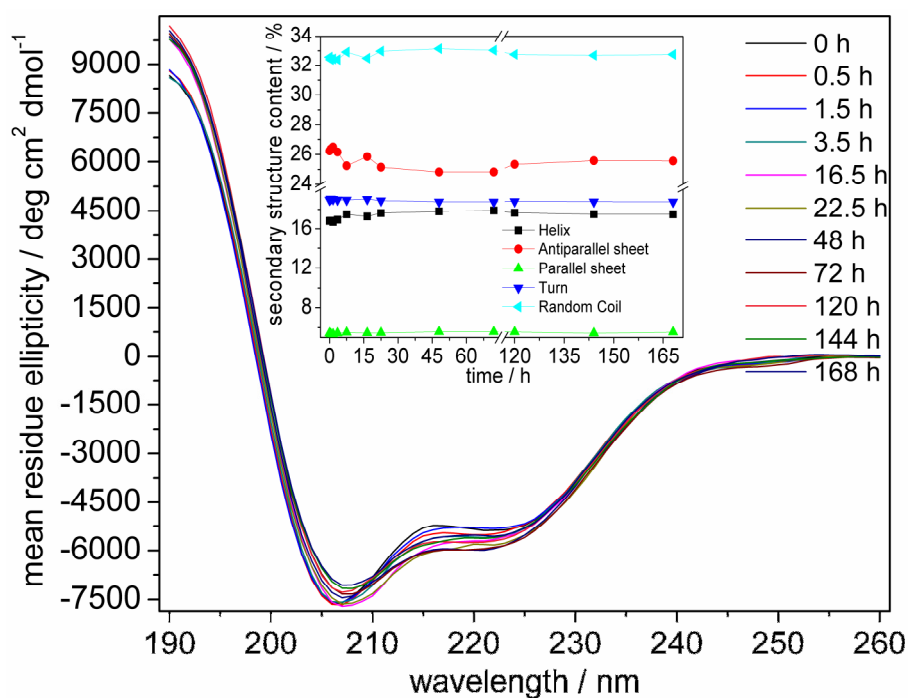
Figure 25: Ellipticity spectra as monitored by CD spectroscopy for 10 µM proIAPP in the presence of 10 mM phosphate buffer, pH 7.4, containing 1 mM SDS at 25 °C. The inset shows the change in secondary structure content, obtained by deconvolution using the CDNN program for the wavelength range 195 - 260 nm.

Thus, proIAPP does not undergo any prominent conformational transition under these conditions, a decrease in ellipticity is observed in the CD spectra at 0.1 mM SDS and 0.5 mM SDS, only.

3.1.2. Thioflavin T binding assay

As described in the section for materials and methods, Thioflavin T (ThT) is an amyloid specific dye, which upon binding to amyloid fibrils exhibits a typical excitation maximum at ~ 440 nm and an emission maximum at ~ 482 nm (*70*). Additionally, the fibril formation occurs simultaneously with ThT binding; this characteristic of ThT is used to follow the kinetics of fibril formation by following the emission intensity at 482 nm by fluorescence spectroscopy. Generally, fibril formation is accompanied by a slow nucleation rate, followed by a fast elongation phase and finally a stationary phase. These three phases, when put together, represent the sigmoidal kinetics observed for ThT binding to fibrils (*57*).

The ThT emission intensity at 482 nm is constant with time (up to 170 h) for 10 µM proIAPP for the condition mentioned in the figure legend of Figure 26. A varying SDS

concentration in the reaction buffer leads to a distinguished change in ThT emission intensity at 482 nm, i.e., the amyloidogenic propensity of proIAPP. However, this change in ThT intensity is observed only for a very small range of SDS concentrations in the reaction buffer.
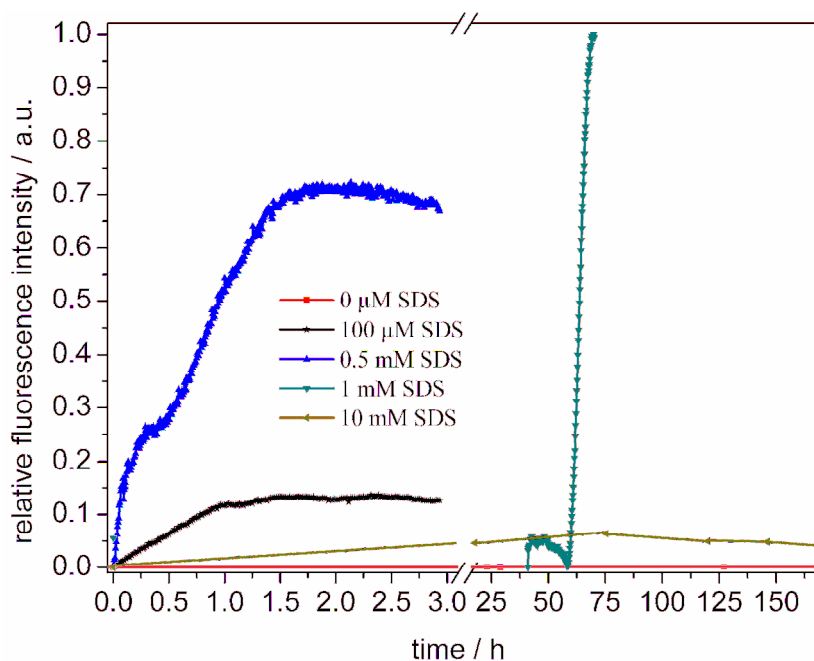

Figure 26: Kinetics of 10 µM proIAPP amyloid fibril formation carried out in 10 mM phosphate buffer containing 10 µM ThT, pH 7.4, at 25 °C, in the presence of 0 µM SDS (solid red cube), 100 µM SDS (solid black star), 0.5 mM SDS (solid blue triangle), 1 mM SDS (inverse dark cyan triangle) and 10 mM SDS (solid dark yellow tilted triangle).

Starting with a tenfold higher molar ratio of SDS:proIAPP, proIAPP shows a slight increase in ThT emission intensity at 482 nm. This increase was not accompanied by any lag phase and the intensity of the stationary phase was only ca. 12% of the highest intensity observed for the same concentration of proIAPP in the presence of 1 mM SDS (Figure 26). At a fiftyfold higher molar ratio, i.e. 0.5 mM SDS in 10 µM proIAPP, a kinetic profile with a distinguished exponential growth phase and without lag phase was recorded (Figure 26). ProIAPP reaches the stationary phase within 2 h. However, the emission intensity is approximately 70% of the highest intensity observed in the presence of 1 mM SDS, only. Thus, the fibril formation observed in the presence of 100 µM and 0.5 mM SDS does not accompany any nucleation phase (Figure 26). Moreover, at a hundredfold higher molar ratio, i.e. 1 mM SDS in 10 µM proIAPP, a long lag phase of 58 h is observed, followed by

a well-defined exponential growth phase. A further increase in SDS concentration to 10 mM does not show any effect on the fibrillation of 10 µM proIAPP within the time frame of the experiment (170 h of monitoring the ThT fluorescence kinetics) as shown in Figure 26. Hence, proIAPP shows a maximum amyloidogenic propensity in the presence of 0.5 mM SDS, with relatively rapid fibrillation kinetics. However, in terms of final ThT emission intensity at 482 nm, 1 mM SDS is more efficient in transforming proIAPP molecules into amyloid fibril structures.

3.1.3. AFM study

Atomic force microscope (AFM), as described in the materials and methods section, is used for the characterization of surface morphology. Samples were taken from the respective reaction mixtures where the ThT kinetics reached the stationary phase. Thereafter, the spin-coating method was used to prepare the sample for the AFM scan, followed by freeze-drying, which guarantees a minimum time to dry, thus minimize surface-induced aggregation effects. The morphologies of the spin-coated samples on the mica surfaces are consistent with the corresponding fibrillation kinetics. 10 µM proIAPP do not show any oligomeric/protofibrillar/fibrillar morphology in the AFM scan in the absence of SDS and in the presence of 10 mM SDS. Samples from the 0.1 mM SDS reaction solution display oligomeric conformations with heights of 2 - 3 nm (Figure 27, left).
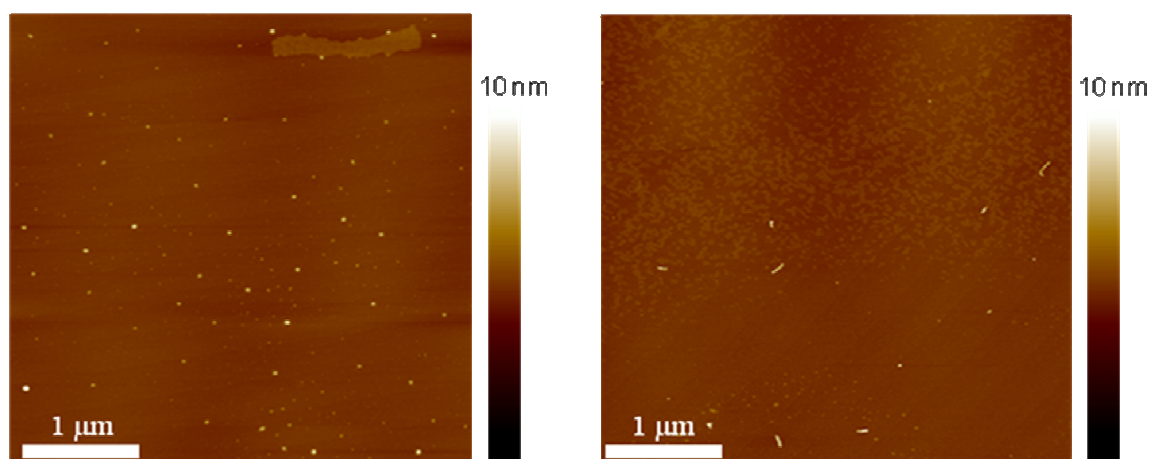

Figure 27: AFM images of proIAPP amyloid fibrils formed in the presence of 100 µM SDS (left) and 0.5 mM SDS (right).

AFM samples prepared from the stationary phase of proIAPP fibrillation containing 0.5 mM SDS show short and twisted protofibrils with a height of 3 - 4 nm, only (Figure 27, right). Although samples from the stationary phase of the proIAPP fibrillation kinetics in the presence of 1 mM SDS show typical long fibrils with a height of 3 - 4 nm in the AFM (Figure 28), no fibrillar morphology was observed for the samples prepared from proIAPP fibrillation reaction mixture containing 10 mM SDS.
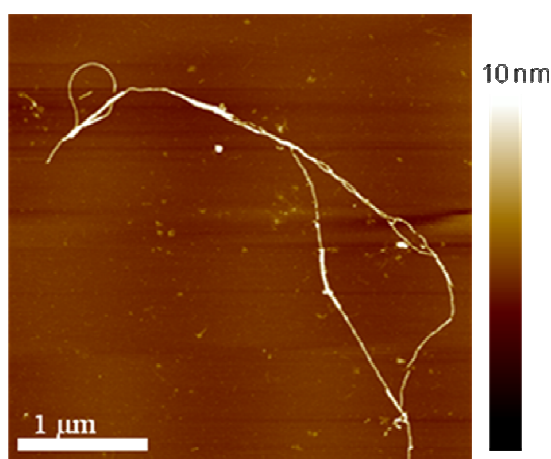

Figure 28: AFM image of proIAPP amyloid fibrils formed in the presence of 1 mM SDS.

3.1.4. Discussion (SDS effects on proIAPP fibril formation)

ProIAPP is known to be the least amyloidogenic polypeptide among the processing intermediate polypeptides during IAPP synthesis in pancreatic β-cells (*17*). The least amyloidogenic propensity of proIAPP has been explained by the presence of positively charged N- and C- termini, directly flanking the primary sequence of the highly amyloidogenic polypeptide IAPP (*17, 18*). Moreover, the N-terminal extended proIAPP fragment has been shown to interact with negatively charged surfaces present inside the pancreatic β-cells (*21*). Thus, the hypothesis has been put forward that proIAPP might be involving in the onset of T2DM through intracellular amyloid fibril formation via interaction with these negatively charged cellular moieties (*21*). However, the factors that govern the formation of this intracellular amyloid are still unclear. Since very little is known about the amyloidogenic propensity of proIAPP, because of its non-amyloidogenic nature *in vitro*, it was advisable to select a simple negatively charged surface to study the possible underlying mechanism of intracellular amyloid fibril formation of proIAPP. On the

57

other hand, sodium dodecyl sulfate (SDS) has been well established as a membrane-mimicking agent to reveal the influence of simple negatively charged membranes on amyloidogenic peptides (*94, 95*). SDS attains different conformations in the reaction buffer, depending upon the concentration of SDS, i.e. below and above the critical micelle concentration (CMC). Thus, the different concentrations of SDS have shown different effects on the fibrillation kinetics of proIAPP as well as on the fibrillar morphology of proIAPP. Here, proIAPP does not show any amyloidogenic propensity in the absence of SDS for the measured period of time and conditions, i.e., no conformational transition or significant decrease in ellipticity by CD (Figure 22), neither an increase in ThT emission intensity at 482 nm (Figure 27), nor any oligomeric/protofibrillar/fibrillar morphologies by AFM have been observed. Freshly dissolved proIAPP exhibits predominantly a random coil conformation. However, addition of SDS to the reaction buffer induces ordered secondary structures as well as amyloidogenic propensity in proIAPP. The range of SDS concentrations that could induce the amyloidogenic propensity in proIAPP was found to be narrow under the experimental conditions chosen, i.e., 0.1 – 1.0 mM only, while the concentration which was able to induce an α-helical conformation in proIAPP was 0.5 mM SDS or above. Moreover, no conformational transition was detected by CD spectroscopy. In the cases of aggregation, only a significant decrease in ellipticity was observed (Figure 23-25). Additionally, proIAPP in the presence of 0.5 mM SDS was able to show some conformational transition from α-helix to β-sheet after deconvolution, only (inset of Figure 24).

SDS at a 100 μM concentration was the first one to induce an amyloidogenic propensity in proIAPP, however, to some extent, only. At 0.5 mM, SDS was able to induce a marked amyloidogenic propensity in proIAPP, as observed in the ThT binding kinetics (Figure 26). This observation can be rationalized by the presence of positively charged residues at the N- and C- termini of the highly amyloidogenic motif of proIAPP. To screen the electrostatic repulsion between these positively charged residues, an optimum concentration of SDS was needed. At 0.5 mM SDS, proIAPP showed a typical fibrillation kinetics, accompanied by a well distinguished exponential phase but without any lag phase. ProIAPP fibrils only attain oligomeric and protofibrillar conformations in the presence of 0.1 and 0.5 mM SDS, respectively. These findings may have special significance *in vivo*,

possibly seeding the IAPP and insulin fibrillation (Chapter 3.4). Moreover, a 1 mM SDS concentration was able to induce amyloidogenic propensity in proIAPP, as observed by a well pronounced ThT kinetics with a relatively long lag phase followed by an exponential growth phase (Figure 26), and a matured fibrillar morphology with fibrillar heights of 3 - 4 nm (Figure 28). This indicates that the gradual appearance of micelles around the CMC (the CMC for SDS in water is 8 mM, adding salts decreases the CMC) imposes a certain steric hindrance in the self-assembly of peptide molecules into oligomers, thus a long lag phase was observed in the presence of 1 mM SDS. However, once the nuclei/oligomers were established, the highest increase in fluorescence emission intensity at 482 nm was observed. 10 mM SDS (above the CMC) was unable to induce amyloidogenic propensity in proIAPP, either because of the absence of monomeric conformations of SDS to screen the electrostatic repulsion between residues of adjacent peptide molecules or the interaction between SDS micelles and proIAPP is imposing a certain steric hindrance, thus prolonging the time scale of nuclei/oligomers formation beyond the time frame of our study at this concentration.

Thus, these results show that SDS affects the conformation and the amyloidogenic propensity of proIAPP. Below the CMC, SDS enhances the proIAPP fibrillation mainly by screening the electrostatic repulsion, while near the CMC the appearance of micellar structures of SDS decreases the rate of nucleus formation by partitioning of the monomeric proIAPP population inside micelles. Micelles, upon binding to proIAPP, are able to induce an α-helical conformation in the proIAPP. SDS above the CMC is able to diminish the amyloidogenic propensity of proIAPP by binding to the peptide molecules, thus inhibiting the proximity of another peptide molecule via steric hindrance, hence inhibit the self assembly of proIAPP into amyloid fibrillar structures.

3.2. The effect of lipid monolayers on proIAPP fibrillation

After establishing the amyloidogenic propensity of proIAPP in the presence of negatively charged surfactant (SDS), our focus shifted towards the study of the conformational changes in proIAPP upon interaction with model lipid monolayer membranes. The physiologically active part of proIAPP, IAPP has been shown to insert itself as monomers into the lipid monolayer membranes with the help of the charged

residues present at the N-terminus of the peptide (*23*). This insertion of monomeric IAPP molecules enhanced the rate of IAPP amyloid fibril formation (*22*). Since proIAPP has a relatively higher number of positively charged residues at the N-terminus, the possibility of comparatively strong electrostatic interaction between proIAPP and negatively charged monolayer membranes might play an important role in the amyloid fibril formation of otherwise non-amyloidogenic proIAPP. To address this point, we tried to study the conformational dynamics of proIAPP and its mutant, proIAPP$_{Ser13, 18}$, upon interaction with negatively charged lipid monolayers (POPG) at different initial surface pressures, i.e., 16 mN/m, 20.5 mN/m (for mutant proIAPP, only) and 31 mN/m, respectively, by employing methodologies like IRRAS and AFM.

3.2.1. IRRAS study

As mentioned in the materials and methods section, IRRAS is the most suitable technique for the study of lipid-peptide interactions by analysis of the contours of the amide-I and -II bands. Here, proIAPP and mutant proIAPP (proIAPP$_{Ser13,18}$) interactions with a negatively charged lipid monolayer, POPG, were studied. First, we studied the interaction of 1 µM proIAPP with negatively charged lipid monolayers of POPG at a surface pressure of 16 mN/m. As shown in the inset of Figure 29, the increase in surface pressure was observed immediately after addition of the POPG solution onto the subphase containing 1 µM proIAPP. This increase in surface pressure was accompanied by two phases, one exponentially increasing phase, reaching a surface pressure of ~ 21 mN/m within first hour of the injection of POPG, and another very slow, non-stop increasing phase, with the surface pressure reaching ~ 24.5 mN/m in the next ~ 22 h of measurement (inset of Figure 29).
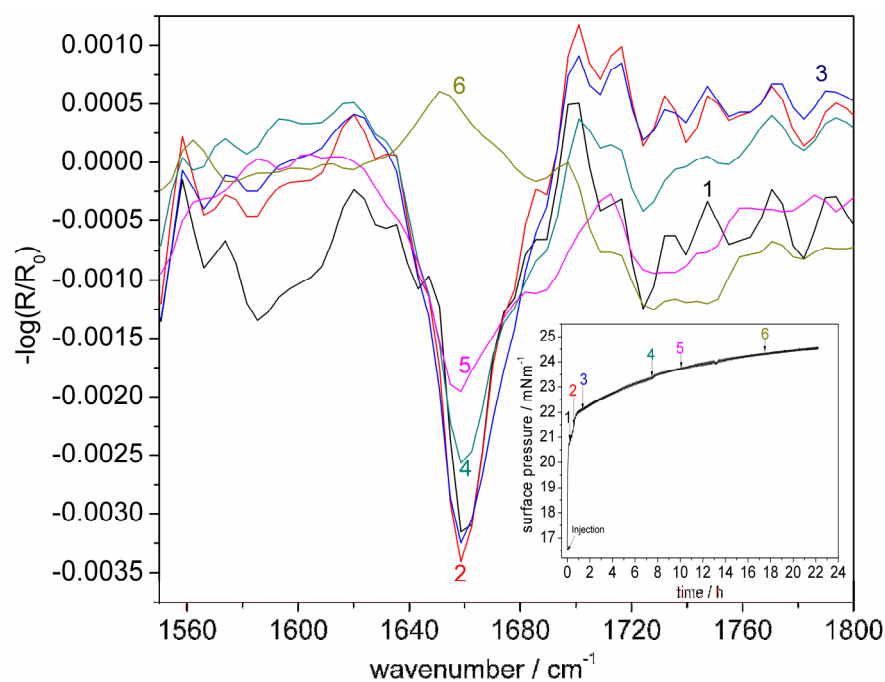
Figure 29: IRRA spectra of the amide-I' regions of POPG monolayers with 1 µM proIAPP at the respective positions of the surface-pressure versus time curve shown in the inset, with an initial surface pressure of ~ 16 mN/m.

The wavenumbers of the amide-I' band with initial values of ~ 1658 cm^{-1}, typical for α-helical conformations, remained constant with a slight increase in the intensity, during the exponential increase in surface pressure. However, the slowly increasing surface pressure curve was accompanied by a decrease in the intensity of the amide-I' band at ~ 1658 cm^{-1}. The IRRA spectra measured after ~18 h of the lipid injection onto the subphase show an amide-I' band of positive intensity with a shift of 8 cm^{-1}, i.e., at ~ 1650 cm^{-1} (Figure 29).

The packing density of lipids in biological bilayer membranes corresponds to a surface-pressure of ~ 30 - 35 mN/m (*104*). Thus, in order to check the ability of proIAPP to insert into bilayer membranes, the conformational dynamics and adsorption isotherm were measured at an initial surface-pressure of 31 mN/m. At this surface pressure, two positive peaks in the amide-I' band region, corresponding to 1646 and 1685 cm^{-1}, appeared (Figure 30). However, there was a significant increase (~ 10 mN/m) in the surface pressure upon injection of POPG solution onto the subphase containing 1 µM proIAPP (inset of Figure 30). The 10 mN/m increase of surface pressure strongly suggests that proIAPP is able to insert into the POPG membrane, as has been shown with the physiologically active peptide IAPP, which inserts into biological membranes *in vivo* (*22*).
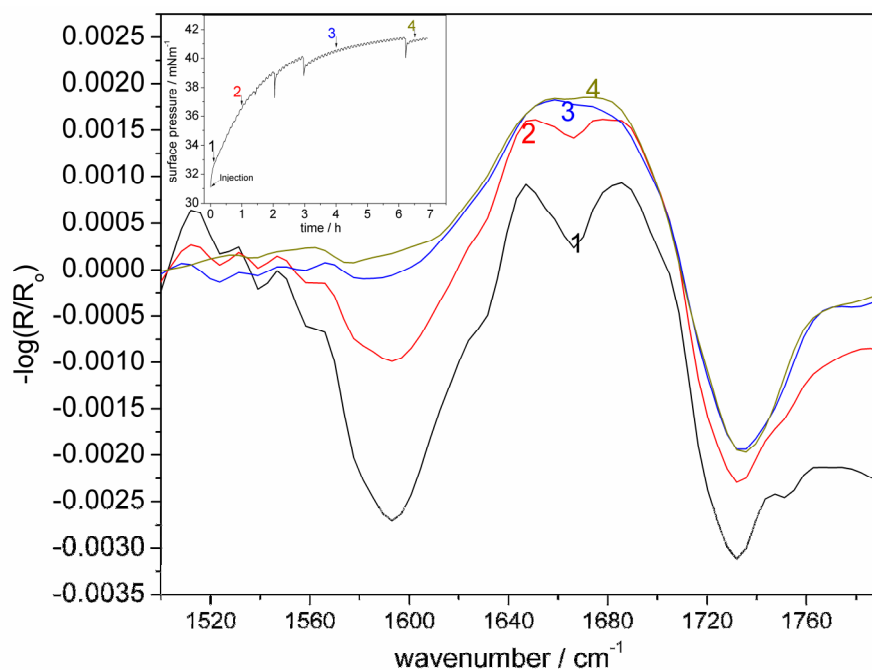
Figure 30: IRRA spectra of the amide-I' region of POPG monolayers with 1 µM proIAPP at the respective positions of the surface-pressure versus time curve shown in the inset, with an initial surface pressure of ~ 31 mN/m.

At this initial surface pressure of 30 mN/m, proIAPP consist of a major population of random coil conformation with some percentage of turns with bands at ~ 1647 and 1685 cm^{-1} (Figure 30). These two IR peaks merged into one broad peak with center at ~ 1666 cm^{-1}, with time and increasing surface pressure.

The interaction of mutant proIAPP, proIAPP$_{Ser13, 18}$, interaction with lipid monolayers was also studied. Interestingly, the replacement of Cysteine 13 and 18 of proIAPP with serine had an impact on the insertion kinetics of proIAPP. At the initial surface pressure of ~ 20 mN/m, proIAPP$_{Ser13,18}$ adsorbs immediately at the POPG-D$_2$O interface, as concluded from the exponential increase in the surface pressure immediately after the addition of POPG solution onto the subphase containing 1.66 µM proIAPP (inset of Figure 31). However, the increase in surface pressure was not so prominent for proIAPP adsorption at an initial surface pressure of 16 and 31 mN/m. ProIAPP$_{Ser13, 18}$ attains a conformation rich in α-helix content, upon adsorption to the lipid-D$_2$O interface (Figure 31). After 3 h of injection of the POPG solution onto the subphase, the surface pressure reached 25.5 mN/m but the conformation of the mutant proIAPP (proIAPP$_{Ser13, 18}$) remained constant without

any conformational transition or decrease in intensity of the amide-I' band (Figure 31); however, proIAPP at 25 mN/m had already diffused to the reference trough, which resulted in net positive amide-I' band (Figure 29).
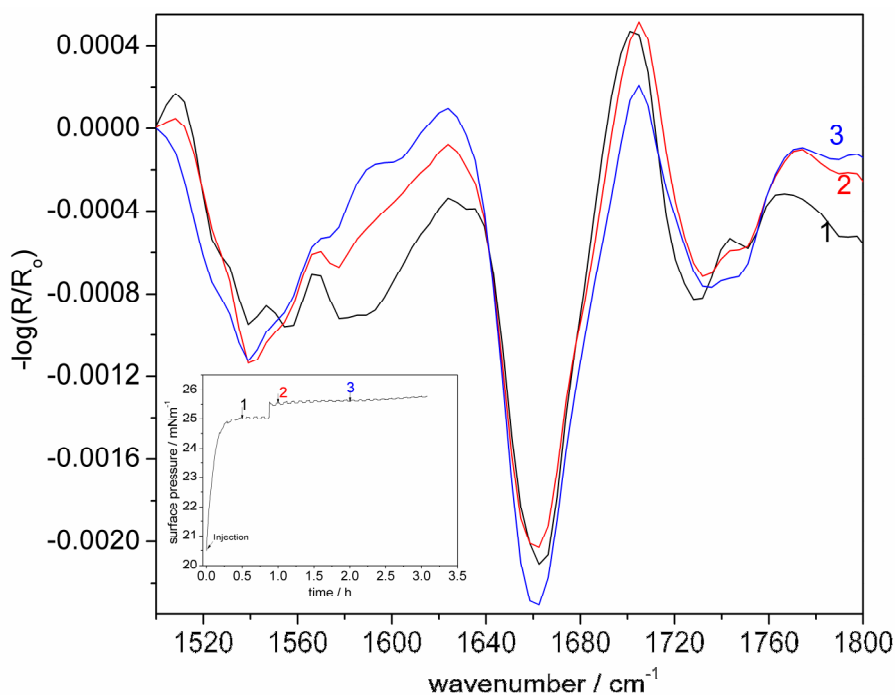

Figure 31: IRRA spectra of the amide-I' region of POPG monolayers with 1.66 µM proIAPP$_{Ser13, 18}$, at the respective positions of the surface-pressure versus time curve shown in the inset, with an initial surface pressure of ~ 20 mN/m.

3.2.2. AFM study

Atomic force microscope (AFM) has been used here to characterize the morphology of the surface containing samples from the sample trough as well as the reference trough of the IRRAS experiments. 5 µL of the samples from the interface of lipid-D_2O of the sample trough and air-D_2O of the reference trough were applied onto freshly cleaved muscovite mica and allowed to dry at ambient temperature. Fibrillar morphologies with a height of 3 - 5 nm were found in both samples of 1 µM proIAPP at initial surface pressures of ~ 16 mN/m and 31 mN/m, respectively (Figure 32). However, the proIAPP$_{Ser13, 18}$ samples collected from the air-D_2O and POPG lipid monolayer-D_2O interface of the sample and reference trough, respectively, did not show any fibrillar-like morphology. Interestingly, the fibrils formed at an initial surface pressure of 31 mN/m were densely grown in comparison to the fibrils formed at an initial surface pressure of 16 mN/m (Figure 32).
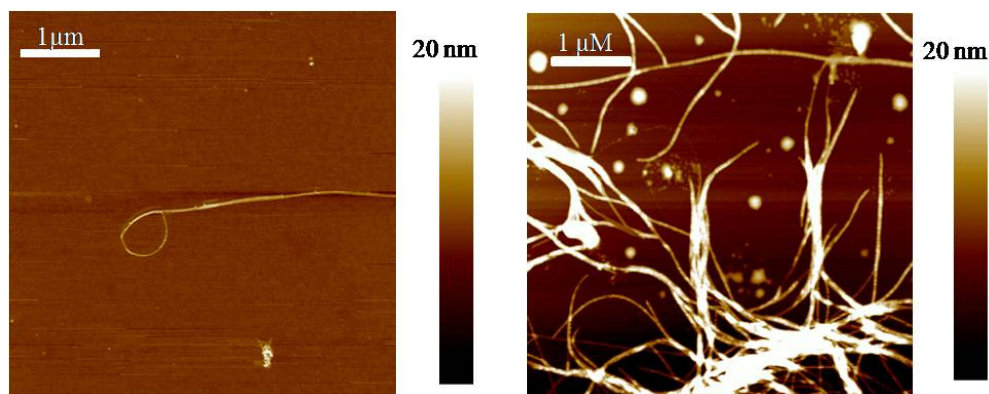
Figure 32: Representative AFM image of proIAPP (1 µM) amyloid fibrils, formed at the POPG-D$_2$O interface (sample trough) and air-D$_2$O interface (reference trough) at a surface pressure of 16 mN/m (left panel) and 31 mN/m (right panel), respectively.

3.2.3. Discussion

In this study, the IRRAS methodology was used to explore the effect of lipid monolayers on the conformational properties and amyloidogenic propensity of proIAPP at, below and near the intracellular membrane's lateral pressure. ProIAPP shows a similar adsorption isotherm as shown by its physiologically active part, IAPP, upon interaction with negatively charged lipid monolayers (*22*). The increase in lateral pressure is not that prominent, but it is significant (> 8 mN/m), independent of the initial lateral pressure of the lipid monolayers (16 and 31 mN/m, respectively), indicating that proIAPP is inserting into the lipid monolayers. The insertion of proIAPP into the POPG monolayers is not accompanied by any conformational transition, in contrast to what has been observed for IAPP upon insertion into lipid monolayers (*22*). Interestingly, the absorbance of the amide-I' band decreases with time, which could have the following reasons:

1) The peptide undergoes a conformational transition, i.e., from α-helix (1658 cm^{-1}) to another conformation.

2) The peptide undergoes an orientational change during its aggregation at the lipid-D$_2$O interface.

3) The peptide diffuses spontaneously to the reference trough.

Since time dependent IRRA spectra did not show any conformational transition, the first possibility can be ruled out. Additionally, the IRRA spectra which were measured with 40° p-polarized light indicate that the second possibility of an orientational change can also

be excluded as potential reason for the decrease in absorbance of the amide-I' band. Hence, the third possibility remains the only reason to describe the decrease in absorbance of the amide-I' band with time. The phenomenon of spontaneous diffusion was later confirmed by the AFM images; AFM images of samples from interfaces of the sample and reference trough show fibrillar morphology, indicating diffusion of peptides to the reference trough took place. Moreover, peptides have been shown to diffuse spontaneously to the reference trough despite insertion into the lipid monolayer (*22*).

The IRRA spectra presented originate from the difference between the absorbance of p-polarized infrared light by the surface of the reference and sample trough, respectively. Thus, if any conformational changes occur in the sample trough due to fibril formation at the lipid interface, it may have been subtracted to null by the conformational changes happening in peptides that diffused to the reference trough. Moreover, at a 31 mN/m initial lateral pressure of the lipid monolayers, the IRRA spectra were showing a positive amide-I' band absorbance from the very beginning, indicating that the major population of proIAPP has already diffused to the reference trough. This reflects the fact that a certain surface pressure value is needed for spontaneous diffusion of proIAPP to the reference trough.

Based on these observations, we can conclude that:

1) ProIAPP inserts into negatively charged lipid monolayers.

2) The insertion induces an α-helical conformation in proIAPP.

3) After a certain time or/and a certain surface pressure, the major population of the proIAPP molecules diffuses to the reference trough, and only a small fraction of the peptide molecules interacts/inserts into the lipid monolayers, as shown by the slow increase of the surface pressure in the late phase of the adsorption isotherm.

To conclude, the insertion of proIAPP into lipid monolayers induces the folding of proIAPP to an α-helix rich conformation, which undergoes amyloid fibril formation. Furthermore, the diffusion of aggregated amyloid fibrils from the subphase/interface of the sample trough to the reference trough most likely accounts for the observed positive amide-I' band. Interestingly, SDS at micellar concentrations induced a similar effect in proIAPP, i.e., a conformational switch from random coil to α-helix. Thus, it can be concluded that

proIAPP attains an α-helical rich conformation upon binding/insertion into negatively charged lipid-like (SDS)/lipid (POPG) interfaces, before it finally starts to fibrillate.

3.3. The effect of lipid bilayer membranes on proIAPP fibrillation

The prediabetic stage of T2DM is accompanied by higher insulin needs, which in turn triggers the release of premature secretory granules through secretagogue stimulation, containing a higher amount of unprocessed prohormones (proIAPP and proinsulin). Furthermore, increased levels of free fatty acids have been observed in the prediabetic stage of T2DM (*20*). It has been shown that the β-cells exposed to hyperlipidaemia remodulate their membranes by increasing the negatively charged lipid content (*105-107*). In the prediabetic stage, the anionic lipid content of the membrane seems to increase beyond the physiological range, i.e. > 10 - 30%. In fact, it has been shown that the processing intermediates of proIAPP bind strongly to the membranes that have more than 30% anionic lipids, and this binding increases the amyloid fibrillation rate significantly (*51*). Thus, the purpose of this part of the thesis was to:

1) explore the amyloidogenic propensity and conformational properties of human proIAPP in the presence of negatively charged membrane surfaces, which are abundant in cellular environments of the prediabetic stage.

2) reveal the mechanism of proIAPP aggregation/fibrillation reaction in the absence and presence of these anionic and various other membrane systems, including heterogeneous model raft mixtures.

The effect of proIAPP on IAPP fibrillation in the presence of lipid membranes has been investigated. To this end, a combined spectroscopy and microscopy approach has been applied using CD, fluorescence and ATR-FTIR spectroscopy as well as AFM.

3.3.1. CD and ATR-FTIR spectroscopy study

The starting conformation of proIAPP was investigated by dissolving 10 µM proIAPP in phosphate buffer via CD or FTIR spectroscopy, respectively. The CD spectra exhibit a minimum at ~ 201 nm along with a shoulder at ~ 220 nm (Figure 33), indicating that proIAPP has a predominantly random coil conformation (~ 37%, as found by the CDNN

fitting program, inset of Figure 33) along with some regular secondary structure elements as the starting conformation.
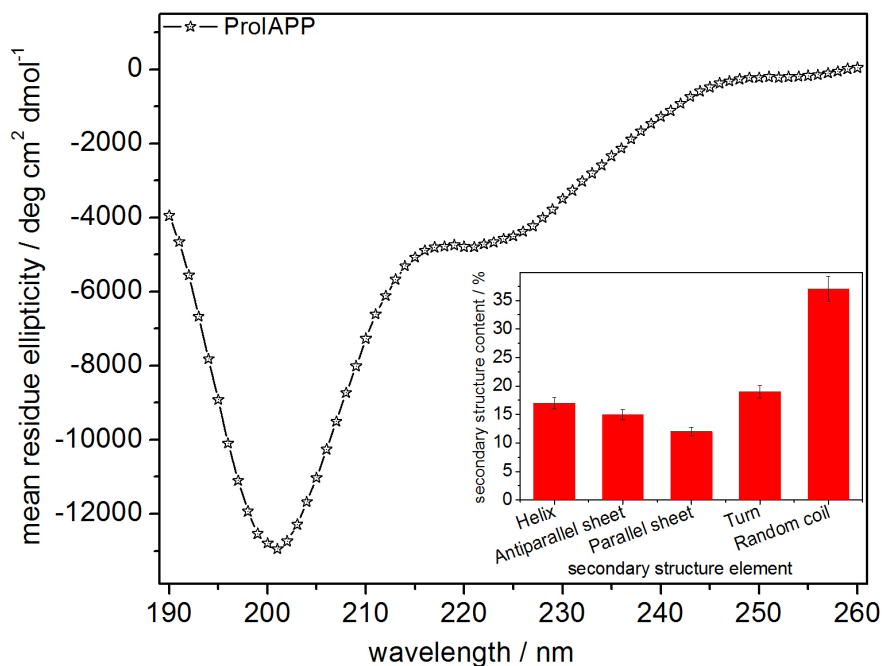

Figure 33: CD spectra of 10 µM proIAPP dissolved in 10 mM phosphate buffer, pH 7.4, at 25 °C. The inset shows the percentages of different secondary structures as obtained by the CDNN program (wavelength range 200 - 260 nm).
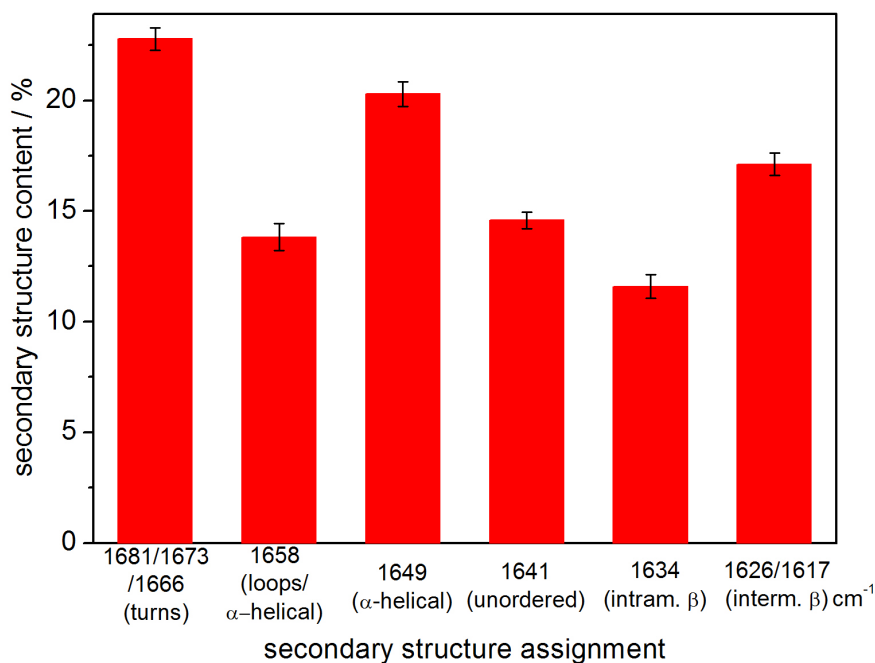

Figure 34: Secondary structure elements of the native structure of proIAPP dissolved in 10 mM phosphate buffer, pD 7.4, at 25 °C, as obtained by analysis of the FTIR data.

The FTIR spectrum of the native form of proIAPP (10 µM) was recorded to have a comparison with the ATR-FTIR data of the system containing the solid supported lipid bilayer membranes. Each spectrum was fitted multiple times with a similar set of sub-bands and slight variations of the starting conditions. Figure 34 shows the results of the fit including the corresponding error bars. Comparison of the secondary structure contents shows that proIAPP has predominantly unordered and turn structures.

3.3.2. Thoflavin T binding assay

As described in the previous chapters, Thioflavin T is used as amyloid specific dye to follow the fibrillation kinetics using fluorescence spectroscopy. The increase in the ThT emission maxima at 25 °C is monitored with time for 10 µM and 40 µM proIAPP, respectively, in the presence of DOPC:DOPG (7:3, w/w) as depicted in Figure 35 (for 10 µM proIAPP, no aggregation is observed over the time span shown). The fibrillation kinetics follows a nucleation dependent aggregation mechanism which includes a lag phase accompanied by nuclei formation, followed by an exponential growth phase and then a stationary phase, as shown in Figure 35. The lag phase is generally used to define the amyloidogenic propensity of a protein or peptide. The shorter the lag phase, the more amyloidogenic is the protein. As shown in Figure 35, 10 µM proIAPP does not show an increase in ThT intensity at 482 nm within the time frame of the measurement. However, the increase in concentration of proIAPP to 40 µM results in a lag phase of ~ 38 h followed by an exponential growth phase for ~ 2.5 h.

The data (Figure 35) clearly show that the presence of the anionic DOPC:DOPG (7:3, w/w) membrane triggers the fibrillation process of proIAPP, but above a critical concentration only. In the absence of the lipid bilayer, no aggregation has been observed up to 7 days even for 40 µM proIAPP at 25 °C. Within the same time period, aggregation of proIAPP was also not observed at membranes with significantly less anionic lipid contents, such as DOPC:DOPG ratios of 9:1 and 8:2, a pure zwitterionic (DOPC) lipid bilayer and at the DPPC:DOPC:cholesterol (1:2:1) model raft mixture.
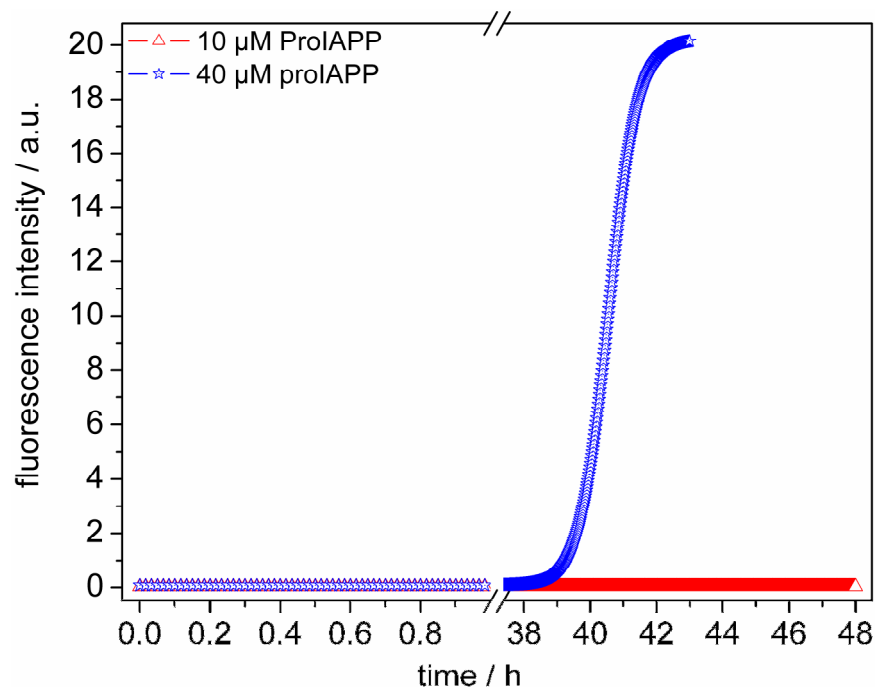
Figure 35: Thioflavin T – monitored amyloid fibril formation kinetics of 10 µM proIAPP (open red triangle), and of 40 µM proIAPP (open center dot blue star) in the presence of DOPC:DOPG (7:3, w/w) lipid vesicles. The experiments were carried out in 10 mM phosphate buffer, pD 7.4, at 25 °C.

Lastly, ThT measurements were also applied to observe the effect of the presence of proIAPP on the amyloidogenic propensity of human IAPP. Two molar ratios of proIAPP and hIAPP, 10 µM : 10 µm and 30 µM : 10 µM, were used, respectively (Figure 36). The ThT kinetics study for these mixtures with a mixing time of 4 min shows aggregation, but with prolonged lag phases compared to the pure hIAPP solution (Figure 36).
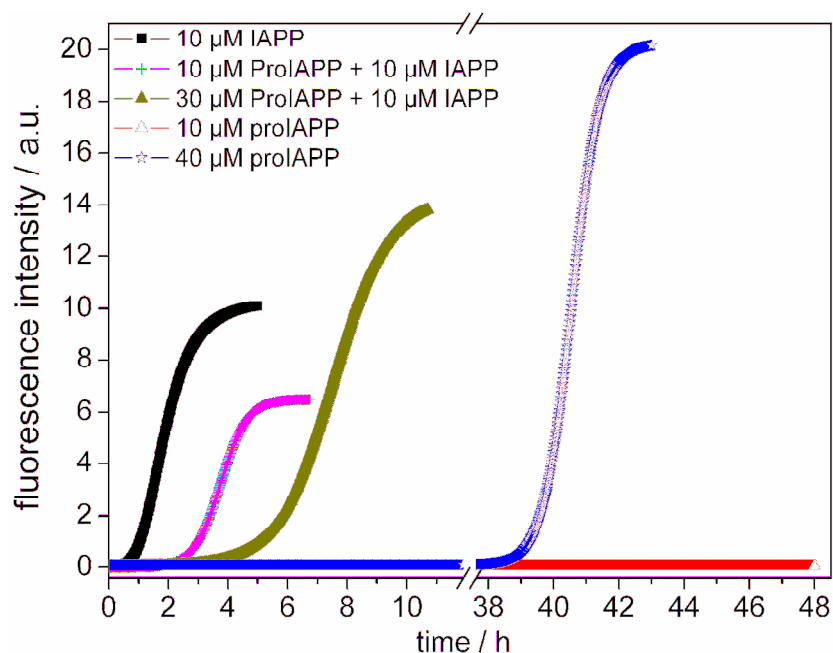
Figure 36: Thioflavin T – monitored amyloid fibril formation kinetics of 10 µM hIAPP (close black rectangles), 10 µM proIAPP (open red triangle), 10 µM proIAPP + 10µM hIAPP (magenta cross), 30 µM proIAPP + 10 µM hIAPP (close dark green triangle), and 40 µM proIAPP (open center dot blue star) in the presence of DOPC:DOPG (7:3, w/w) lipid vesicles prepared in 10 mM phosphate buffer, pD 7.4, at 25 °C.

3.3.3. ATR-FTIR spectroscopy study

The conformational changes of proIAPP were also studied in the presence of lipid interfaces at 25 °C using the ATR-FTIR spectroscopy. To evaluate the changes in secondary structure of proIAPP at the membrane interface supported on the IRE (internal reflection element)-crystal (Ge, germanium), we collected ATR-FTIR spectra over an interval of 30 min for 7 days after the injection of a 40 µM proIAPP solution into the ATR-cell (a 10 µM proIAPP solution did not show any amyloidogenic propensity at the membrane interface, Figure 35). Due to interfacial adsorption, the local concentration close to the IRE crystal surface and membrane increased with time, hence also the FTIR intensity. Subsequently, this adsorption was followed by an aggregation process. During the aggregation process, the peak maximum of the amide-I' band of proIAPP shifted from 1644 cm^{-1} to 1628 cm^{-1}. Figure 37 shows selected ATR-FTIR spectra of the time-dependent measurement, while Figure 38 represents normalized selected spectra.
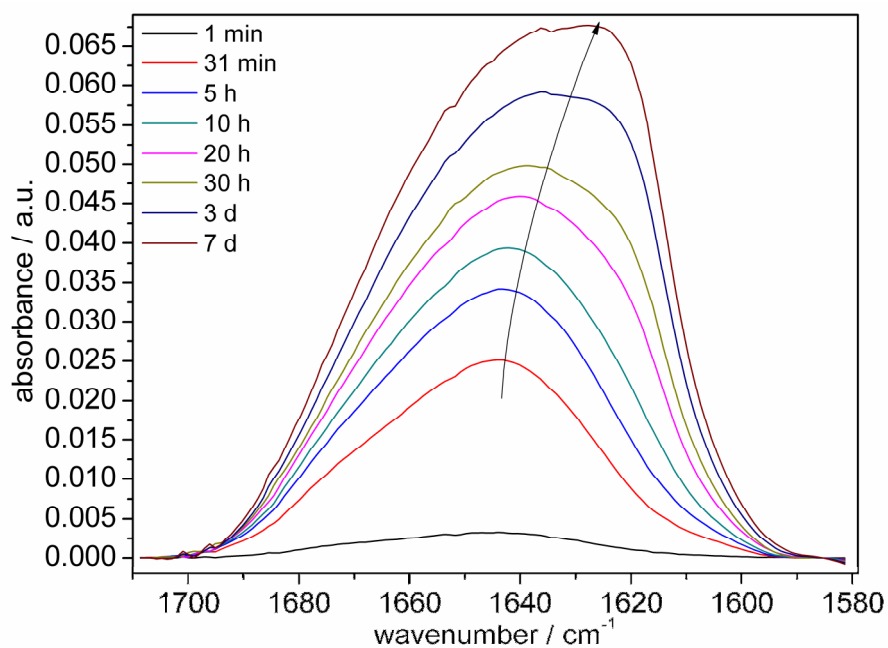
Figure 37: Time evolution of the amide-I' band of proIAPP upon adsorption at the DOPC:DOPG (7:3, w/w) membrane interface supported on an IRE crystal in the ATR-cell at 25 °C.
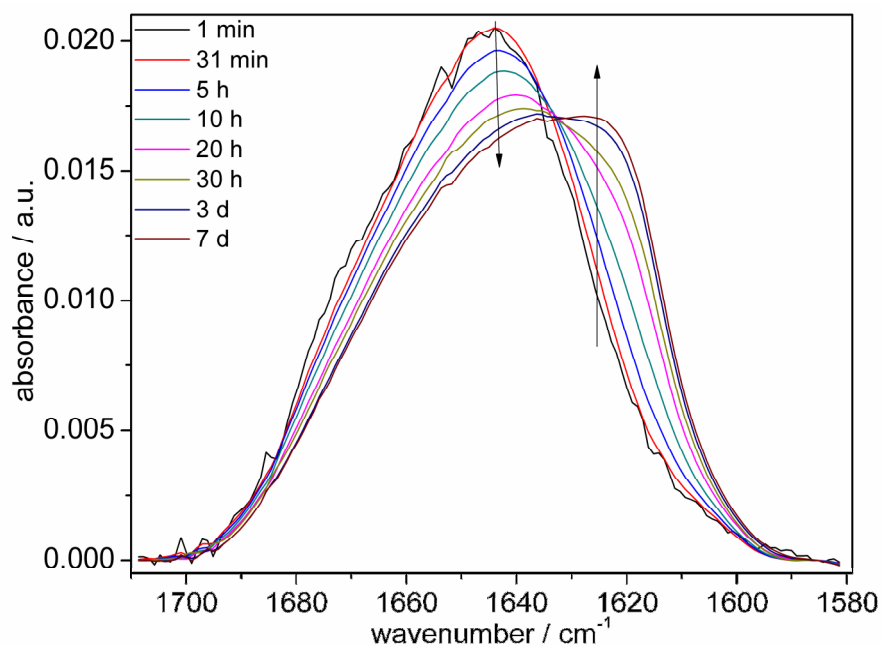

Figure 38: Time evolution of the normalized amide-I' band of proIAPP upon adsorption at the DOPC:DOPG (7:3, w/w) membrane interface.

The arrow in Figure 37 shows the gradual increase in amide-I' band intensity and shift upon adsorption to the membrane interface, while the arrows in Figure 38 depict the

decrease in the intensity of the amide-I' band at ~ 1647 cm^{-1} and the concomitant increase in the intensity at ~ 1628 cm^{-1} band over the time period measured.
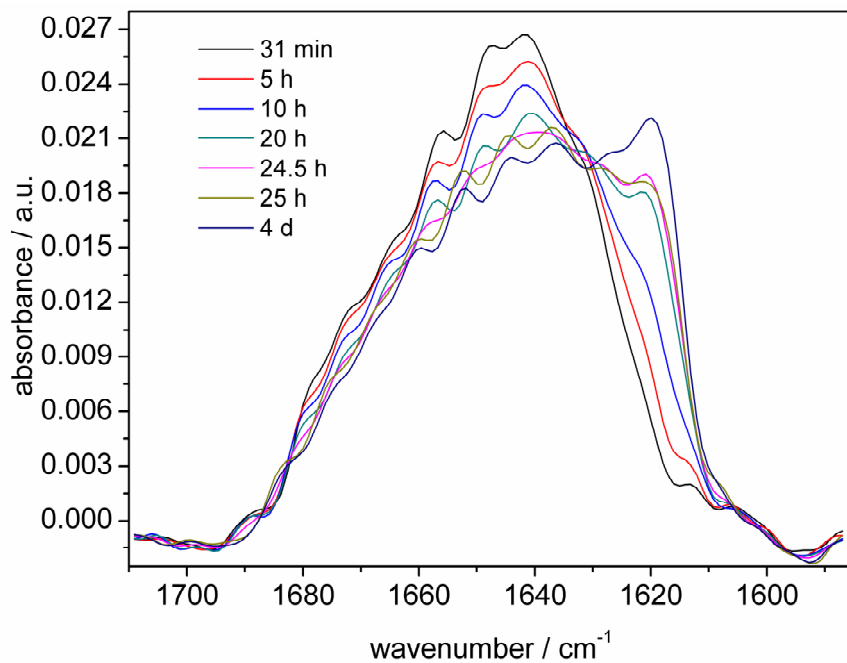

Figure 39a: Fourier self-deconvolution (FSD) spectra of the amide-I' band of proIAPP upon adsorption at the DOPC:DOPG (7:3, w/w) membrane interface.
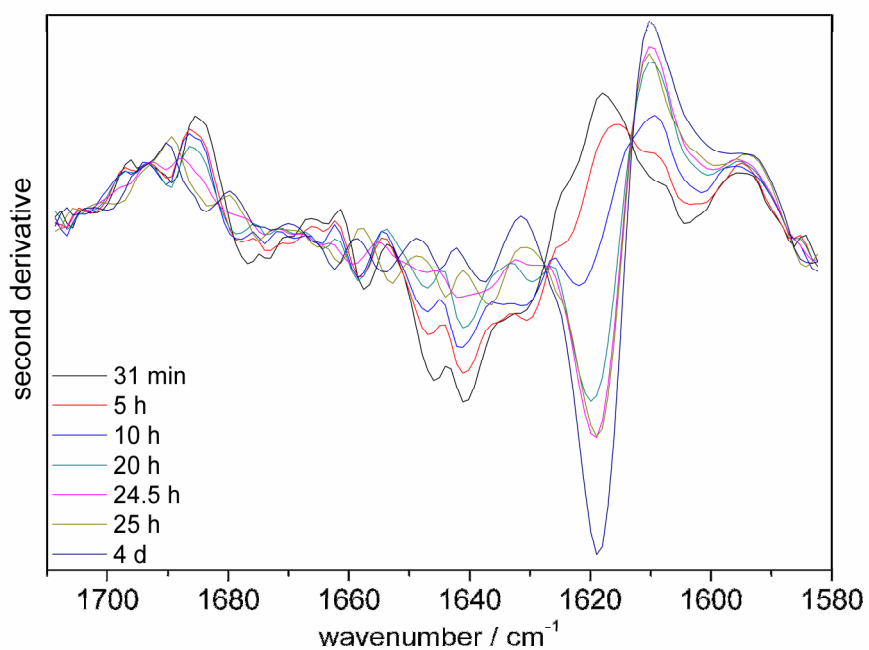

Figure 39b: Second derivative spectra of the amide-I' band of adsorbed proIAPP at the DOPC:DOPG (7:3, w/w) membrane interface.

Figures 39 a & b show the Fourier self deconvolution (FSD) and the second derivative data of time dependent spectra. They reveal seven distinct bands for native proIAPP, appearing at ~ 1678, 1674, 1665, 1657, 1647, 1641 and 1631 cm^{-1}, respectively. During the aggregation process, some of the bands shift to higher wavenumbers and two strong bands at ~ 1628 and 1619 cm^{-1} appear. Thereafter, peak fitting of the normalized spectra was performed for quantitative analysis of the underlying secondary structural changes.

Figure 40 shows the time evolution of the conformational changes within the first 40 h obtained by fitting the normalized curves for the respective seven bands. It is clear from the peak fitting that the major conformational changes happened with bands corresponding to ~ 1660 (loop), 1647 - 1653 (α-helical), and 1617 (intermolecular β-sheet) cm^{-1}. The bands corresponding to loops and α-helices followed a sigmoidal decrease, and the intermolecular β-sheet bands follow a sigmoidal increase with a lag phase of ~ 4 h respectively. Thus, proIAPP fibrillation at the DOPC:DOPG (7:3 w/w) membrane interface is accompanied by a decrease in loop and helical conformation and simultaneous gain in intermolecular β-sheet structural content. Besides intermolecular β-sheets, the intramolecular β-sheet (at 1635 cm^{-1}) content increases slightly from 12 to 14% with time.
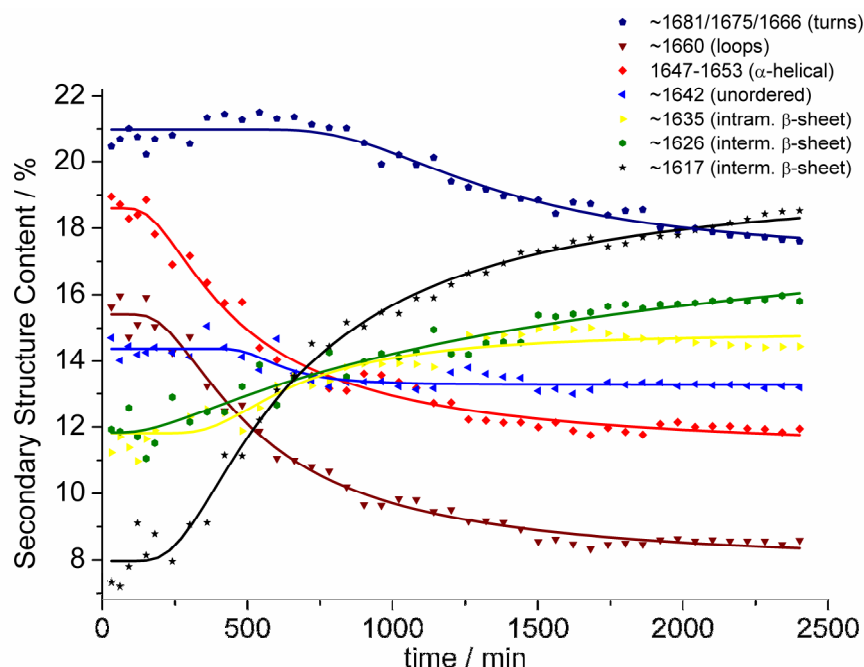

Figure 40: Time evolution of the secondary structural changes upon fibrillation of 40 µM proIAPP on the DOPC:DOPG (7:3, w/w) anionic membrane interface, derived from peak-fitting of the normalized ATR-FTIR spectra.

To investigate the effect of varying lipid compositions, additional ATR-FTIR experiments on 40 µM proIAPP were performed in the presence of pure DOPC bilayers and of bilayers composed of a lipid raft mixture, DOPC:DPPC:Chol (1:2:1). Figures 41 and 42 exhibit the time evolution of the corresponding amide-I' bands.
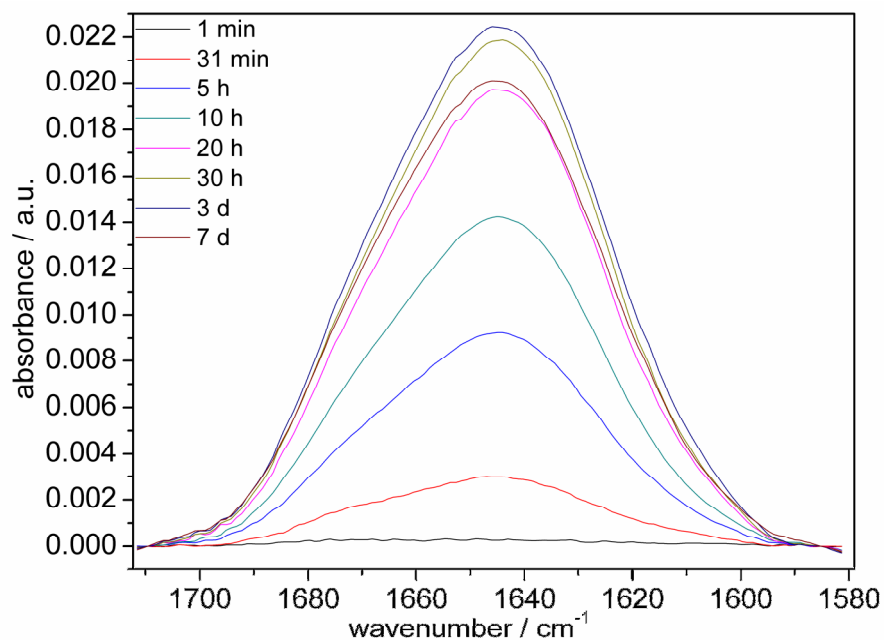
Figure 41: Time evolution of the amide-I' band of proIAPP upon adsorption at the pure DOPC membrane over a period of 7 days at 25 °C.

In case of pure DOPC (Figure 41), only adsorption of proIAPP at the membrane interface without any subsequent changes in amid-I' band frequency was observed. However, adsorption at the raft mixture was accompanied by the appearance of a shoulder in the intermolecular β-sheet region after 3 days, which further evolved upto 7 days (Figure 42).
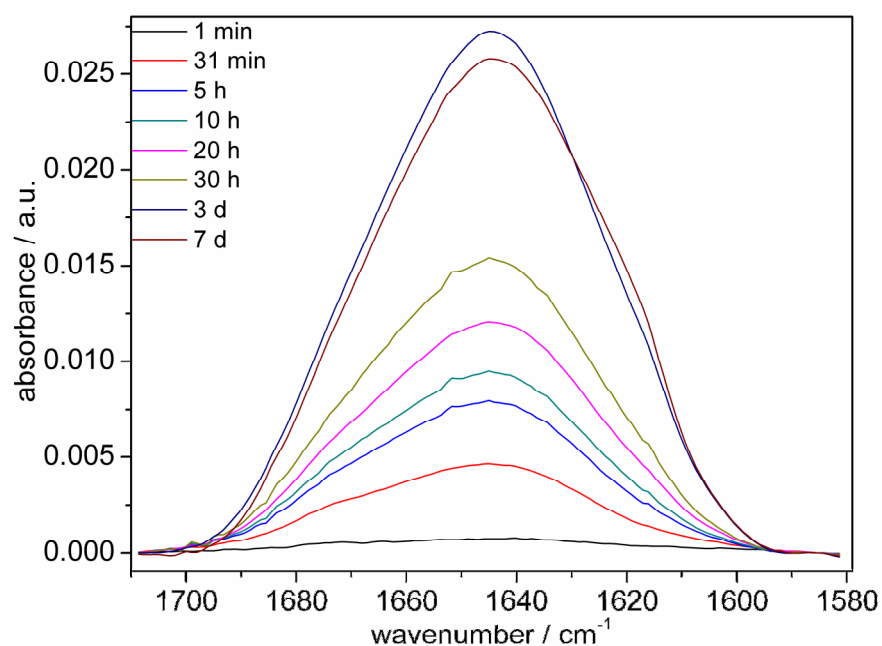
Figure 42: Time evolution of the amide-I' band of proIAPP upon adsorption at a heterogeneous raft membrane consisting of DOPC:DPPC:Chol (1:2:1) over the period of 7 days at 25 °C.

Thus, the presence of a pure zwitterionic lipid bilayer membrane (DOPC) has no effect on the amyloidogenic propensity of proIAPP, while the heterogeneous raft membrane has a minor effect, only. The kinetics of aggregation at the heterogeneous raft membrane is very slow, and the aggregate structure does not seem to be well ordered.

Finally, we also checked the presence of proIAPP on the amyloidogenic propensity of human IAPP at the anionic DOPC:DOPG (7:3, w/w) interface. The adsorption kinetics of the hIAPP:proIAPP equimolar mixture is relatively slow in comparison to hIAPP (Figure 43, upper panel), and the same holds true for the fibrillation kinetics (Figure 43, lower panel). Notably, the final adsorption and intermolecular β-sheet intensities are smaller for hIAPP in comparison to the peptide mixture, which could be attributed to a seed-induced co-fibrillation of the proIAPP. The longer lag and elongation phase of the proIAPP + IAPP mixture could be attributed to the interaction and complex formation between the highly amyloidogenic core of hIAPP and distinct regions, such as the pro-region, of the proIAPP molecules.
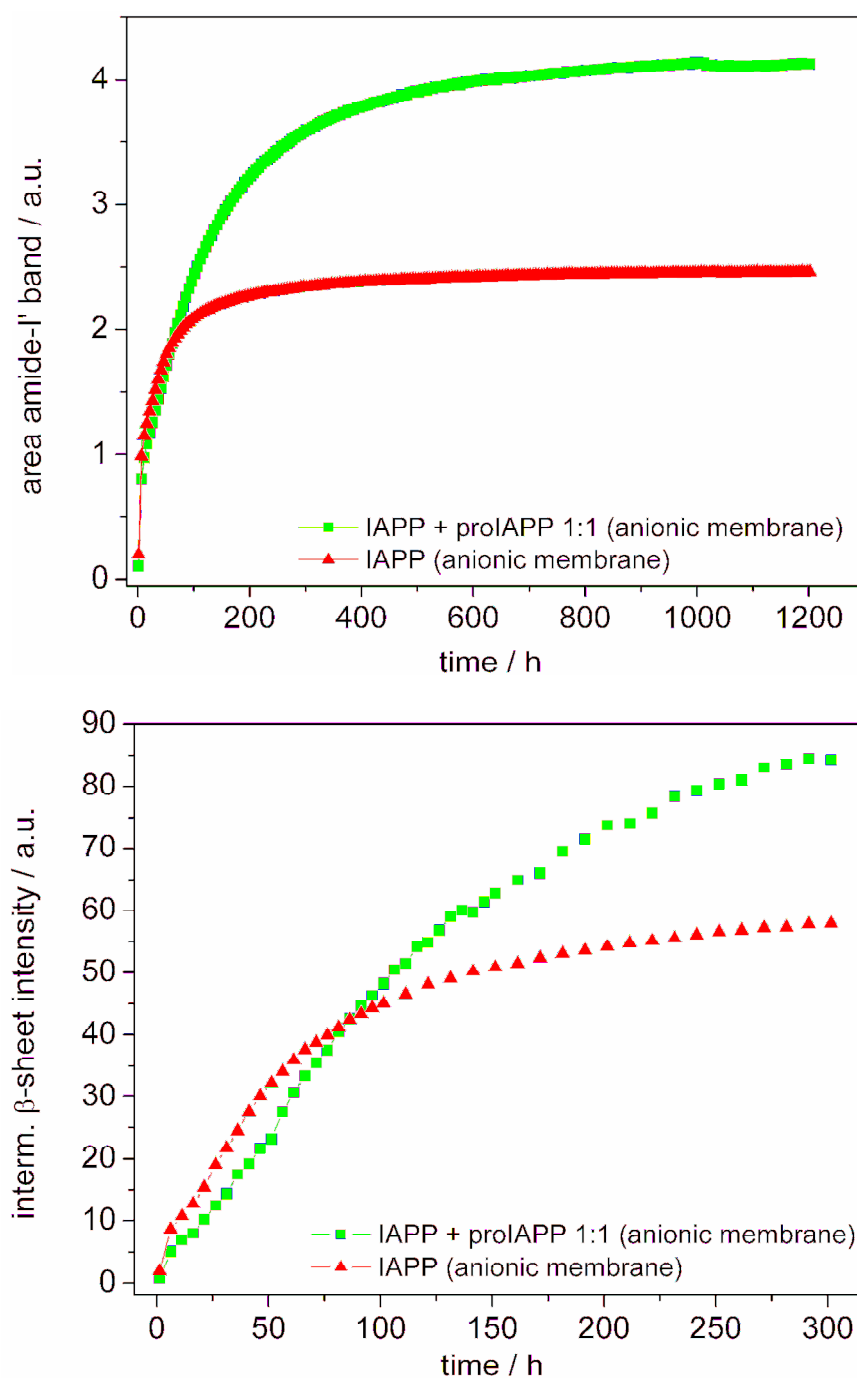
Figure 43: Upper panel: Adsorption kinetics of a mixture of hIAPP and proIAPP (1:1, each 10 µM) in the presence of an anionic (DOPC:DOPG, 7:3) membrane and of hIAPP under the same conditions, followed by integration of the amide-I' band between 1710 and 1585 cm^{-1}. Lower panel: Depicts the corresponding intermolecular β-sheet content with respect to the whole amide-I' area of hIAPP and the equimolar mixture of hIAPP and proIAPP (10 µM each), in the presence of the anionic membrane.

3.3.4. AFM study

Atomic force microscope (AFM) is used here to reveal the morphology of the protein aggregates, also in the presence of membraneous interfaces (*22, 108*). Here, the spin-coating method is used to prepare the samples, followed by freezing and drying in a lyophilizer to decrease the drying time. This protocol for the AFM sample preparation minimizes the surface-induced aggregation effects. Unlike other membrane-induced fibrillating systems, such as hIAPP (*22, 24, 109*), proIAPP is found to form oligomeric or small fibrillar structures, only. Notably, there was no major spectral difference in the ATR-FTIR data for these two peptides, hence the different aggregates (the large oligomeric vs. fibrillar ones) must essentially differ in the packing properties of the aggregating units, only. Figure 44 depicts characteristic AFM images of 40 µM aggregated proIAPP in the presence of the anionic lipid bilayer. Essentially oligomeric structures were found with heights in the range of 2.5 – 3.5 nm. Along with these oligomeric species, a minor population of small fibrillar structures having lengths of 50 – 55 nm was found as well. A similar analysis for 40 µM proIAPP in bulk solution under the same conditions up to seven days did not show either significant secondary structural changes (measured by ATR-FTIR spectroscopy) or changes in the morphology (determined by AFM).

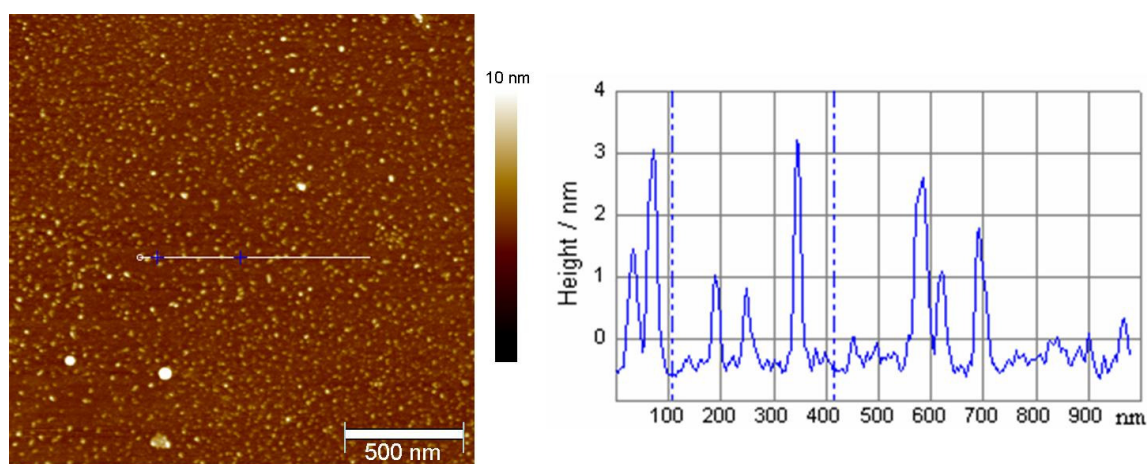**Figure 44:** AFM image of proIAPP, aggregated at a concentration of 40 µM in the presence of the DOPC/DOPG (7:3 w/w) membrane at 25 °C for 7 days (left), and the corresponding height scale (right).

3.3.5. Discussion

The main focus of this part of the thesis was to reveal the time scale and underlying mechanisms of the fibril formation of proIAPP in the presence of lipid membranes. Besides

anionic membranes (DOPC:DOPG, 7:3), zwitterionic and model raft mixtures were also used as model membrane systems for the interaction studies. In fact, lipid membranes seem to constitute the preferred loci of aggregation and probably also of cytotoxicity (*22, 24, 109*). The secondary structures of proIAPP were first determined after injection of the sample to capture their starting conformation, using CD and FTIR spectroscopy. Both methodologies present proIAPP as predominantly random coil structure with little percentage of ordered secondary structure content.

The fibrillation kinetics monitored with the ThT assay (Figure 35) shows that proIAPP, which does not show any amyloidogenic propensity in the absence and in the presence of anionic membrane (DOPC:DOPG, 7:3) at lower concentration (< 40 µM), undergoes aggregation with a lag phase of ~ 39 h. Certainly, different lag and growth times are seen in different sample environments, such as in the ATR-cell, where the lag time for 40 µM proIAPP was in the range of ~ 4 h in the presence of anionic lipid membrane. Differences in time scale are due to the difference sample geometry and vesicle preparations. In the presence of supported phospholipid bilayers (lipid bilayer on IRE crystal), the signal is due to the concentration increase of the peptides upon adsorption at the flat lipid interface, while in the ThT kinetic assay, the peptides interact with large spherical unilamellar vesicles (LUVs). Thus, a strong self association potential is achieved for proIAPP in the presence of anionic membranes. Nevertheless, proIAPP showed very low amyloidogenic propensity. This low amyloidogenic propensity of proIAPP may be rationalized by the increased net charge on the N- and C- termini in comparison to hIAPP (see Figure 2), which is known for its amyloidogenic propensity and shares its primary sequence with proIAPP (*17*). Moreover, Figure 37 reveals that when the proIAPP concentration at the anionic membrane interface exceeds a critical concentration (because of adsorption at the interface), the aggregation is observed by ATR-FTIR measurements. Thus, in proIAPP aggregation, the adsorption is the preceding step of the fibrillation process, followed by self-assembly of adsorbed proIAPP molecules at the anionic lipid interface (for a schematic representation of such mechanism, see Figure 6). Additionally, proIAPP does not adsorb and aggregate significantly in the presence of the pure zwitterionic fluid DOPC membrane within a time period of up to 7 days. Conversely, in the

presence of the zwitterionic but heterogeneous model raft membranes, proIAPP seems to cluster into less-ordered structures, with slower kinetics.

Unlike other amyloidogenic peptides, proIAPP forms mainly small oligomeric-like disordered structures at the anionic lipid membrane interface, having heights of ~ 3.5 nm. These heights correspond to the heights of normal fibrils, which vary typically from 2 nm (in the case of hIAPP fragments (*110, 111*) and α-synuclein (*112*)) to 6 nm (e.g., for hIAPP (*113*), insulin (*114, 115*)). This difference in morphological structure of proIAPP may be attributed to the presence of the pro-region, i.e., its C- and N- termini flanking the amyloidogenic core, which largely corresponds to the primary sequence of the highly amyloidogenic hIAPP. It may be rationalized that due to these additional ends, efficient packing into ordered fibrillar structures is hampered, thus leading to the more disordered oligomeric aggregate structures observed by AFM for proIAPP.

It was also observed that the addition of proIAPP to hIAPP delays the rate of hIAPP fibril formation, probably by some kind of complex formation. A 1:1 molar mixture of proIAPP and hIAPP increased the lag phase by a factor of ~ 3 h (Figure 36). Thus, it appears reasonable to speculate that the pro-region of the proIAPP prolongs the fibrillation kinetics of the highly amyloidogenic peptide, hIAPP. In fact, it has been speculated that part of the function of hIAPP processing intermediates, like proIAPP, may be to prevent aggregation and amyloidogenesis in the early stages of hIAPP biosynthesis and transport (*17*). Particularly, in the case of excess proIAPP, increased aggregation levels have finally been observed, which could be attributed to a seed-induced co-fibrillation of proIAPP. Reports on the aggregation of other systems where similar proteins have been compared, such as different insulin constructs or homologues of lysozyme (*116, 117*), are still scarce, so that generalizations are difficult to make. However, it is clear that seeding of peptide fibril formation depends strongly on the similarity of their sequences, which is largely fulfilled for hIAPP and its propeptide, proIAPP.

3.4. The effect of seeds on the fibrillation of peptides secreted from pancreatic β-cells

As mentioned in the introduction, the amyloid stability appears to be derived from a combination of forces, including but not limited to H-bonding, like the stabilizing forces of globular proteins. This includes the stacking of side chains from different peptides/proteins,

along with the H-bonding between backbones of different peptide molecules. It has been known that amyloidogenesis is an inherent property of proteins/peptides; even non-amyloidogenic proteins/peptides undergo amyloid fibril formation under certain conditions. Thus, it is important to know how the seeds from one amyloidogenic peptide can affect the amyloidogenic propensity of other amyloidogenic or non-amyloidogenic peptides or proteins that are stored, processed, and secreted together. The seeds of Aβ fibrils have shown to modulate the fibrillation of IAPP and *vice versa* (*118*), while these two peptides are secreted by the distantly located organs of the human body. Hence, it seems reasonable to execute the cross-seeding experiments between IAPP, insulin, and proIAPP. Moreover, the outcome of this set of experiments will also shed some light on the possibility of intracellular fibrillation of proIAPP and its involvement in the extracellular plaque formation, which has been found in over 90% of the pancreas of T2DM patients (*5*).

Thus, in order to understand proIAPP involvement in T2DM, we explored the modulation of proIAPP fibrillation by IAPP and insulin seeds and *vice versa*, by employing fluorescence and ATR-FTIR spectroscopy as well as AFM.

3.4.1. Thioflavin T binding assay

The thioflavin T (ThT) dye was used to track the aggregation kinetics of peptides and proteins in the presence and absence of seeds from different amyloidogenic peptides. As described in the materials and methods section, the ThT emission intensity at 482 nm increases upon binding to amyloid fibrils. Since the steps of fibril formation and ThT binding are simultaneous processes, an increase in ThT emission intensity at 482 nm was observed as the fibrillation kinetics of different amyloidogenic peptides under their respective conditions. ProIAPP seeds for the cross-seeding reaction were taken from the stationary phase of proIAPP fibrillation in the presence of 0.1 mM SDS (Figure 26), where proIAPP was shown to form only oligomeric structures as observed by AFM.

As has been shown in Figure 45, IAPP fibrillation follows a sigmoidal curve with a lag phase of ~ 7 h, followed by an exponential growth phase for ~ 8 h. The addition of 4% proIAPP seeds to the IAPP fibrillation reaction mixture enhances the fibrillation rate, significantly. The lag phase reduces to ~ 1.5 h, and the exponential growth phase to 1 h. Hence, the presence of 4% proIAPP seeds in the IAPP fibrillation reaction enhances the

amyloidogenic propensity by fourfold. Moreover, the final ThT intensity of IAPP solution was also enhanced in the presence of proIAPP seeds (Figure 45).
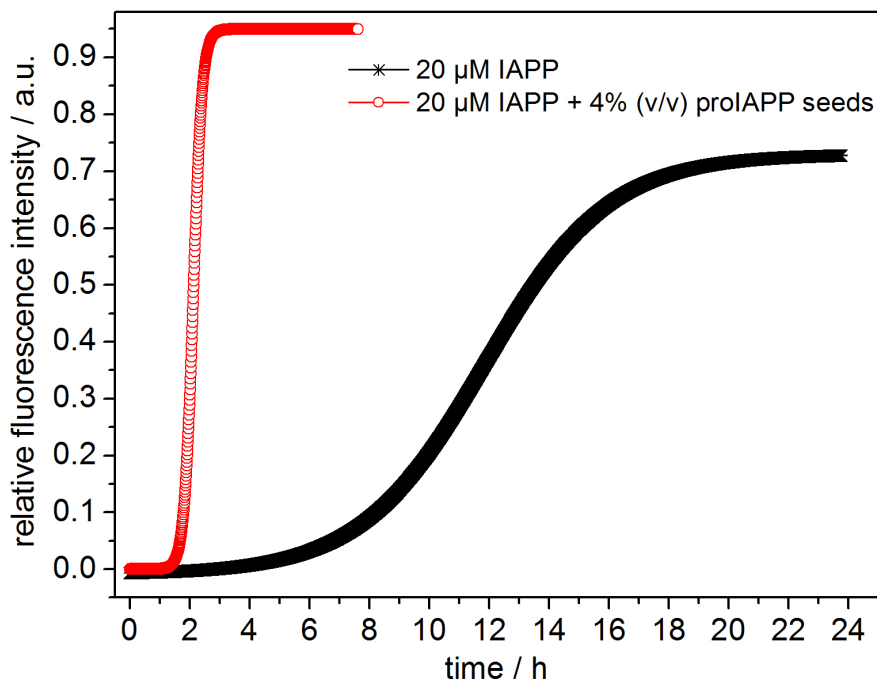

Figure 45: Thiflavin T monitored amyloid fibril formation of 20 μM IAPP in the absence (open black crosses) and presence (open red circles) of 4% (v/v) proIAPP seeds. The experiments were carried out in 10 mM phosphate buffer, pH 7.4, at 25 °C.

Insulin, which normally does not aggregate under physiological conditions at room temperature, was shown to form amyloid fibrils at a concentration of 0.5% (w/w), pH 2, at 60 °C (*28*). This protocol was used to observe the effect of proIAPP seeds on the fibrillation kinetics of insulin (Figure 46).

Insulin, like IAPP, follows a sigmoidal fibrillation kinetics with a lag phase of ~ 18 h followed by an exponential growth phase of ~ 14 h. The presence of 4% proIAPP seeds is only able to enhance the nucleation rate, but not the elongation rate of insulin fibrillation. Here, insulin follows fibrillation kinetics with a lag phase of ~ 10 h and an exponential growth phase of ~ 14 h (Figure 46). Moreover, the final ThT intensity is higher in the presence of proIAPP seeds, as also observed for the IAPP fibrillation upon addition of proIAPP seeds.
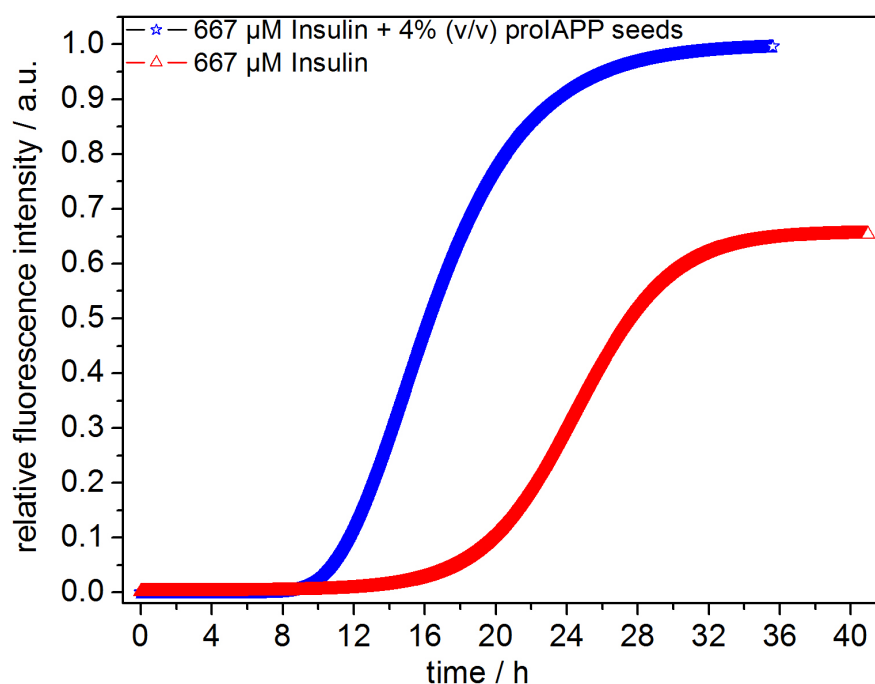
81

Figure 46: Thiflavin T monitored amyloid fibril formation of 667 µM insulin in the absence (open red triangles) and presence (open red circles) of 4% (v/v) proIAPP seeds. The experiments were carried out in H$_2$O-HCl buffer, pH 2, at 60 °C.

Thus, proIAPP seeds were able to enhance the amyloidogenic propensity of insulin and IAPP in their respective studied conditions. Thioflavin T binding assays were also done to underline the amyloidogenic propensity of proIAPP in the presence of IAPP and insulin fibrils. The 20 µM ProIAPP did not show any amyloidogenic propensity in the presence of respective 4% (v/v) seeds, as measured for 7 days in 10 mM phosphate buffer, pH 7.4, at 25 °C.

3.4.2. ATR-FTIR spectroscopy study

Attenuated total reflection Fourier transform infrared spectroscopy was used to determine the arrangement of amide bond in amyloid fibrils grown in the presence and absence of seeds. IAPP in the presence of proIAPP seeds shows a prominent band at ~ 1623 cm^{-1} along with a shoulder around 1646 cm^{-1} (Figure 47). However, IAPP fibrils, which were grown in the absence of proIAPP seeds, did not adsorb onto the silicon crystal at the beginning, therefore no signal was observed at time 0 h. Upon drying, significant absorbance of the amide-I' band region corresponding to 1658 cm^{-1} and a shoulder at 1628 cm^{-1} was observed (Figure 48). The wavenumber 1658 cm^{-1} corresponds to a mixture of α-

helical and turn conformations of IAPP that was attained upon adsorption to the silicon ATR crystal, and the 1628 cm^{-1} band corresponds to the intermolecular β-sheets of an aggregated fraction of IAPP that settles onto the silicon crystal during the drying process.

Figure 47: Amide-I' vibration characteristics of IAPP fibrils, fibrillated in the presence of 4% proIAPP seed in 10 mM phosphate buffer, pH 7.4, at 25 °C.

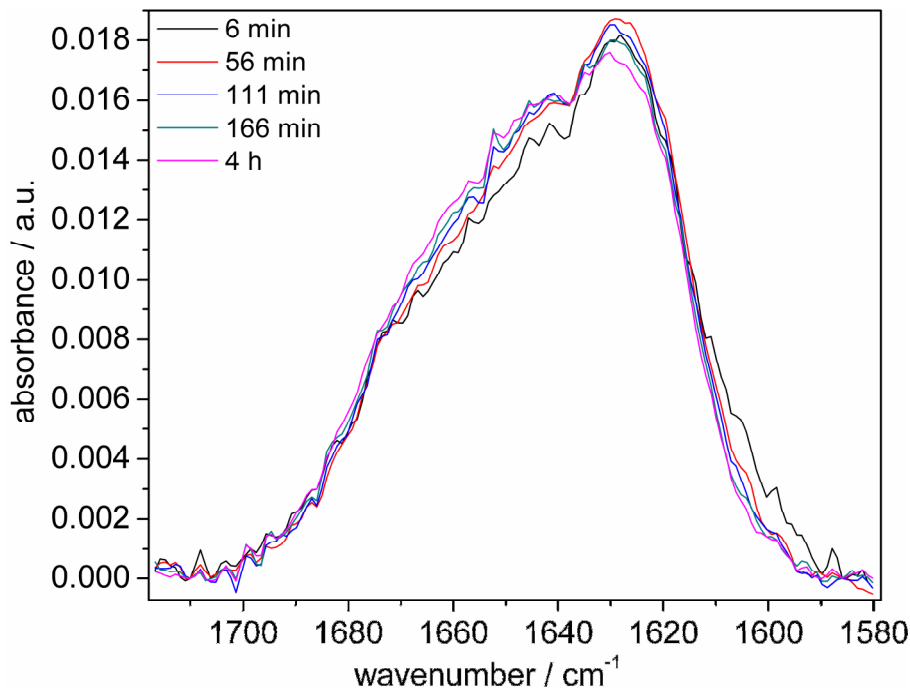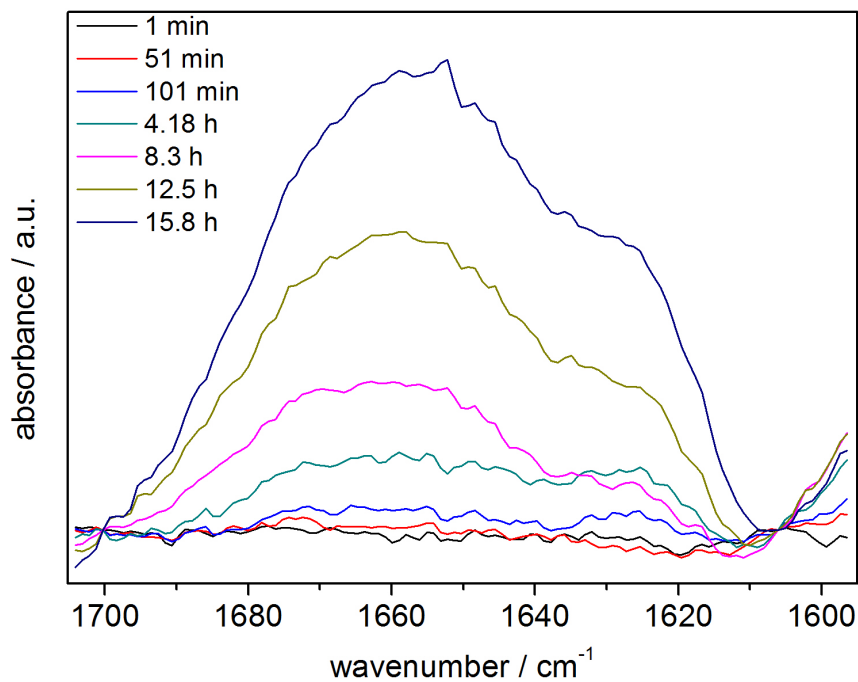**Figure 48:** Amide-I' vibration characteristics of IAPP fibrils, fibrillated in the absence of proIAPP seeds in 10 mM phosphate buffer, pH 7.4, at 25 °C.

The amide-I' band spectra (after 3 min) of insulin fibrils grown in the presence of proIAPP seed, show a prominent peak around 1637 cm^{-1} and a shoulder at ~ 1651 cm^{-1}, indicating that the insulin fibrils have predominantly α-helices and intramolecular β-sheets content (Figure 49). The peak and shoulder corresponding to 1637 and 1651 cm^{-1} wavenumbers shifts to 1627 and 1657 cm^{-1} wavenumbers upon drying on the silicon crystal. This peak shift is also accompanied by increase in absorbance at 1627 cm^{-1} peak.

Figure 49: Amide-I' vibration characteristics of insulin fibrils, fibrillated in the presence of 4% proIAPP seeds in H$_2$O-HCl buffer, pH 2, at 60 °C.

Insulin fibrils grown in the absence of proIAPP seeds show an amide-I' band with a prominent peak corresponding to intermolecular β-sheets around 1627 cm^{-1} and a shoulder at 1661 cm^{-1} that upon drying show increase in absorbance, only. This shows that not all of the 667 μM insulin did fibrillate in the bulk, as revealed by the increase in the absorbance at 1627 cm^{-1} during drying on the silicon crystal (Figure 50).

Thus, at beginning the shape of amide-I' band of insulin fibrils grown in the presence of proIAPP seeds, appeared to be rather similar to IAPP fibrils grown in the presence of proIAPP seeds (Figures 47 & 49), but with drying on crystal, the amide-I' band shape

changed to the one shown by insulin fibrils grown in the absence of proIAPP seeds (Figure 50)

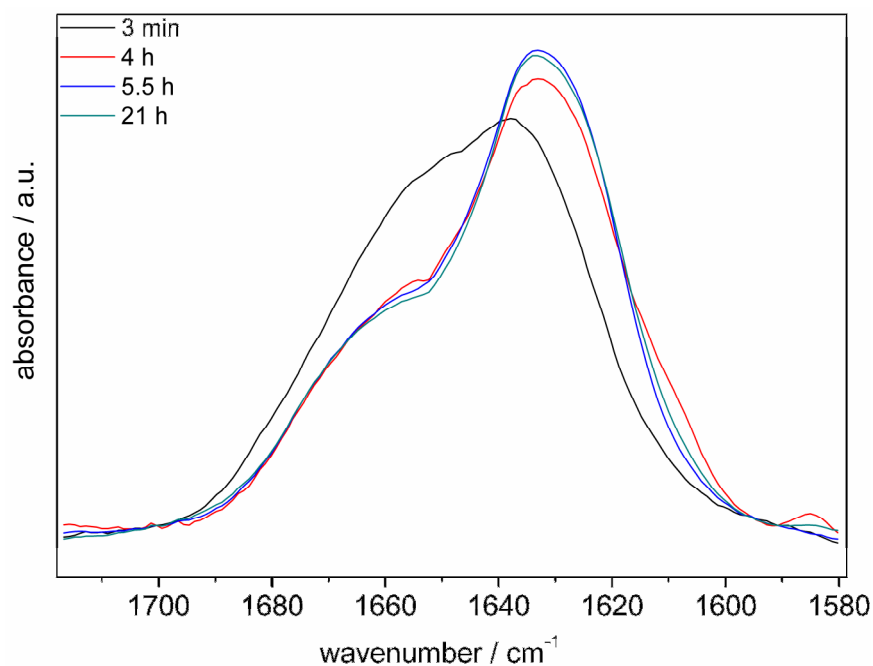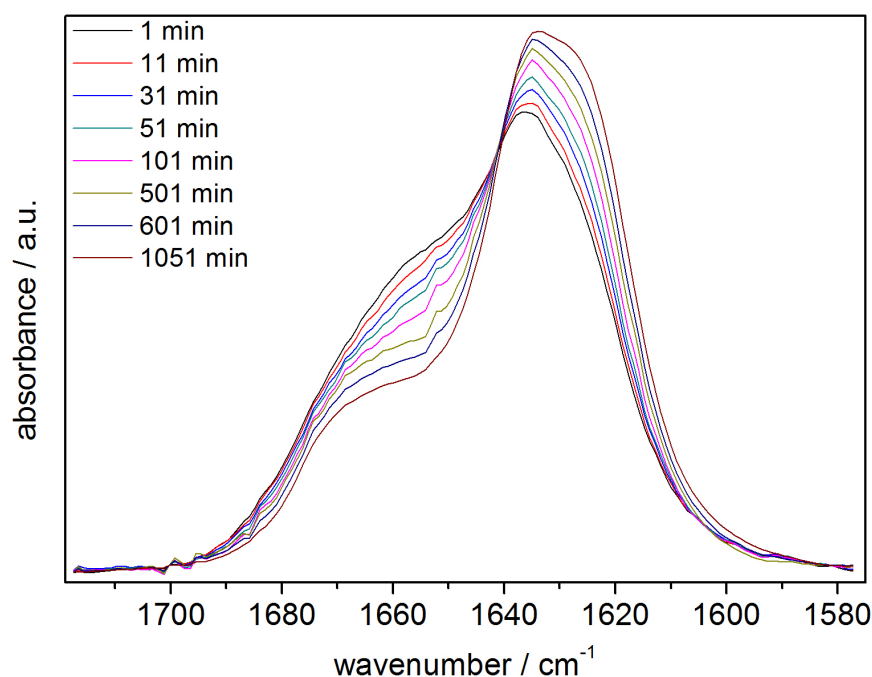**Figure 50:** Amide-I' vibration characteristic of insulin fibrils, fibrillated in the absence of proIAPP seed in H$_2$O-HCl buffer, pH 2, at 60 °C.

3.4.3. AFM study

The morphologies of the fibrils grown in the presence and absence of seeds from the different amyloidogenic proteins or peptides were checked by AFM. ProIAPP did not show any fibrillar morphology in the presence or absence of IAPP and insulin fibrils under the conditions studied. However, proIAPP seeds had very different and varied effects on the fibrillar morphology of IAPP and insulin fibrils. As shown in Figure 51, insulin forms mainly amorphous, oligomeric or short fibrils in the absence of proIAPP seeds, in the studied condition as mentioned in the figure legend. The height of fibrils was found to be in the range of 5 - 6 nm.

The presence of proIAPP seeds in the insulin fibrillation reaction mixture enhanced the fibrillation of insulin as observed by the ThT binding assay and the same was observed by AFM as well. Insulin was found to attain discrete fragmented and long fibrillar morphologies in the presence of proIAPP seeds. These fibrils were found to have a height of 3 - 4 nm (Figure 52).
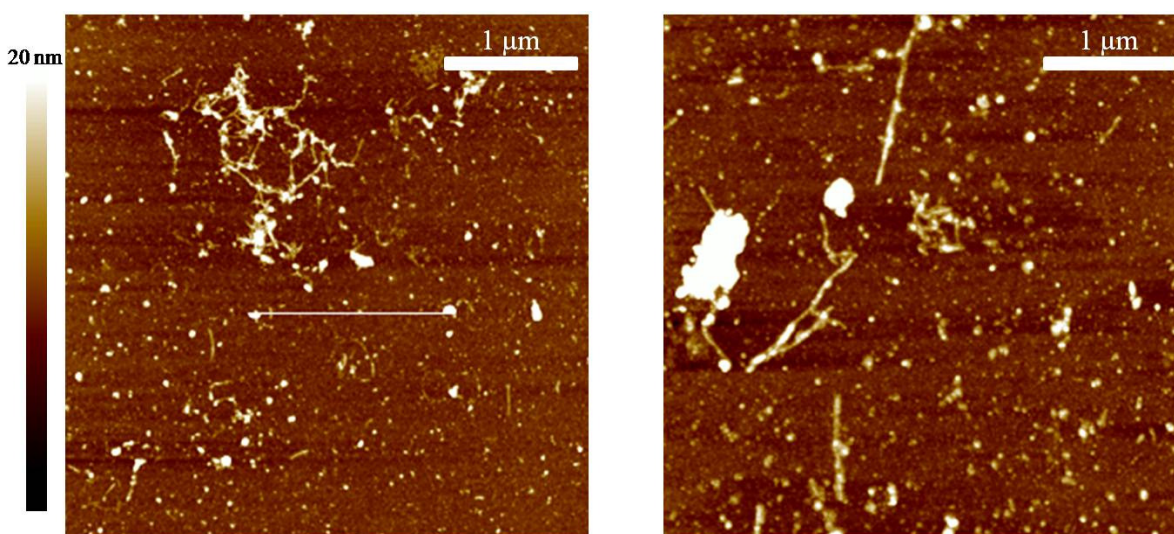
Figure 51: AFM images of insulin aggregated at a concentration of 667 µM in H$_2$O-HCl buffer, pH 2, 60 °C, at two different places (4x4 µm resolution).
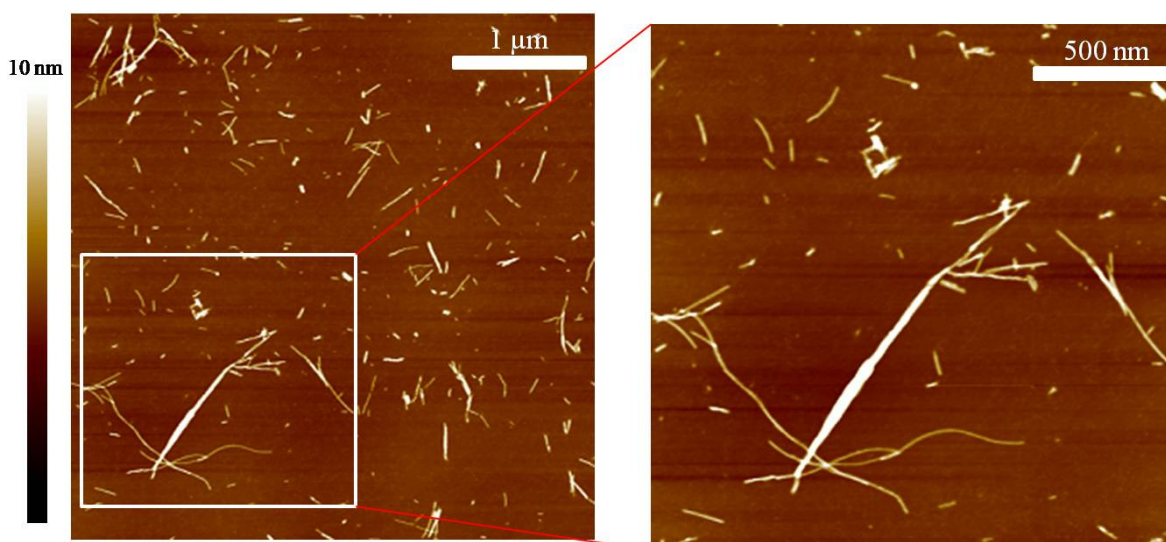
Figure 52: AFM images of insulin, aggregated at a concentration of 667 µM in H$_2$O-HCl buffer, pH 2, 60 °C containing 4% proIAPP seeds, at 4x4 µm (left), 2x2 µm resolution (right).

On the other hand, the fibrillar morphology of IAPP was drastically affected by the presence of proIAPP seeds. IAPP, in the absence of proIAPP seeds, was found to form long mature fibrils with a height of 4 - 5 nm (shown in Figure 53). IAPP forms amorphous aggregates along with the fibrils at the conditions studied here, as observed by the AFM images.
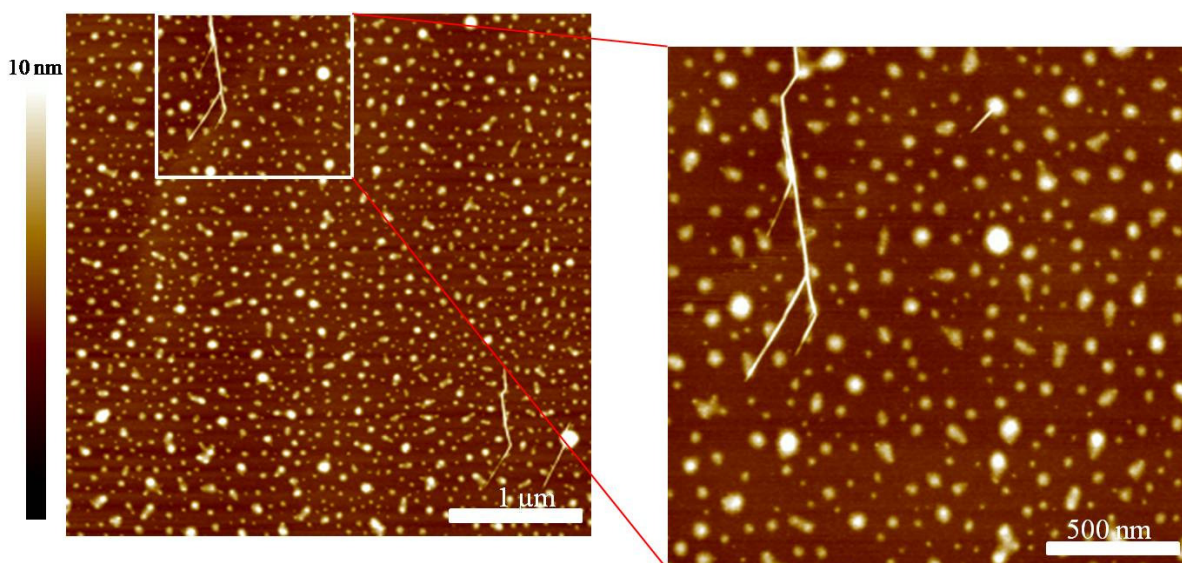
Figure 53: AFM images of IAPP, aggregated at a concentration of 20 μM in 10 mM phosphate buffer, pH 7.4, 25 °C, at 4x4 µm resolution (left), 2x2 µm resolution (right).

The proIAPP seeds added to the IAPP fibrillation reaction trapped the fibril formation in oligomeric species, only. IAPP is found to form predominantly oligomers in the presence of proIAPP seeds, with a height of 3 - 4 nm (Figure 54). The amorphous morphologies were absent in the AFM scan of the samples prepared from IAPP fibrillation reaction in the presence of proIAPP seeds (Figure 54), unlike the unseeded IAPP fibrillation (Figure 53).

Figure 54: AFM images of IAPP, aggregated at a concentration of 20 μM in 10 mM phosphate buffer, pH 7.4, 25 °C containing 4% (v/v) proIAPP seeds, at 4x4 µm resolution.
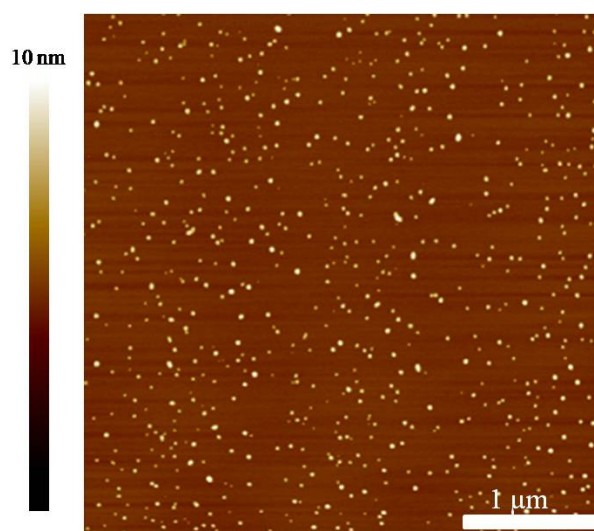
3.4.4. Discussion

The proIAPP fibrils grown in the presence of 0.1 mM SDS formed mainly oligomers, as revealed by both AFM and ThT measurements. These structures were used as seeds for the fibrillation of IAPP and insulin, and vice versa. These studies were executed in order to reveal the potential role of proIAPP in enhancing the amyloidogenic propensity of IAPP and insulin, respectively, all three peptides being produced by islet β-cells, an aspect that might be relevant for the onset of T2DM. Different combinations of seeds and fibrils of these three peptides/proteins were tested for such effects. It was revealed that pre-formed seeds of IAPP and insulin had no effect on the amyloidogenic propensity of proIAPP, which shows no amyloidogenic characteristics in the absence of either seeds. This finding indicates that seeds of IAPP and insulin are not compatible as templates for proIAPP fibrillation. However, the seeds of proIAPP fibrils were able to enhance the amyloidogenic propensity of IAPP and insulin under their respective amyloid forming conditions, acting as templates for fibrillation. The lag phase was reduced in the fibrillation reaction of both peptides. IAPP shows drastic changes in its amyloid morphology in the presence of proIAPP fibrils. This may be explained through the amino acid sequence that proIAPP shares with IAPP; proIAPP is the precursor of IAPP. Thus, the proIAPP seeds provide a platform for an earlier onset of exponential growth, compared to IAPP fibrillation in the absence of proIAPP seeds. IAPP aggregates formed in the absence of proIAPP seeds exhibit both amorphous and fibrillar morphologies, as revealed by the AFM analysis. In a concomitant ATR-FTIR experiment, IAPP did not show any initial amide-I' band, which suggests that IAPP was already aggregated in the bulk solvent and no significant adsorption at the silicon crystal was observed. However, upon drying with time, the amide-I' band began to appear. The broad peak around 1658 cm^{-1} and the shoulder at 1628 cm^{-1} reveals that this structure contains more amorphous aggregates than ordered aggregates (Figure 48), as confirmed by the AFM scans of the sample (Figure 53). This can be attributed to the higher concentration of IAPP used in the study. Otherwise, IAPP forms normally fibrillar structures, only. ProIAPP seeds can be used by IAPP molecules as templates for fibrillation, hence the major population of IAPP underwent an ordered (fibrillar) aggregation instead of an amorphous one, as shown by the ATR-FTIR spectra (Figure 47)

and AFM images (Figure 54). This modulation of IAPP fibrillation was also observed in the ThT kinetics assay (Figure 45).

The amyloidogenic propensity of insulin was also enhanced in the presence of proIAPP, but not as drastic as observed for IAPP. This could be rationalized by the sequence similarity of proIAPP, IAPP and insulin. Since proIAPP shares its primary sequence with IAPP (hence some congruent side chain stacking and hydrogen bonding between the backbone of the two peptides is possible), the compatibility of proIAPP seeds was sufficient in fostering the fibrillation process of IAPP. Insulin lacks this homology with the proIAPP sequence. Hence, proIAPP seeds were not as efficient in accelerating the insulin fibrillation process as observed for IAPP. Thus, at the beginning, the position and shape of the amide-I' band measured for insulin (ATR-FTIR) appeared to be rather similar to that observed when IAPP fibrils grew in the presence of proIAPP seeds (Figures 47 & 49), but upon drying on the crystal with time, the amide-I' band adopted a similar shape as observed for insulin fibrils formed in the absence of proIAPP (Figure 50).

Hence, proIAPP seeds are very efficient in enhancing the amyloidogenic propensity of IAPP and insulin, while IAPP and insulin seeds are not able to do the same for proIAPP. To verify these conclusions, further experiments are still needed to be performed with varying the percentage of insulin, IAPP and glucagon (a hormone secreted by α-cells of pancreas) seeds, in order to further explore the possibility of proIAPP involvement in amyloid plaque formation. This information will be of substantial importance for the understanding of the onset and progression of T2DM.

Chapter 4.   Summary

The aim of this PhD thesis was to understand and to explore the effects of negatively charged surfactants and membrane surfaces on the amyloidogenic propensity of proIAPP. In addition, the effects of seeds from different amyloidogenic peptides/proteins secreted by pancreatic β-cells on proIAPP fibrillation and *vice versa* were explored *in vitro*. This work should thus help in understanding the role of negatively charged cellular moieties and surfaces in the onset and progression of T2DM. Since the knowledge of the influence of lipid membranes on the amyloidogenic propensity of proIAPP has been quite rare, the first approach adopted was to investigate the putative effects of lipid membranes by taking a simple negatively charged membrane-mimicking model, SDS. Thereafter, this approach was extended to lipid monolayers in order to understand the insertion/adsorption of proIAPP at different surface pressures at a D_2O-lipid monolayer interface by IRRAS. This approach would help to understand the dynamics and conformation of the peptide bonds of proIAPP during the interaction with lipid monolayers resulting in amyloid fibril formation below and near the intracellular membrane's lateral pressure. The following part of the thesis dealt with the effects of lipid bilayer membranes possessing diverse anionic/zwitterionic lipid compositions on the amyloid fibril formation of proIAPP and proIAPP-IAPP mixtures. This helps in understanding the underlying mechanism of the role of lipid interfaces in proIAPP fibril formation, and subsequently the function of proIAPP and abnormally higher anionic cellular membrane contents in the onset and progression of T2DM. Finally, cross-seeding experiments with seeds from different amyloidogenic proteins/peptides, secreted by pancreatic β-cells, i.e. proIAPP, IAPP and insulin, were carried out in order to determine the compatibility of seeds from one amyloidogenic peptide with the others, thus helping identify the potent primary culprit of T2DM.

The role of a negatively charged membrane-mimicking agent as well as negatively charged cellular moieties on the early intracellular amyloid formation of proIAPP was studied using SDS. The SDS concentration had differential effects on the amyloidogenic propensity of proIAPP. SDS retains a monomeric structure below the CMC, whereas a gradual appearance of micelles starts near the CMC. ProIAPP, which did not show any amyloidogenic propensity in bulk solution, underwent fibril formation in a concentration range of 0.1 to 1.0 mM SDS, only. The monomeric structure of SDS interacts with proIAPP

and induces regular secondary structures in proIAPP. These partially folded proIAPP molecules fibrillate with relatively fast fibrillation rates. For SDS concentrations above the CMC, proIAPP molecules ceased to undergo fibril formation due to folding into stable α-helical conformations. The gain in the amyloidogenic propensity of proIAPP (for SDS concentrations < CMC) is probably rationalized by the screening of electrostatic repulsion between proIAPP molecules, in addition to the folding of proIAPP molecules into a partially folded amyloidogenic conformation, while the loss of the amyloidogenic propensity of proIAPP (for SDS concentrations > CMC) can be attributed to the binding of peptides to micelles that is expected to sterically hinder the close proximity needed for the self-assembly otherwise leading to fibril formation. Thus, it can be concluded that the aberrant folding of proIAPP into a partially folded conformation can lead to early intracellular amyloid fibril formation via interaction with negatively charged cellular moieties. Additionally, the folding of proIAPP into a stable conformation (α-helices) prohibits its involvement in early intracellular amyloid fibril formation, as suggested by the results in the presence of SDS at a concentration above the CMC value.

The SDS approach was followed by lipid monolayer studies in order to investigate the insertion/adsorption of proIAPP at different surface pressures at a D_2O-lipid interface by IRRAS and AFM. ProIAPP adsorption at the negatively charged lipid monolayer (POPG)-D_2O interface started immediately after the addition of lipid onto the subphase, as concluded from the increase in surface pressure. The adsorption of proIAPP onto the POPG-D_2O interface showed the induction of an α-helical structure in the proIAPP molecules. This adsorbed proIAPP underwent amyloid fibril formation as verified by AFM. However, no transition in the infrared wavenumbers from α-helix to β-sheet could be detected in the IRRA spectra. This could be explained by the diffusion of proIAPP molecules from the sample trough to the reference trough with an increase of the surface pressure > 24 mN/m, except for the mutant variant, which remained α-helical within the studied time frame. Thus, the conformational transitions found for proIAPP in the sample trough was subtracted from the conformational transitions in proIAPP which diffused into the reference trough. As a result, the amyloid fibril morphologies were found in both troughs by AFM analysis. Nevertheless, this approach helped in understanding the

conformational dynamics of proIAPP during amyloid fibril formation upon interaction with lipid monolayer membranes.

After observing the behaviour of proIAPP at negatively charged lipid monolayers at different lateral pressures, model bilayer membranes were studied. This part of the thesis was meant to understand the conformational transition during proIAPP fibrillation at various model membrane surfaces. In addition, to understand the conformational dynamics during proIAPP fibrillation, our goal was to reveal the putative mechanism of proIAPP aggregation in the presence of various model membrane systems, including heterogeneous model raft mixtures. ProIAPP adsorbs with a slow rate at the anionic membrane system used (DOPC:DOPG 7:3, w:w). This adsorption was subsequently followed by a gradual conformational transition from an unordered structure to intermolecular β-sheets. Thus, this observation is rationalized by factors like an increasing proIAPP concentration upon adsorption at the membrane surface and formation of a partially folded conformation, which helped to approximate proIAPP molecules for self-assembling into amyloid fibrils. This phenomenon was absent at lower concentrations of proIAPP. Additionally, this process did also not occur in the presence of a pure zwitterionic membrane (DOPC), a membrane with a lower anionic lipid content (< 30% DOPG) and a model raft mixture (DOPC:DPPC:Chol, 1:2:1). Unlike other amyloidogenic peptides/proteins, proIAPP (DOPC:DOPG, 7:3) forms oligomeric or short fibrillar structures only at anionic membranes. Additionally, the presence of proIAPP monomers in IAPP fibrillation reduced the fibrillation kinetics of IAPP at anionic membranes (DOPC:DOPG, 7:3). Hence, it seems likely that in the prediabetic stage, a remodulation of the cellular membrane's composition can be a leading/stimulating factor in the onset of intracellular nucleus formation, followed by the progression of extracellular deposits of amyloid plaques in T2DM patients.

Finally, the compatibility of seeds from different amyloidogenic peptides/proteins secreted by pancreatic β-cells, i.e., insulin, proIAPP, and IAPP, in the fibrillation reaction of other monomeric peptides/proteins secreted by the same cells was analyzed, since proIAPP and proinsulin are processed by the same processing enzymes, stored in the same secretory granules and secreted in response to the same stimuli. Fluorescence and ATR-FTIR spectroscopy, as well as AFM, showed that IAPP and insulin seeds were unable to induce amyloid structures in proIAPP. However, seeds from proIAPP were able to enhance

the amyloidogenic propensity of IAPP and insulin, by reducing the nucleation (lag) phase. The presence or absence of proIAPP seeds did not have a significant effect on the amide-I' band of the fibrils obtained from IAPP and insulin. However, the morphology of the IAPP fibrils was drastically affected by the addition of proIAPP seeds to the fibrillation reaction. IAPP formed only oligomers in the presence of seeds from proIAPP, instead of the mature fibrils that are found in the absence of proIAPP seeds. ProIAPP has a minor effect on the fibrillar morphology of insulin, compared to the unseeded fibrillation, and exhibits predominantly fragmented fibrils along with some longer fibrils. The formation of the IAPP oligomers may be attributed to the incorporation of proIAPP molecules with the growing IAPP aggregates during the aggregation reaction, and the extended positively charged N- and C- termini of the incorporated proIAPP probably sterically hinder the elongation of oligomers into mature fibrils. Thus, the seeds from proIAPP are able to enhance the amyloidogenic propensity of IAPP and insulin, but not *vice versa*.

To conclude, a simple hypothesis may be postulated:

"An increase in the cellular composition of anionic moieties or interfaces in the prediabetic stage of T2DM may lead to the formation of intracellular proIAPP oligomers or short fibrils, which upon exposure to IAPP and insulin monomers may progress to pathological amyloid plaque formation in T2DM".

Chapter 5.   Zusammenfassung

Ziel der vorliegenden Dissertation war die Untersuchung des Einflusses negativ geladener, grenzflächenaktiver Substanzen und Oberflächen auf die amyloidogenen Eigenschaften von proIAPP. Des Weiteren wurde der Effekt von Fibrillenkeimen (*engl.* seeds) unterschiedlicher amyloidogener Peptide/Proteine, die von pankreatischen β-Zellen sekretiert werden, auf die Fibrillierung von proIAPP *in vitro* analysiert. Diese Ergebnisse tragen zu einem besseren Verständnis der Funktion von negativ geladenen zellulären Komponenten und Oberflächen während des Ausbruchs und Verlaufs von T2DM bei. Da der Einfluss von Lipidmembranen auf die amyloidogenen Eigenschaften von proIAPP noch weitgehend unbekannt ist, wurden zunächst mögliche Effekte durch die Verwendung von SDS untersucht, welches ein einfaches, negativ geladenes, membrannachahmendes Modellsystem darstellt. Im Folgenden wurde dieser Ansatz auf Lipidmonoschichten ausgeweitet, um mit Hilfe der IRRA-Spektroskopie einen Einblick in die Einlagerung bzw. Adsoption von proIAPP bei unterschiedlichen Oberflächendrücken in bzw. an der D_2O – Lipidmonoschicht-Grenzfläche zu erhalten. Diese Methodik erlaubt eine genauere Kenntnis der Peptidbindungsdynamik des proIAPPs während der Wechselwirkung mit Lipidmonoschichten unterhalb und nahe dem in intrazellulären Membranen vorherrschenden lateralen Druck, wobei die Interaktion zur Amyloidfibrillenbildung führt. Ein weiterer Teil dieser Dissertation beschäftigte sich mit dem Einfluss von Lipiddoppelschichtmembranen mit unterschiedlichen Anteilen an anionischen und zwitterionischen Lipiden auf die Amyloidfibrillenbildung von proIAPP sowie Mischungen von proIAPP mit IAPP. Diese Ergebnisse helfen, den Mechanismus der proIAPP-Fibrillierung in Anwesenheit von Membranen und die Anwesenheit von hohen anionischen Lipidanteilen zellulärer Membranen während der Ausbildung und des Verlaufes von T2DM besser zu verstehen. Abschließend wurden Kreuzwechselwirkungsexperimente mit Fibrillenkeimen von unterschiedlichen amyloidogenen Peptiden/Proteinen, die von pankreatischen β-Zellen sekretiert werden (wie z.B. proIAPP, IAPP und Insulin), durchgeführt, um die Kompatibilität von Fibrillenkeimen eines amyloidogenen Peptides zu einem anderen zu untersuchen. Dies soll die primär wirksame Spezies von T2DM identifizieren helfen.

Die Experimente mit der negativ geladenen, membrannachahmenden Substanz SDS zeigen in Abhängigkeit der SDS-Konzentration unterschiedliche Effekte auf die Neigung des proIAPPs zur Amyloidbildung, da SDS unterhalb der kritischen Mizellkonzentration (CMC) seine monomere Struktur beibehält, während nahe der CMC eine sukzessive Ausbildung von Mizellstrukturen erfolgt. In Bulk-Lösung wies proIAPP kein amyloidogenes Verhalten auf, es bildete jedoch bei SDS-Konzentration zwischen 0,1 und 1 mM Fibrillen aus. Dabei wechselwirkt die monomere Konformation von SDS mit proIAPP und induziert reguläre Sekundärstrukturen. Diese partiell gefalteten proIAPP-Moleküle fibrillieren mit vergleichsweise schnelleren Fibrillierungsgeschwindigkeiten. Liegt die SDS-Konzentration oberhalb der CMC, bildet proIAPP stabile α-helikale Konformationen aus und umgeht so die Fibrillenbildung. Die verstärkte Neigung von proIAPP zur Amyloidbildung bei SDS-Konzentrationen unterhalb der CMC basiert wahrscheinlich auf der Abschirmung der elektrostatischen Abstoßungskräfte zwischen den proIAPP-Molekülen, zusätzlich zur Faltung der pro-IAPP-Moleküle in teilweise gefaltete amyloidogene Strukturen. Im Gegensatz dazu lässt sich die Herabsetzung der amyloid-bildenden Eigenschaften des pro-IAPPs bei SDS-Konzentrationen oberhalb der CMC auf die Bindung des Peptids an die Mizellen zurückführen, wobei von einer sterischen Hinderung der für die Selbstassoziation benötigten unmittelbaren Nähe ausgegangen wird, die ansonsten zu einer fibrillären Morphologie führen würde. Demzufolge kann zweifelsfrei angenommen werden, dass die anomale Faltung des proIAPPs in eine partiell gefaltete Konformation zu einer frühen intrazellulären Amyloidfibrillenbildung aufgrund von Wechselwirkungen mit negativ geladenen zellulären Komponenten führt. Weiterhin verhindert die Faltung des proIAPPs in eine stabile (α-helikale) Konformation die Ausbildung früher intrazellulärer Amyloidfibrillen, wie die Ergebnisse in Anwesenheit von SDS bei Konzentrationen oberhalb der CMC nahe legen.

Die folgenden Studien mit Lipidmonoschichten erlauben Aussagen über die Einlagerung bzw. Adsorption von proIAPP an der D_2O-Lipidgrenzfläche bei verschiedenen Oberflächendrücken. Dabei konnte mittels IRRAS gezeigt werden, dass die Adsorption von proIAPP an der negativ geladenen Lipidmonoschicht (POPG)-D_2O-Grenzfläche sofort nach Spreitung des Lipids auf der Subphase erfolgt, was durch einen Anstieg des Oberflächendrucks nachgewiesen wurde. Die Adsorption führt zur Ausbildung α-helikaler

Strukturen der proIAPP-Moleküle. Diese adsorbierte Form unterliegt der Fibrillenbildung, welche mittels AFM nachgewiesen wurde, obwohl in den IRRA-Spektren keine Verschiebung der Wellenzahl von α-Helix zu β-Faltblatt beobachtet werden konnte. Letzteres lässt sich durch die Diffusion von proIAPP vom Probentrog in den Referenztrog mit steigendem Oberflächendruck (> 24 mN/m) begründen. Allerdings behielt die mutierte Spezies über den beobachteten Zeitraum ihre α-helikale Struktur bei. Folglich wurde die im Probentrog beobachtete Konformationsänderung des proIAPPs um die im Referenztrog ermittelte korrigiert. Daraus ergab sich der Nachweis einer amyloidogenen Fibrillenmorphologie in beiden Trögen mit Hilfe der Rasterkraftmikroskopie. Trotzdem konnte mit Hilfe dieses Ansatzes die Konformationsdynamik des proIAPPs während der durch Lipidmonoschichten induzierten Amyloidfibrillenbildung besser verstanden werden.

Nachdem die Eigenschaften von proIAPP in Gegenwart von negativ geladenen Lipidmonoschichten bei unterschiedlichen Oberflächendrücken analysiert wurden, erfolgte nun die Betrachtung von Modellsystemen, die sich aus Lipiddoppelschichten zusammensetzen. Dieser Teil der Dissertation diente dazu, den Strukturwechsel des proIAPPs während der Fibrillierung an verschiedenen Modellmembranoberflächen näher zu untersuchen. Des Weiteren sollte ein möglicher Mechanismus der Aggregation von proIAPP in Gegenwart verschiedener Modellmembransysteme aufgezeigt werden, inklusive heterogener Modellraftmembranen. Dabei zeigte sich, dass proIAPP an anionischen Membransystemen (DOPC:DOPG 7:3, w/w) langsam adsorbiert, wobei sich der Adsorption eine schrittweise Konformationsänderung von ungeordneten zu intermolekularen β-Faltblattstrukturen anschließt. Diese Beobachtungen lassen sich mit einem Anstieg der proIAPP-Konzentration an der Membranoberfläche während der Adsorption sowie der Ausbildung von partiell gefalteten Strukturen erklären, wobei die daraus resultierende große Nähe der proIAPP-Moleküle zueinander eine Selbstassoziation zu Amyloidfibrillen erleichtert. Dieses Phänomen konnte nicht bei geringeren proIAPP-Konzentrationen nachgewiesen werden und war auch in Anwesenheit einer reinen zwitterionischen Membran (DOPC) sowie einer Membran mit geringem anionischen Lipidanteil (< 30% DOPG) und einer Modellraftmembran (DOPC:DPPC:Chol, 1:2:1) nicht detektierbar. Im Gegensatz zu anderen amyloidogenen Peptiden/Proteinen bildete proIAPP an anionischen Membranen (DOPC:DOPG, 7:3) lediglich oligomere und kurze fibrilläre

Strukturen aus. Des Weiteren führte die Anwesenheit von proIAPP-Monomeren während der Fibrillenbildung von IAPP an anionischen Membranen (DOPC:DOPG, 7:3) zu einer verlangsamten Fibrillierungskinetik des IAPPs. Folglich scheint im prädiabetischen Stadium die Anpassung der zellulären Membranzusammensetzung ein ausschlaggebender Faktor zu Beginn der intrazellulären Keimbildung zu sein, in deren weiterem Verlauf extrazelluläre Ablagerungen amyloidogener Plaques bei Patienten mit T2DM auftreten.

Abschließend erfolgte in dieser Arbeit eine Analyse der gegenseitigen Austauschbarkeit von Fibrillenkeimen verschiedener amyloidogener Peptide/Proteine, wie z.B. proIAPP, Insulin und IAPP, während der Fibrillierung anderer monomerer Peptide/Proteine, die von den gleichen pankreatischen β-Zellen sekretiert werden, da proIAPP und Proinsulin von den gleichen Enzymen prozessiert und in den gleichen sekretorischen Granula gespeichert werden sowie der Auslöseimpuls zur Sekretion derselbe ist. Mit Hilfe der Fluoreszenz- und ATR-FTIR-Spektroskopie sowie der Rasterkraftmikroskopie konnte gezeigt werden, dass Fibrillenkeime von IAPP und Insulin keine Ausbildung amyloidogener Strukturen beim proIAPP induzieren können. Allerdings war umgekehrt eine Verstärkung der Neigung zur Amyloidbildung bei IAPP und Insulin durch proIAPP-Fibrillenkeime mittels einer verkürzten Keimbildungsphase nachweisbar. Die An- oder Abwesenheit von proIAPP-Fibrillenkeimen hatte dabei keinen signifikanten Einfluss auf die Amid-I′-Bande der IAPP- bzw. Insulinfibrillen. Indes wurde die Morphologie der IAPP-Fibrillen drastisch durch die Anwesenheit der proIAPP-Fibrillenkeime während der Aggregation beeinflusst. Anstelle gereifter Fibrillen bildete IAPP in Anwesenheit von proIAPP-Fibrillenkeimen lediglich Oligomere. Dagegen wurde die Morphologie der Insulinaggregate im Vergleich zur Aggregation ohne Keimzugabe nur geringfügig durch die proIAPP-Fibrillenkeime beeinflusst. Insulin wies neben einigen längeren Fibrillen hauptsächlich fragmentierte Fibrillen auf. Die Morphologie der IAPP-Oligomere lässt sich auf die Einlagerung von proIAPP-Molekülen in die IAPP-Aggregate während der Aggregation zurückführen. Aufgrund der ausgedehnten positiv geladenen N- und C-Termini des eingelagerten proIAPPs tritt eine sterische Hinderung beim Anwachsen der Oligomere zu gereiften Fibrillen auf. Folglich sind Fibrillenkeime vom proIAPP stärker kompatibel und steigern die Amyloidogenität von IAPP und Insulin, während der umgekehrte Vorgang nicht zu beobachten ist.

Auf Grundlage der Ergebnisse der vorliegenden Dissertation lässt sich zusammenfassend folgende Hypothese aufstellen:

"Eine Erhöhung der zellulären Zusammensetzung mit anionischen Komponenten und Oberflächen im prädiabetischen Stadium der T2DM scheint zur Ausbildung von intrazellulären proIAPP-Oligomeren oder kurzen Fibrillen zu führen, was im weiteren Verlauf durch die Wechselwirkung mit IAPP- und Insulinmonomeren zu einer Ablagerung pathologischer Amyloidplaques führen kann".

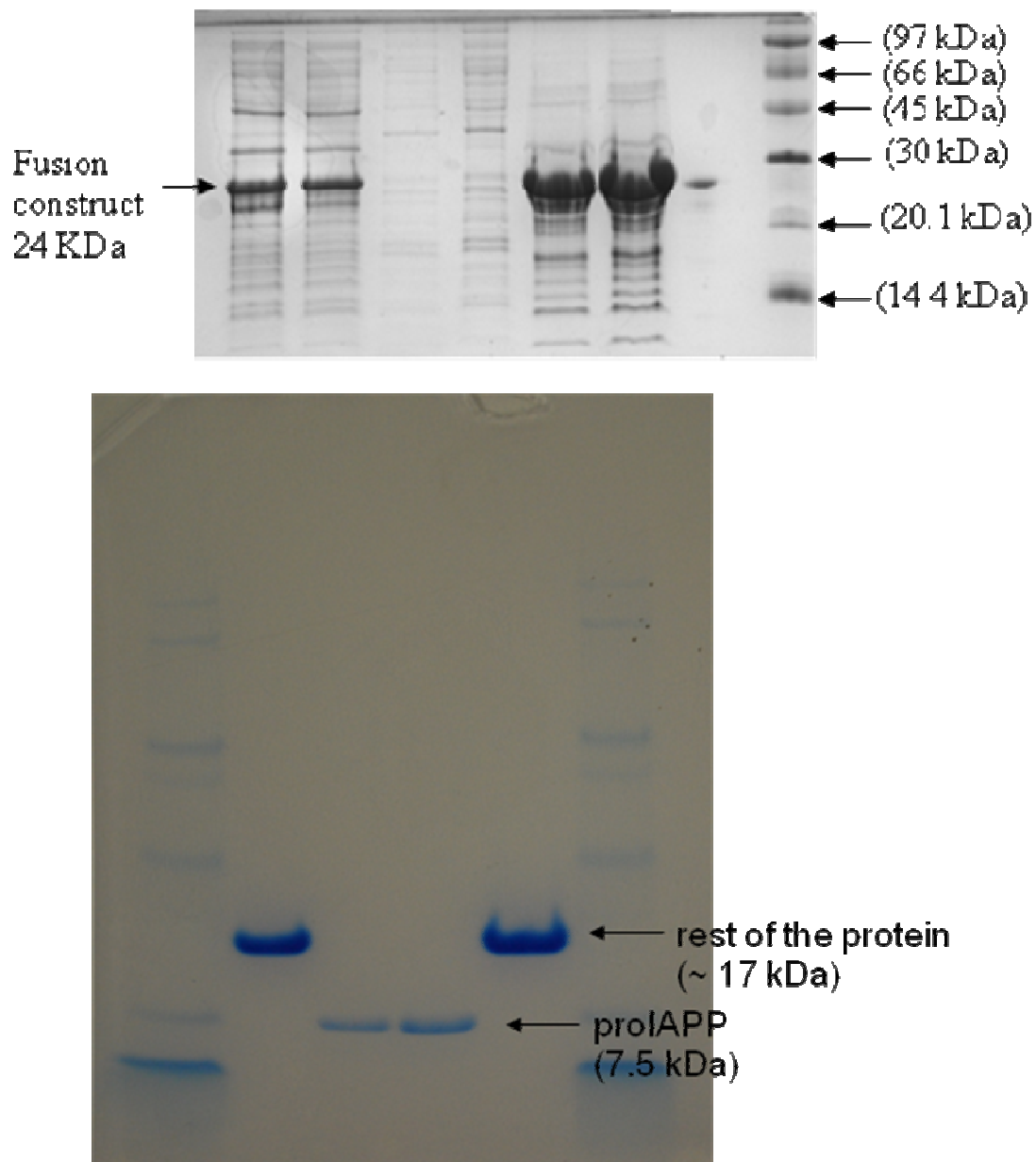**Figure A**: Upper panel: BL21(DE3) *E. coli* cells expression for induced proIAPP production, from right: lanes 1 & 2 - cytosol; lanes 3 & 4 - eluate as cytosol passed through Ni-NTA beads; lanes 5 & 6 - on Ni beads; lane 8 - marker. Lower panel: After cleavage of fusion protein with enterokinase enzyme, lane 3 and 4 shows proIAPP; lanes 2 & 5 shows the rest of the cleaved part of fusion protein.

Figure B: Electron spray ionization mass spectroscopy data to identify the purity and mass of the purified peptide (fusion proIAPP). The graph shows the mass by charge ratio (m/z) vs. the relative abundance of the species; the inset shows the mass of the species present in the sample.
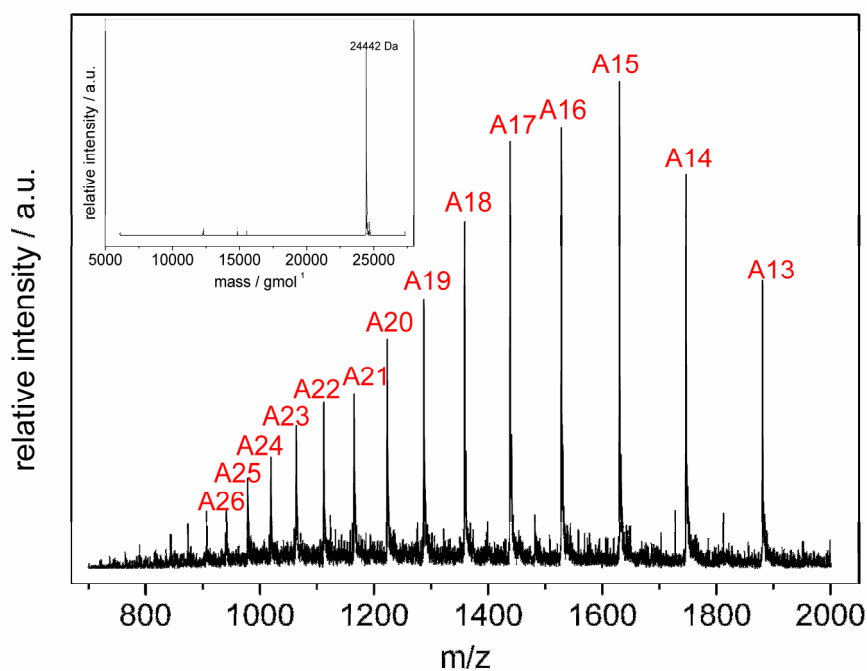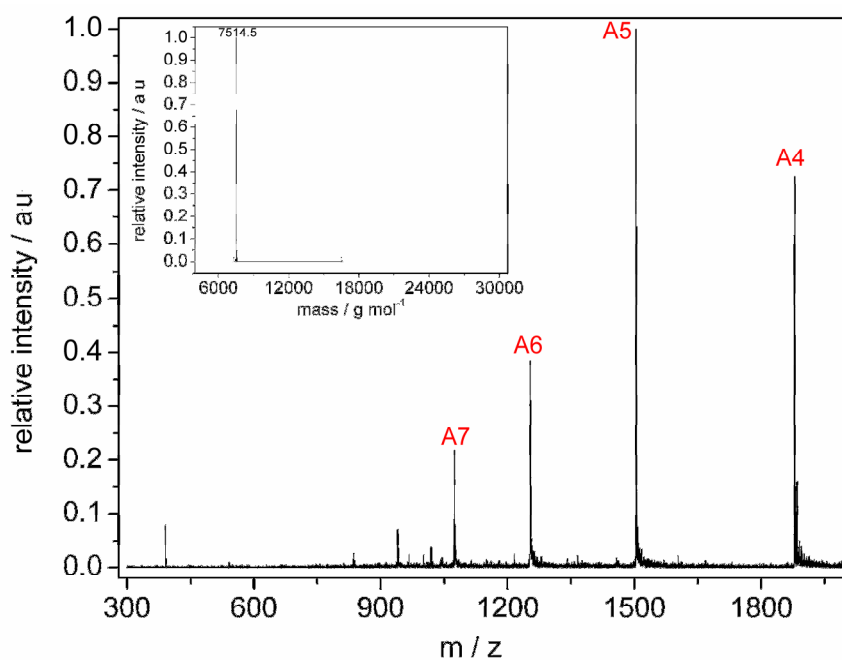

Figure C: Electron spray ionization mass spectroscopy data to identify the purity and mass of the purified peptide (proIAPP). The graph shows the mass by charge ratio (m/z) vs. the relative abundance of the species; the inset shows the mass of the species present in the sample.

100
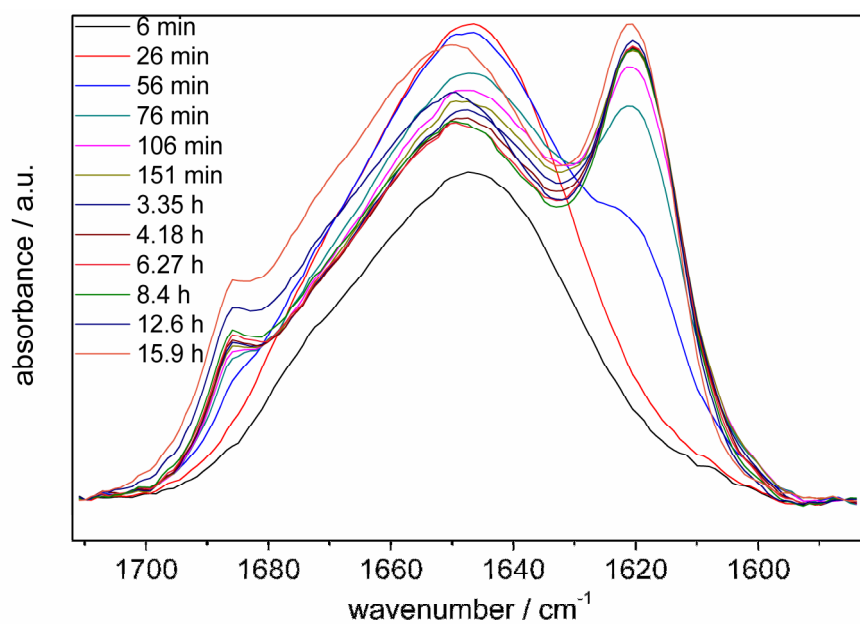
Figure D: 20 µM proIAPP aggregation on a silicon crystal in the presence of 0.1 mM SDS in 10 mM phosphate buffer, pD 7.4, at room temperature. The time evolution of the amide-I' band shows the appearance of antiparallel β-sheets and helical conformations during the process of aggregation on the silicon crystal.
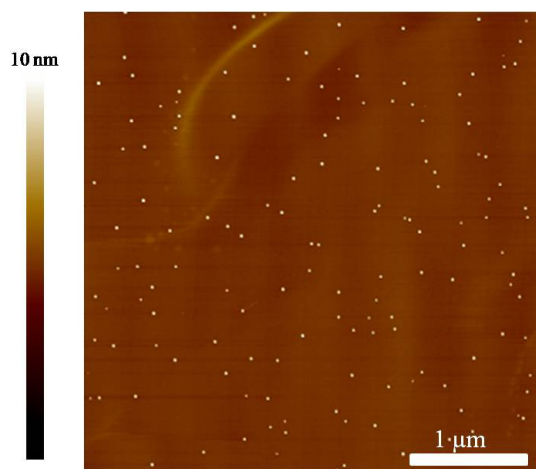
Figure E: AFM image of proIAPP oligomers grown in the presence of 0.1 mM SDS that were used as seeds for enhancing the fibrillation kinetics of IAPP and insulin at their respective amyloidogenic conditions.

References

(1)   Powers, E. T., Morimoto, R. I., Dillin, A., Kelly, J. W., and Balch, W. E. (2009) Biological and chemical approaches to diseases of proteostasis deficiency. *Annu Rev Biochem 78*, 959-91.

(2)   Chiti, F., and Dobson, C. M. (2006) Protein misfolding, functional amyloid, and human disease. *Annu Rev Biochem 75*, 333-66.

(3)   Amos, A. F., McCarty, D. J., and Zimmet, P. (1997) The rising global burden of diabetes and its complications: estimates and projections to the year 2010. *Diabet Med 14 Suppl 5*, S1-85.

(4)   Kahn, S. E., Andrikopoulos, S., and Verchere, C. B. (1999) Islet amyloid: a long-recognized but underappreciated pathological feature of type 2 diabetes. *Diabetes 48*, 241-53.

(5)   Hull, R. L., Westermark, G. T., Westermark, P., and Kahn, S. E. (2004) Islet amyloid: a critical entity in the pathogenesis of type 2 diabetes. *J Clin Endocrinol Metab 89*, 3629-43.

(6)   Westermark, G. T., Steiner, D. F., Gebre-Medhin, S., Engstrom, U., and Westermark, P. (2000) Pro islet amyloid polypeptide (ProIAPP) immunoreactivity in the islets of Langerhans. *Ups J Med Sci 105*, 97-106.

(7)   Clark, A., and Nilsson, M. R. (2004) Islet amyloid: a complication of islet dysfunction or an aetiological factor in Type 2 diabetes? *Diabetologia 47*, 157-69.

(8)   Kahn, S. E., D'Alessio, D. A., Schwartz, M. W., Fujimoto, W. Y., Ensinck, J. W., Taborsky, G. J., Jr., and Porte, D., Jr. (1990) Evidence of cosecretion of islet amyloid polypeptide and insulin by beta-cells. *Diabetes 39*, 634-8.

(9)   Marcinkiewicz, M., Ramla, D., Seidah, N. G., and Chretien, M. (1994) Developmental expression of the prohormone convertases PC1 and PC2 in mouse pancreatic islets. *Endocrinology 135*, 1651-60.

(10)   Marzban, L., Trigo-Gonzalez, G., Zhu, X., Rhodes, C. J., Halban, P. A., Steiner, D. F., and Verchere, C. B. (2004) Role of beta-cell prohormone convertase (PC)1/3 in processing of pro-islet amyloid polypeptide. *Diabetes 53*, 141-8.

(11)   Sanke, T., Bell, G. I., Sample, C., Rubenstein, A. H., and Steiner, D. F. (1988) An islet amyloid peptide is derived from an 89-amino acid precursor by proteolytic processing. *J Biol Chem 263*, 17243-6.

(12)   Roberts, A. N., Leighton, B., Todd, J. A., Cockburn, D., Schofield, P. N., Sutton, R., Holt, S., Boyd, Y., Day, A. J., Foot, E. A., and et al. (1989) Molecular and functional characterization of amylin, a peptide associated with type 2 diabetes mellitus. *Proc Natl Acad Sci U S A 86*, 9662-6.

(13)   Kahn, S. E., Verchere, C. B., Andrikopoulos, S., Asberry, P. J., Leonetti, D. L., Wahl, P. W., Boyko, E. J., Schwartz, R. S., Newell-Morris, L., and Fujimoto, W. Y. (1998) Reduced amylin release is a characteristic of impaired glucose tolerance and type 2 diabetes in Japanese Americans. *Diabetes 47*, 640-5.

(14)   Clark, A., Cooper, G. J., Lewis, C. E., Morris, J. F., Willis, A. C., Reid, K. B., and Turner, R. C. (1987) Islet amyloid formed from diabetes-associated peptide may be pathogenic in type-2 diabetes. *Lancet 2*, 231-4.

(15)   Cooper, G. J., Willis, A. C., Clark, A., Turner, R. C., Sim, R. B., and Reid, K. B. (1987) Purification and characterization of a peptide from amyloid-rich pancreases of type 2 diabetic patients. *Proc Natl Acad Sci U S A 84*, 8628-32.

(16)   Gebre-Medhin, S., Olofsson, C., and Mulder, H. (2000) Islet amyloid polypeptide in the islets of Langerhans: friend or foe? *Diabetologia 43*, 687-95.

(17)   Yonemoto, I. T., Kroon, G. J., Dyson, H. J., Balch, W. E., and Kelly, J. W. (2008) Amylin proprotein processing generates progressively more amyloidogenic peptides that initially sample the helical state. *Biochemistry 47*, 9900-10.

(18)   Jha, S., Sellin, D., Seidel, R., and Winter, R. (2009) Amyloidogenic propensities and conformational properties of ProIAPP and IAPP in the presence of lipid bilayer membranes. *J Mol Biol 389*, 907-20.

(19)   Westermark, G., Westermark, P., Eizirik, D. L., Hellerstrom, C., Fox, N., Steiner, D. F., and Andersson, A. (1999) Differences in amyloid deposition in islets of transgenic mice expressing human islet amyloid polypeptide versus human islets implanted into nude mice. *Metabolism 48*, 448-54.

(20)   Paulsson, J. F., Andersson, A., Westermark, P., and Westermark, G. T. (2006) Intracellular amyloid-like deposits contain unprocessed pro-islet amyloid polypeptide

(proIAPP) in beta cells of transgenic mice overexpressing the gene for human IAPP and transplanted human islets. *Diabetologia 49*, 1237-46.

(21) Park, K., and Verchere, C. B. (2001) Identification of a heparin binding domain in the N-terminal cleavage site of pro-islet amyloid polypeptide. Implications for islet amyloid formation. *J Biol Chem 276*, 16611-6.

(22) Lopes, D. H., Meister, A., Gohlke, A., Hauser, A., Blume, A., and Winter, R. (2007) Mechanism of islet amyloid polypeptide fibrillation at lipid interfaces studied by infrared reflection absorption spectroscopy. *Biophys J 93*, 3132-41.

(23) Engel, M. F., Yigittop, H., Elgersma, R. C., Rijkers, D. T., Liskamp, R. M., de Kruijff, B., Hoppener, J. W., and Antoinette Killian, J. (2006) Islet amyloid polypeptide inserts into phospholipid monolayers as monomer. *J Mol Biol 356*, 783-9.

(24) Engel, M. F., Khemtemourian, L., Kleijer, C. C., Meeldijk, H. J., Jacobs, J., Verkleij, A. J., de Kruijff, B., Killian, J. A., and Hoppener, J. W. (2008) Membrane damage by human islet amyloid polypeptide through fibril growth at the membrane. *Proc Natl Acad Sci U S A 105*, 6033-8.

(25) Engel, M. F. (2009) Membrane permeabilization by Islet Amyloid Polypeptide. *Chem Phys Lipids 160*, 1-10.

(26) Glenner, G. G., Ein, D., Eanes, E. D., Bladen, H. A., Terry, W., and Page, D. L. (1971) Creation of "amyloid" fibrils from Bence Jones proteins in vitro. *Science 174*, 712-4.

(27) Rambaran, R. N., and Serpell, L. C. (2008) Amyloid fibrils: abnormal protein assembly. *Prion 2*, 112-7.

(28) Grudzielanek, S., Smirnovas, V., and Winter, R. (2006) Solvation-assisted pressure tuning of insulin fibrillation: from novel aggregation pathways to biotechnological applications. *J Mol Biol 356*, 497-509.

(29) Bemporad, F., Taddei, N., Stefani, M., and Chiti, F. (2006) Assessing the role of aromatic residues in the amyloid aggregation of human muscle acylphosphatase. *Protein Sci 15*, 862-70.

(30) Dobson, C. M. (2003) Protein folding and misfolding. *Nature 426*, 884-90.

(31) Sunde, M., Serpell, L. C., Bartlam, M., Fraser, P. E., Pepys, M. B., and Blake, C. C. (1997) Common core structure of amyloid fibrils by synchrotron X-ray diffraction. *J Mol Biol 273*, 729-39.

(32) Madine, J., Jack, E., Stockley, P. G., Radford, S. E., Serpell, L. C., and Middleton, D. A. (2008) Structural insights into the polymorphism of amyloid-like fibrils formed by region 20-29 of amylin revealed by solid-state NMR and X-ray fiber diffraction. *J Am Chem Soc 130*, 14990-5001.

(33) Perutz, M. F., Johnson, T., Suzuki, M., and Finch, J. T. (1994) Glutamine repeats as polar zippers: their possible role in inherited neurodegenerative diseases. *Proc Natl Acad Sci U S A 91*, 5355-8.

(34) Perutz, M. (1994) Polar zippers: their role in human disease. *Protein Sci 3*, 1629-37.

(35) Staniforth, R. A., Giannini, S., Higgins, L. D., Conroy, M. J., Hounslow, A. M., Jerala, R., Craven, C. J., and Waltho, J. P. (2001) Three-dimensional domain swapping in the folded and molten-globule states of cystatins, an amyloid-forming structural superfamily. *Embo J 20*, 4774-81.

(36) Schlunegger, M. P., Bennett, M. J., and Eisenberg, D. (1997) Oligomer formation by 3D domain swapping: a model for protein assembly and misassembly. *Adv Protein Chem 50*, 61-122.

(37) Chothia, C. (1973) Conformation of twisted beta-pleated sheets in proteins. *J Mol Biol 75*, 295-302.

(38) Pauling, L., and Corey, R. B. (1951) Configurations of Polypeptide Chains With Favored Orientations Around Single Bonds: Two New Pleated Sheets. *Proc Natl Acad Sci U S A 37*, 729-40.

(39) Goldsbury, C., Kistler, J., Aebi, U., Arvinte, T., and Cooper, G. J. (1999) Watching amyloid fibrils grow by time-lapse atomic force microscopy. *J Mol Biol 285*, 33-9.

(40) Makin, O. S., Atkins, E., Sikorski, P., Johansson, J., and Serpell, L. C. (2005) Molecular basis for amyloid fibril formation and stability. *Proc Natl Acad Sci U S A 102*, 315-20.

(41) Perrin, R. J., Woods, W. S., Clayton, D. F., and George, J. M. (2000) Interaction of human alpha-Synuclein and Parkinson's disease variants with phospholipids. Structural analysis using site-directed mutagenesis. *J Biol Chem 275*, 34393-8.

(42)   Olofsson, A., Borowik, T., Grobner, G., and Sauer-Eriksson, A. E. (2007) Negatively charged phospholipid membranes induce amyloid formation of medin via an alpha-helical intermediate. *J Mol Biol 374*, 186-94.

(43)   Ellis, R. J., and Minton, A. P. (2006) Protein aggregation in crowded environments. *Biol Chem 387*, 485-97.

(44)   Homouz, D., Perham, M., Samiotakis, A., Cheung, M. S., and Wittung-Stafshede, P. (2008) Crowded, cell-like environment induces shape changes in aspherical protein. *Proc Natl Acad Sci U S A 105*, 11754-9.

(45)   Munishkina, L. A., Cooper, E. M., Uversky, V. N., and Fink, A. L. (2004) The effect of macromolecular crowding on protein aggregation and amyloid fibril formation. *J Mol Recognit 17*, 456-64.

(46)   Aisenbrey, C., Borowik, T., Bystrom, R., Bokvist, M., Lindstrom, F., Misiak, H., Sani, M. A., and Grobner, G. (2008) How is protein aggregation in amyloidogenic diseases modulated by biological membranes? *Eur Biophys J 37*, 247-55.

(47)   Aisenbrey, C., Bechinger, B., and Grobner, G. (2008) Macromolecular crowding at membrane interfaces: adsorption and alignment of membrane peptides. *J Mol Biol 375*, 376-85.

(48)   Porat, Y., Kolusheva, S., Jelinek, R., and Gazit, E. (2003) The human islet amyloid polypeptide forms transient membrane-active prefibrillar assemblies. *Biochemistry 42*, 10971-7.

(49)   Green, J. D., Kreplak, L., Goldsbury, C., Li Blatter, X., Stolz, M., Cooper, G. S., Seelig, A., Kistler, J., and Aebi, U. (2004) Atomic force microscopy reveals defects within mica supported lipid bilayers induced by the amyloidogenic human amylin peptide. *J Mol Biol 342*, 877-87.

(50)   Rangachari, V., Moore, B. D., Reed, D. K., Sonoda, L. K., Bridges, A. W., Conboy, E., Hartigan, D., and Rosenberry, T. L. (2007) Amyloid-beta(1-42) rapidly forms protofibrils and oligomers by distinct pathways in low concentrations of sodium dodecylsulfate. *Biochemistry 46*, 12451-62.

(51)   Knight, J. D., and Miranker, A. D. (2004) Phospholipid catalysis of diabetic amyloid assembly. *J Mol Biol 341*, 1175-87.

(52) Maltseva, E., Kerth, A., Blume, A., Mohwald, H., and Brezesinski, G. (2005) Adsorption of amyloid beta (1-40) peptide at phospholipid monolayers. *Chembiochem 6*, 1817-24.

(53) Bokvist, M., Lindstrom, F., Watts, A., and Grobner, G. (2004) Two types of Alzheimer's beta-amyloid (1-40) peptide membrane interactions: aggregation preventing transmembrane anchoring versus accelerated surface fibril formation. *J Mol Biol 335*, 1039-49.

(54) Bokvist, M., and Grobner, G. (2007) Misfolding of amyloidogenic proteins at membrane surfaces: the impact of macromolecular crowding. *J Am Chem Soc 129*, 14848-9.

(55) Bystrom, R., Aisenbrey, C., Borowik, T., Bokvist, M., Lindstrom, F., Sani, M. A., Olofsson, A., and Grobner, G. (2008) Disordered proteins: biological membranes as two-dimensional aggregation matrices. *Cell Biochem Biophys 52*, 175-89.

(56) Jarrett, J. T., and Lansbury, P. T., Jr. (1993) Seeding "one-dimensional crystallization" of amyloid: a pathogenic mechanism in Alzheimer's disease and scrapie? *Cell 73*, 1055-8.

(57) Dzwolak, W. (2006) Tuning amyloidogenic conformations through cosolvents and hydrostatic pressure: when the soft matter becomes even softer. *Biochim Biophys Acta 1764*, 470-80.

(58) Hong, D. P., and Fink, A. L. (2005) Independent heterologous fibrillation of insulin and its B-chain peptide. *Biochemistry 44*, 16701-9.

(59) Furukawa, Y., Kaneko, K., Matsumoto, G., Kurosawa, M., and Nukina, N. (2009) Cross-seeding fibrillation of Q/N-rich proteins offers new pathomechanism of polyglutamine diseases. *J Neurosci 29*, 5153-62.

(60) Day, C. A., and Kenworthy, A. K. (2009) Tracking microdomain dynamics in cell membranes. *Biochim Biophys Acta 1788*, 245-53.

(61) Shaw, A. S. (2006) Lipid rafts: now you see them, now you don't. *Nat Immunol 7*, 1139-42.

(62) Abedini, A., Tracz, S. M., Cho, J. H., and Raleigh, D. P. (2006) Characterization of the heparin binding site in the N-terminus of human pro-islet amyloid polypeptide: implications for amyloid formation. *Biochemistry 45*, 9228-37.

(63)   Nielsen, L., Frokjaer, S., Brange, J., Uversky, V. N., and Fink, A. L. (2001) Probing the mechanism of insulin fibril formation with insulin mutants. *Biochemistry 40*, 8397-409.

(64)   Pace, C. N., Vajdos, F., Fee, L., Grimsley, G., and Gray, T. (1995) How to measure and predict the molar absorption coefficient of a protein. *Protein Sci 4*, 2411-23.

(65)   Zhang, Z., and Marshall, A. G. (1998) A universal algorithm for fast and automated charge state deconvolution of electrospray mass-to-charge ratio spectra. *J Am Soc Mass Spectrom 9*, 225-33.

(66)   Royer, C. A. (2006) Probing protein folding and conformational transitions with fluorescence. *Chem Rev 106*, 1769-84.

(67)   Lakowicz, J. *Principles of Fluorescence spectroscopy*, second ed.

(68)   Vassar, P. S., and Culling, C. F. (1959) Fluorescent stains, with special reference to amyloid and connective tissues. *Arch Pathol 68*, 487-98.

(69)   Naiki, H., Higuchi, K., Hosokawa, M., and Takeda, T. (1989) Fluorometric determination of amyloid fibrils in vitro using the fluorescent dye, thioflavin T1. *Anal Biochem 177*, 244-9.

(70)   LeVine, H., 3rd. (1993) Thioflavine T interaction with synthetic Alzheimer's disease beta-amyloid peptides: detection of amyloid aggregation in solution. *Protein Sci 2*, 404-10.

(71)   LeVine, H., 3rd. (1995) Thioflavin T interaction with amyloid β-sheet structures. *Amyloid Int. J. Exp. Clin. Invest. 2*, 1-6.

(72)   Saeed, S. M., and Fine, G. (1967) Thioflavin-T for amyloid detection. *Am J Clin Pathol 47*, 588-93.

(73)   Andersen, C. B., Yagi, H., Manno, M., Martorana, V., Ban, T., Christiansen, G., Otzen, D. E., Goto, Y., and Rischel, C. (2009) Branching in amyloid fibril growth. *Biophys J 96*, 1529-36.

(74)   Ban, T., Hamada, D., Hasegawa, K., Naiki, H., and Goto, Y. (2003) Direct observation of amyloid fibril growth monitored by thioflavin T fluorescence. *J Biol Chem 278*, 16462-5.

(75)   Kelenyi, G. (1967) On the histochemistry of azo group-free thiazole dyes. *J Histochem Cytochem 15*, 172-80.

(76) Wu, J., Yang, J. T., and Wu, C. S. (1992) Beta-II conformation of all-beta proteins can be distinguished from unordered form by circular dichroism. *Anal Biochem 200*, 359-64.

(77) Manavaln, P., and Johnson, W. C. Jr. (1983) Sensitivity of circular dichroism to protein tertiary structure class. *Nature 305*, 831-832.

(78) Bohm, G., Muhr, R., and Jaenicke, R. (1992) Quantitative analysis of protein far UV circular dichroism spectra by neural networks. *Protein Eng 5*, 191-5.

(79) Rummelhart, D. E., Hinton, G. E., and Williams, R. J. (1986) Learning representation by backpropagation algorithms. *Nature (London) 323*, 533-536.

(80) Blaudez, D., Buffeteau, T., Castaings, N., Desbat, B., Turlet, J. M. (1996) Organization in pure and alternate deuterated cadmium arachidate monolayers on solid substrates and at the air/water interface studied by conventional and differential Fourier transform infrared spectroscopies. *J. Chem. Phys. 104*, 9983-9993.

(81) Meister, A., Nicolini, C., Waldmann, H., Kuhlmann, J., Kerth, A., Winter, R., and Blume, A. (2006) Insertion of lipidated Ras proteins into lipid monolayers studied by infrared reflection absorption spectroscopy (IRRAS). *Biophys J 91*, 1388-401.

(82) Flach, C. R., Brauner, J. W., Taylor, J. W., Baldwin, R. C., and Mendelsohn, R. (1994) External reflection FTIR of peptide monolayer films in situ at the air/water interface: experimental design, spectra-structure correlations, and effects of hydrogen-deuterium exchange. *Biophys J 67*, 402-10.

(83) Dendramis, A. L., Poser, J. W., and Schwinn, E. W. (1983) Laser Raman spectroscopy of calf bone Gla protein. *Biochim Biophys Acta 742*, 525-9.

(84) Myshakina, N. S., and Asher, S. A. (2007) Peptide bond vibrational coupling. *J Phys Chem B 111*, 4271-9.

(85) Tatulian, S. A. (2003) Attenuated total reflection Fourier transform infrared spectroscopy: a method of choice for studying membrane proteins and lipids. *Biochemistry 42*, 11898-907.

(86) Byler, D. M., and Susi, H. (1986) Examination of the secondary structure of proteins by deconvolved FTIR spectra. *Biopolymers 25*, 469-87.

(87)   Baro, A. M., Miranda, R., Alaman, J., Garcia, N., Binnig, G., Rohrer, H., Gerber, C., and Carrascosa, J. L. (1985) Determination of surface topography of biological specimens at high resolution by scanning tunnelling microscopy. *Nature 315*, 253-4.

(88)   Herz, M. G., F. J., and Mannhart, J. (2003) Probing the shape of atoms in real space. *Phys. Rev. B 68*, 0453011-0453017.

(89)   Giessibl, F. J., Hembacher, S., Bielefeldt, H., and Mannhart, J. (2000) Subatomic Features on the Silicon (111)-(7x7) Surface Observed by Atomic Force Microscopy. *Science 289*, 422-426.

(90)   Muller, D. J., Janovjak, H., Lehto, T., Kuerschner, L., and Anderson, K. (2002) Observing structure, function and assembly of single proteins by AFM. *Prog Biophys Mol Biol 79*, 1-43.

(91)   Tompkins, B. (1999) *MultiMode™ SPM Instruction Manual*, Digital Instruments Veeco Metrology Group, Santa Barbara.

(92)   Morris, V. J., kirby, A. R., and Gunning, A.P. (1999) *Atomic Force Microscopy for Biologists*, Imperial College Press, London.

(93)   Magonov, S. N., and Whangbo, M. -H. (1996) *Surface analysis with STM and AFM. Experimental and theoretical aspects of image analysis.*, Weinheim, New York, Basel, Cambridge, Tokyo.

(94)   Pappalardo, G., Milardi, D., Magri, A., Attanasio, F., Impellizzeri, G., La Rosa, C., Grasso, D., and Rizzarelli, E. (2007) Environmental factors differently affect human and rat IAPP: conformational preferences and membrane interactions of IAPP17-29 peptide derivatives. *Chemistry 13*, 10204-15.

(95)   Lindberg, M., Biverstahl, H., Graslund, A., and Maler, L. (2003) Structure and positioning comparison of two variants of penetratin in two different membrane mimicking systems by NMR. *Eur J Biochem 270*, 3055-63.

(96)   Mascioni, A., Porcelli, F., Ilangovan, U., Ramamoorthy, A., and Veglia, G. (2003) Conformational preferences of the amylin nucleation site in SDS micelles: an NMR study. *Biopolymers 69*, 29-41.

(97)   Henry, G. D., and Sykes, B. D. (1994) Methods to study membrane protein structure in solution. *Methods Enzymol 239*, 515-35.

(98) Reynolds, J. A., and Tanford, C. (1970) The gross conformation of protein-sodium dodecyl sulfate complexes. *J Biol Chem 245*, 5161-5.

(99) Mattice, W. L., Riser, J. M., and Clark, D. S. (1976) Conformational properties of the complexes formed by proteins and sodium dodecyl sulfate. *Biochemistry 15*, 4264-72.

(100) Cui, X., Mao, S., Liu, M., Yuan, H., and Du, Y. (2008) Mechanism of surfactant micelle formation. *Langmuir 24*, 10771-5.

(101) Ahmad, M. F., Ramakrishna, T., Raman, B., and Rao Ch, M. (2006) Fibrillogenic and non-fibrillogenic ensembles of SDS-bound human alpha-synuclein. *J Mol Biol 364*, 1061-72.

(102) Yamamoto, S., Hasegawa, K., Yamaguchi, I., Tsutsumi, S., Kardos, J., Goto, Y., Gejyo, F., and Naiki, H. (2004) Low concentrations of sodium dodecyl sulfate induce the extension of beta 2-microglobulin-related amyloid fibrils at a neutral pH. *Biochemistry 43*, 11075-82.

(103) Patil, S. M., Xu, S., Sheftic, S. R., and Alexandrescu, A. T. (2009) Dynamic alpha-helix structure of micelle-bound human amylin. *J Biol Chem 284*, 11982-91.

(104) Demel, R. A., Geurts van Kessel, W. S., Zwaal, R. F., Roelofsen, B., and van Deenen, L. L. (1975) Relation between various phospholipase actions on human red cell membranes and the interfacial phospholipid pressure in monolayers. *Biochim Biophys Acta 406*, 97-107.

(105) Clement, L., Kim-Sohn, K. A., Magnan, C., Kassis, N., Adnot, P., Kergoat, M., Assimacopoulos-Jeannet, F., Penicaud, L., Hsu, F., Turk, J., and Ktorza, A. (2002) Pancreatic beta-cell alpha2A adrenoceptor and phospholipid changes in hyperlipidemic rats. *Lipids 37*, 501-6.

(106) Wolf, B. A., Pasquale, S. M., and Turk, J. (1991) Free fatty acid accumulation in secretagogue-stimulated pancreatic islets and effects of arachidonate on depolarization-induced insulin secretion. *Biochemistry 30*, 6372-9.

(107) Turk, J., Wolf, B. A., Lefkowith, J. B., Stump, W. T., and McDaniel, M. L. (1986) Glucose-induced phospholipid hydrolysis in isolated pancreatic islets: quantitative effects on the phospholipid content of arachidonate and other fatty acids. *Biochim Biophys Acta 879*, 399-409.

(108) Canale, C., Torrassa, S., Rispoli, P., Relini, A., Rolandi, R., Bucciantini, M., Stefani, M., and Gliozzi, A. (2006) Natively folded HypF-N and its early amyloid aggregates interact with phospholipid monolayers and destabilize supported phospholipid bilayers. *Biophys J 91*, 4575-88.

(109) Meng, X., Fink, A. L., and Uversky, V. N. (2008) The effect of membranes on the in vitro fibrillation of an amyloidogenic light-chain variable-domain SMA. *J Mol Biol 381*, 989-99.

(110) Kayed, R., Bernhagen, J., Greenfield, N., Sweimeh, K., Brunner, H., Voelter, W., and Kapurniotu, A. (1999) Conformational transitions of islet amyloid polypeptide (IAPP) in amyloid formation in vitro. *J Mol Biol 287*, 781-96.

(111) Radovan, D., Smirnovas, V., and Winter, R. (2008) Effect of pressure on islet amyloid polypeptide aggregation: revealing the polymorphic nature of the fibrillation process. *Biochemistry 47*, 6352-60.

(112) Apetri, M. M., Maiti, N. C., Zagorski, M. G., Carey, P. R., and Anderson, V. E. (2006) Secondary structure of alpha-synuclein oligomers: characterization by raman and atomic force microscopy. *J Mol Biol 355*, 63-71.

(113) Marek, P., Abedini, A., Song, B., Kanungo, M., Johnson, M. E., Gupta, R., Zaman, W., Wong, S. S., and Raleigh, D. P. (2007) Aromatic interactions are not required for amyloid fibril formation by islet amyloid polypeptide but do influence the rate of fibril formation and fibril morphology. *Biochemistry 46*, 3255-61.

(114) Jansen, R., Dzwolak, W., and Winter, R. (2005) Amyloidogenic self-assembly of insulin aggregates probed by high resolution atomic force microscopy. *Biophys J 88*, 1344-53.

(115) Ortiz, C., Zhang, D., Ribbe, A. E., Xie, Y., and Ben-Amotz, D. (2007) Analysis of insulin amyloid fibrils by Raman spectroscopy. *Biophys Chem 128*, 150-5.

(116) Hong, D. P., Ahmad, A., and Fink, A. L. (2006) Fibrillation of human insulin A and B chains. *Biochemistry 45*, 9342-53.

(117) Krebs, M. R., Morozova-Roche, L. A., Daniel, K., Robinson, C. V., and Dobson, C. M. (2004) Observation of sequence specificity in the seeding of protein amyloid fibrils. *Protein Sci 13*, 1933-8.

(118) Yan, L. M., Velkova, A., Tatarek-Nossol, M., Andreetto, E., and Kapurniotu, A. (2007) IAPP mimic blocks Abeta cytotoxic self-assembly: cross-suppression of amyloid toxicity of Abeta and IAPP suggests a molecular link between Alzheimer's disease and type II diabetes. *Angew Chem Int Ed Engl 46*, 1246-52.